UNIVERSITY COLLEGE LONDON

Faculty of Mathematics and Physical Sciences

Department of Physics & Astronomy

MOLECULAR EMISSION IN ACTIVE CENTRES OF NEARBY GALAXIES

Thesis submitted for the Degree of Doctor of Philosophy of University College London

by

George Kelly

Supervisors:
Prof. Serena Viti
Dr Thomas Greve

Examiners:
Prof. Ian Howarth
Prof. Chris Lintott

November 29, 2016

I, George Kelly, confirm that the work presented in this thesis is my own. Where information has been derived from other sources, I confirm that this has been indicated in the thesis.

Abstract

The work of this thesis focuses on observations of molecular rotational lines, which are used to uncover the properties of some of the most extreme regions of nearby galaxies. We complete this by both direct analysis of the observations, and using a suite of astrochemical models. We study the distribution of CS in two nearby starburst galaxies, NGC 6946 and NGC 3079. Two low-J lines of CS are observed with the IRAM-30m telescope in a region spanning 50″ about the centre of each galaxy. Both lines have a high critical density that makes CS a good tracer of dense, star-forming gas. Through LTE analysis and a coupled radiative transfer-chemical modelling, we find a temperature and density gradient from the centre of NGC 6946 to the offset pointings. In NGC 3079, we find uniform temperature.

We also present observations of SiO and HNCO in nearby galaxy NGC 1068 from the Plateau de Bure interferometer (PdBI). We see four clear peaks, one for each molecule to both the west and the east of the AGN. From a detailed chemical modelling we find that a high SiO abundance and low HNCO indicate a fast shock, while high HNCO and low SiO indicates either a slow shock or warm, dense, non-shocked gas. Comparing to observations, the east is therefore likely to contain gas that is heavily shocked. Gas to the west may be non-shocked, or maybe undergoing a much milder shock event. We complete a radiative transfer modelling. Taking into account these results, the milder shock event is the more likely of the two. Finally, ALMA observations of the distribution of several molecules in NGC 1068 are analysed. These molecules trace different components of the molecular gas in the AGN, circumnuclear disc and starburst ring. Spectral analysis of each molecule, and the ratio between molecules are used to determine galaxy properties and how these vary from region to region.

Acknowledgements

There are many people to whom I owe my thanks for this thesis and my time at UCL. To my supervisor, Serena, for her expert guidance and wisdom. Without her insight, encouragement and patience, the completion of this thesis would have been quite overwhelming. To Santi, for the invaluable knowledge I gained on my visits to Madrid. To the group of UCL astrochemists past and present, for advice and help whenever I needed it. To Komal, for her constant and unwavering support throughout my PhD. Thank you for your love and kindness and for sticking by me during some of the more stressful moments of the last four years. I could not have done this without you. To my parents, my brothers and all my family, for their full support and backing from beginning to end. To the old members of G18 and beyond for some great times, mostly at the Euston Tap. And finally, to STFC for my studentship and travel grants.

Contents

This page was intentionally left blank

List of Figures

This page was intentionally left blank

List of Tables

Chapter 1

Introduction

1.1 The Interstellar Medium and Molecular Astrophysics

The vast space between the stars is not empty. The interstellar medium (ISM) consists of many different components. This occurs due to a processing of the gas and dust that is present between stellar systems, leading to a mixture of atomic, molecular and ionised gas, as well as dust grains. The cycle through the many phases of the ISM is depicted in Figure 1.1. The many stages of gas in the ISM provide varying physical conditions. McKee and Ostriker (1977) showed that the diffuse region of the ISM is actually composed of three regions, cold neutral medium (CNM), warm neutral medium (WNM) and hot ionised medium (HIM). This diffuse gas transitions to molecular clouds. Many processes govern this cycle; stellar radiation pressure (Zinnecker and Yorke 2007) and stellar winds (Hollenbach et al. 1976) force diffuse gas into more compact formations, which may collapse gravitationally to eventually form stars. Observing molecular gas is the key to the understanding of the many physical processes occurring locally and in external galaxies. To do so, it is vital to understand the chemistry of these regions. The field of astrochemistry is relatively young, and even more so is its application to the study of nearby galaxies. The advent of new state of the art ground based facilities, such as the Atacama Large Millimetre Array (ALMA, Wootten and Thompson 2009), coupled with space telescopes

and older ground based single dish facilities, has provided greater opportunity for these studies.

Molecular clouds are inhomogeneous in density. They contain dense cores that may be stable enough to remain starless, or may go on to exceed the Jeans length and form a protostellar core. This is governed largely by the amount of magnetic or turbulent pressure supporting the core (Tan et al. 2013). Subsequent star formation mechanisms are split into low- and high-mass regimes, with a cutoff of $\sim 8\ M_{\odot}$. The principle difference being that for high mass stars, the time scale for accretion is longer than the time taken to radiate gravitational energy during collapse. This means that massive stars begin nuclear fusion while matter is still accreting, while low mass stars do not. Stars of different mass return matter to the ISM through different methods. Low mass stars end their lives as planetary nebulae, with stellar winds responsible for ejecting material. High mass stars affect the surrounding area throughout their lifetime, providing UV photons to ionise gas. Massive stars end in a supernova and eject stellar remains back into the ISM.

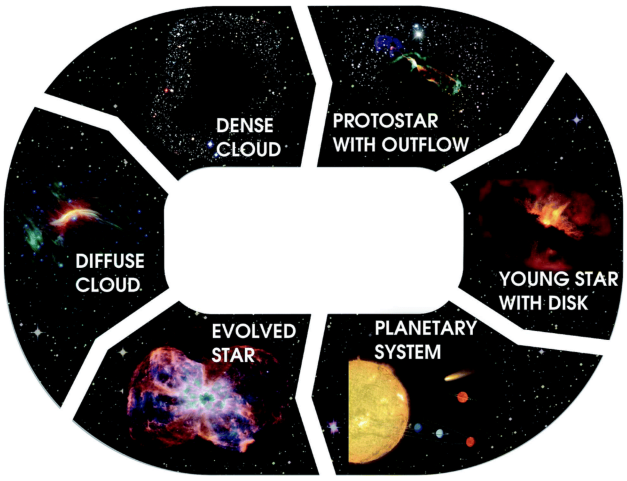

Figure 1.1: Life cycle of the ISM from van Dishoeck (2014). Image credit to NASA / ESA / ESO / NRAO

The release of matter from stars back into the ISM is important in that this creates the heavier elements required for the complex chemistry that takes place in molecular clouds. These are the regions that are of most interest to this thesis. Observations of molecules, coupled with theoretical models, can allow for a much greater understanding of these regions. In this introduction the chemistry and physics of the ISM, as well as how it relates to particular objects or regions, will be discussed.

1.2 Gas-Phase Chemistry

Molecular clouds are cold, with temperatures around 10 K. This has a profound effect on the chemistry that can occur. Reactions between two neutral species do occur in this environment, but they are often extremely inefficient due to small cross sections for reactions. Activation barriers are not easily overcome when the temperature is so low. For these reactions to be significant the density must be very high to increase the frequency of collisions. Ion-neutral reactions are much more efficient. The ion induces a temporary dipole in the neutral species and causes an attraction between the two reactants. Thus, the cross section for the reaction is significantly increased.

All ion-neutral reactions are highly dependent on initial reactions that form H_3^+. The most obvious way of ionising molecular hydrogen is with a UV photon, which would be readily available in the presence of massive stars. UV photons are largely unable to penetrate denser regions of molecular clouds due to the high extinction. However, gas-phase chemistry can proceed as it is possible for cosmic rays to initiate ion-neutral reactions in regions of high extinction, as in Reaction 1.1, where ζ denotes a cosmic ray.

$$\begin{aligned} &H_2 + \zeta \longrightarrow H_2^+, \\ &H_2^+ + H_2 \longrightarrow H_3^+ + H \end{aligned} \tag{1.1}$$

However it forms, H_3^+ is then able to initiate many further ion-neutral reactions through the donation of a proton. The products of these reactions can then provide the ion reactant needed for reactions between successively more complex species.

1.3 Dust and surface reactions

Dust is ubiquitous in the ISM. Grains range in size, a, from nanometers to microns, in a distribution originally postulated to be $n(a) \propto a^{-3.5}$ (Mathis et al. 1977). This has been modified subsequently based on extinction to give a more complex distribution (Weingartner and Draine 2001). Grains are mostly formed in stellar atmospheres and in supernovae, but may also be formed, and can certainly be destroyed in the ISM. They predominately consist of silicate and carbonaceous species, with smaller grains sometimes made up of single large polycyclic aromatic hydrocarbons (PAHs). Dust makes up approximately 1/100

of the ISM by mass as measured for the Milky Way (Savage and Mathis 1979), but this value varies quite considerably especially for other galaxies. Dust is key to the physics and chemistry of many different processes. Approximately half of stellar light emitted in the UV, visible and near-IR is absorbed by dust and remitted and longer wavelengths (Lequeux 2005). UV irradiation can release electrons via the photoelectric effect. Where gas number density reaches $\sim 10^4$ mol cm^{-3}, these electrons begin to efficiently transfer energy between gas and dust, coupling the two. In addition, atoms and molecules colliding with grains may stick to the surface and form an icy mantle. This brings species closer together and acts as a catalyst for interstellar chemistry.

At the low temperatures experienced in molecular clouds, gas phase species begin to stick to surfaces of dust grains. This can occur relatively weakly at very low temperatures ($\sim$ 10 K) through van der Waals forces (physisorption). At higher temperatures, and depending on the species, these weak bonds are easily overcome and a full chemical bond must form to retain a species on the grain surface (chemisorption). These processes are of significance as they bring together atoms and molecules from the gas phase (chemically depleting it) to a proximity where they may react. Formation reactions can occur in the following ways (also shown in Figure 1.2) (Pirronello et al. 2003):

- Langmuir-Hinshelwood mechanism - both species are on the grain surface and they diffuse towards one another and react
- Eley-Rideal mechanism - one species is on the grain surface and a gas phase species collides directly with it to react
- Harris-Kasemo mechanism - this mechanism represents a sort of in-between from the previous two. A species striking the surface may rebound into the gas phase or get trapped. A trapped species may rebound many times before reacting with a species already present on the grain surface.

Dust is possibly of most importance chemically because of the formation of H_2 on the grain surface. In Section 1.2, the importance of H_2 on all interstellar chemistry was discussed. However, H_2 cannot form in the gas phase. If two hydrogen atoms in the gas phase collide they may end up in a vibrational level of the ground electronic state higher than the dissociation limit. The molecule must be stabilised through a transition to the ground state but this process is slow and therefore improbable. It may end up in a higher

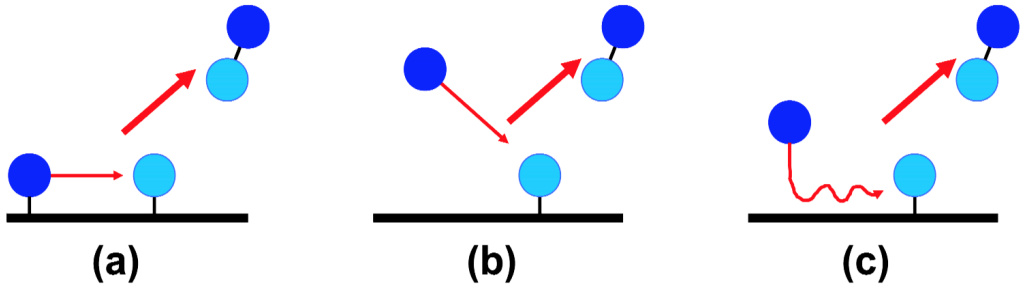

Figure 1.2: Possible mechanisms for two body grain surface reactions (Chen 2011). a) Langmuir-Hinshelwood, b) Eley-Rideal, c) Harris-Kasemo.

electronic state, but with only highly forbidden routes back to the ground state (Duley and Williams 1984). The rate of formation of H_2 is well known (Habart et al. 2004) and by comparing to the rate coefficient of the gas phase reaction between two hydrogen atoms, it is clear that it is not responsible for H_2 formation (Vidali 2013).

The Reaction system 1.2 has also been considered as a gas phase route

$$\begin{aligned} \mathrm{H} + \mathrm{e}^- &\longrightarrow \mathrm{H}^- + h\nu, \\ \mathrm{H}^- + \mathrm{H} &\longrightarrow \mathrm{H}_2 + \mathrm{e}^- \end{aligned} \tag{1.2}$$

This has been found to be the dominant route in the early universe (Saslaw and Zipoy 1967), when dust grains were not present, but in the present universe the electron density is too low to produce very much H_2. The need for dust grains as catalysts for H_2 formation was developed by Gould and Salpeter (1963) and Hollenbach and Salpeter (1969). Hydrogen atoms may not encounter dust grains very often, but when they do the chance they react with another hydrogen atom is quite high. The Langmuir-Hinshelwood mechanism is the most efficient formation route to H_2 with Goodman (1978) calculating H mobility via quantum tunnelling and thermal hopping on graphite grains. This work was furthered by many authors calculating the bonding energy of H chemisorbed to different surfaces (e.g. Klose 1992; Aronowitz and Chang 1985) as well as numerous modelling attempts. Although the detailed mechanism for hydrogen formation on dust grains is still not completely clear, it is widely accepted as being the dominant formation route.

1.4 Extragalactic Molecular Astrophysics

The first detection of interstellar molecular lines in external galaxies was made by Weliachew (1971), in NGC 253 and M82. The detection was of OH, which was only detected in absorption. It was not until Rickard et al. (1975) observed CO in the same galaxies that an emission line was seen. Further detections of various different molecules have followed in the last few decades, perhaps the most impressive being the detection of CO in a galaxy at redshift, z >6 by Walter et al. (2004), proving that chemistry was occurring to produce molecular gas in the early universe.

CO is the molecule most observed in external galaxies. As it is so abundant, it is the easiest to detect. H_2 has no dipole moment so is very difficult to detect at the low temperatures in molecular clouds. To calculate the quantity of molecular gas in a galaxy, CO is therefore observed and a CO-to-H_2 conversion factor estimated. While this is quite well known for the Milky Way, the value varies between galaxies, and between regions within galaxies (Bolatto et al. 2013). Caution must be used when using this approach for external galaxies. However, using CO detections is one of the most direct ways of measuring Star Formation Rate (SFR). Lu et al. (2015) do this effectively even for high redshift galaxies, using the ratio of CO($J = 7 - 6$) to IR emission from dust, which is usually used as a SFR tracer, and calibrating to SFR-IR using Kennicutt (1998). This has an advantage as CO is not enhanced by non-stellar radiation (for example active galactic nuclei, discussed in Section 1.4.2) in the way dust is. For most normal spiral galaxies, the sum mass of molecular and atomic hydrogen scales well with the SFR (Boselli et al. 2002).

Other molecules can be used to trace different gas components in external galaxies. Particularly with single dish observations, the beam will encompass a combination of different environments and molecules can be used to disentangle these components. Some of the uses of molecules as molecular tracers are discussed in Section 1.4.3. First we discuss classes of galaxy that are of importance to this thesis.

1.4.1 Starburst Galaxies

Starburst galaxies differ from normal galaxies through their greater Star Formation Rate (SFR). They are the far extreme of a continuous spectrum of galactic SFRs. A starburst in a galaxy is transient. It is a period of time where the galaxy converts vast quantities

of gas into stars. Starbursts should therefore be treated more as a phase in a galaxy's evolution, rather than a galaxy type. This period is relatively short-lived (10^7 - 10^8 years (Leitherer et al. 1999; Neri et al. 2003)), as it is limited by the supply of gas required for star formation. The rapid rate of star formation causes the galaxy to undergo an enhanced period of evolution, changing not only its stellar and gas content, but also dust content, colour and metallicity. The study of starbursts is therefore vital for the understanding of galaxy evolution as a whole.

Starbursts are not confined to a particular galaxy morphology or luminosity. They cover dwarf galaxies, such as the Large Magellanic Cloud ($L_{IR} \approx 10^8\ L_\odot$), up to ultraluminous infrared galaxies (ULIRGs, $L_{IR} > 10^{12}\ L_\odot$). This, coupled with their ephemeral nature, leads to some difficulty in classification. Simply classifying a galaxy as undergoing a starburst can be somewhat controversial, as no one single definition exists. For low redshift galaxies, some such criteria include a SFR that can't be sustained for more than a certain amount of time (e.g. 10^8 years), or a have disk averaged SFR surface density (i.e. the mean SFR per unit area across the galaxy) of $\Sigma > 1\ M_\odot \mathrm{yr}^{-1}\ \mathrm{kpc}^{-2}$ (Kennicutt and Evans 2012). Figure 1.3 is a plot showing individual galaxies' disk averaged SFR surface density against their total SFR. This is used as an illustration of the problems associated with classifying starbursts. There is an enormous amount of scatter in this plot, with many normal galaxies overlapping starbursts. It also draws attention to the subclasses of starburst. "Infrared selected", as indicated on the plot, refers to ULIRGs and LIRGs (the latter being an order of magnitude or so less luminous than the former). At lower redshifts, these galaxies are largely similar to the prototype starbursts; with a very high SFR in the circumnuclear region. At higher redshift, different characteristics make up the majority; the SFR is quite uniformly high across the entire disk. This is because these galaxies are gas-rich enough to reach LIRG luminosity across the whole galaxy (Daddi et al. 2010). In both cases, these galaxies are usually very dusty. In the plot, circumnuclear indicates that the starburst event occurs in the central region of the host galaxy. For example, the local prototype starburst NGC 253 (Strickland et al. 2002) has a SFR of 5 $M_\odot \mathrm{yr}^{-1}$ in its nuclear region; $\sim 70\%$ of the SFR for the entire galaxy (Wik et al. 2014). For comparison, a regular galaxy may see a SFR of $\sim 1\ M_\odot \mathrm{yr}^{-1}$ across its entirety (Robitaille and Whitney 2010). The cause of the starburst event here is gas migrating from the galactic disk towards the central region. This can occur due to interaction with a nearby passing galaxy. Tidal forces perturb the orbits of disk stars and gas. As gas clouds

are thrown out out of their orbits they collide with one another, and kinetic energy transfers. This leads to a transfer of angular momentum; some clouds some outwards and some provide the central region of the galaxy with an inflow of gas. This provides the fuel for a circumnuclear starburst. This is often the case for low-z LIRGs and ULIRGs (Duc et al. 1997). The timescale for star formation is, however, frequently shorter than the dynamical timescale of the interaction. The peak starburst may last around 10^7 - 10^8, whereas the interaction should last at least an order of magnitude longer than this (Kennicutt et al. 1998). In addition, many starbursts are not obviously interacting. In these cases there must be some other force causing gas to flow inwards. This could be due to the presence of a stellar bar, which can act to remove angular momentum from gas. Finally, the plot shows blue compact galaxies (BCGs). These are low mass and contain very little dust. They are also very low metallicity. As many as 80% show evidence of recent interaction (Pustilnik et al. 2001), explaining the starburst activity. Numerical simulations confirm that BCG can form from either dwarf-dwarf mergers or through tidal interactions (Bekki 2008). However, in BCGs with no evidence of interaction, the reasons for starburst are quite uncertain.

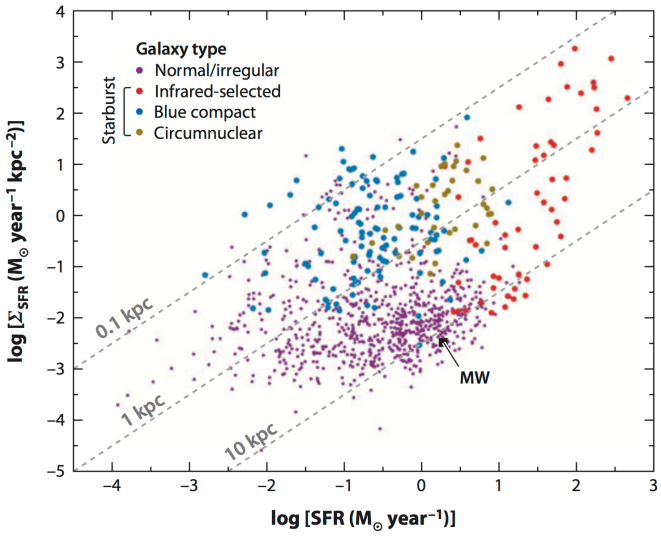

Figure 1.3: Distribution of integrated star-formation properties of galaxies in the local Universe. Each point represents an individual galaxy or starburst region, with the average star-formation rate (SFR) per unit area plotted as a function of the absolute SFR (Figure 9 of Kennicutt and Evans 2012)

Dust grains absorb much of the UV radiation from stars, therefore cannot be directly obscured. Therefore observations of the gas are vital to understanding the processes

governing starburst environments. This UV is re-emitted in the IR as the dust cools. Observations of the dust in the mid-IR have been able to distinguish between the dust heated by starbursts and the dust heated by an active galactic nucleus (AGN) (Armus et al. 2007). This is important as there appears to be a clear correlation between AGN and starbursts; half of all Seyfert 2 galaxies have a circumnuclear starburst (González Delgado et al. 1998). It is likely that these two phenomena are not unrelated. In galaxies with both an AGN and a starburst, the cause of each may be an interaction with another galaxy. In a minority of cases this can mean a full merger but more often it is likely due to a "close approach".

1.4.2 Active Galactic Nuclei

An active galactic nucleus (AGN) is the central region of a galaxy that displays energetic phenomena that cannot be attributed to stars. AGN are subcategorised into several different classes. Much of the reasoning behind this is the historical understanding that different classes were not related. More recently, a unified model of AGN attempts to explain the differences seen in each class (Antonucci 1993). The two largest classes of AGN are Seyferts and Quasars (or quasi-stellar objects, QSOs). The principal observational difference between the two is their luminosity. The AGN in a Seyfert galaxy is typically as luminous as the total luminosity of all stars in the galaxy ($\sim 10^{11}\ L_{\odot}$). A QSO is 100 times brighter. Sources with this amount of power output are very rare. They are therefore seen more often at great distances, where the luminosity of the AGN far outshines the stellar contribution. This made the galaxies when first observed appear as a point source, hence the name "quasi-stellar".

A unified model of AGN is shown in Figure 1.4. Here is shown the separation between the relatively low luminosity radio-quiet Seyferts, and the many types of radio-loud observations that depend on viewing angle. As is shown, all AGN contain at their centre, a supermassive black hole (SMBH). The mass of this of this is correlated with the galaxy's stellar mass and can be as high as $10^{8}\ M_{\odot}$. The accretion disc surrounding the black hole is the power source of the AGN. The dusty torus surrounding it is a highly efficient absorber of high energy photons.

Different classes of AGN were originally classified based on their spectra. Some Seyfert galaxies' spectra show a mixture of broad and narrow lines, some only display the narrow line feature, first identified by Khachikian and Weedman (1974). The broad line features

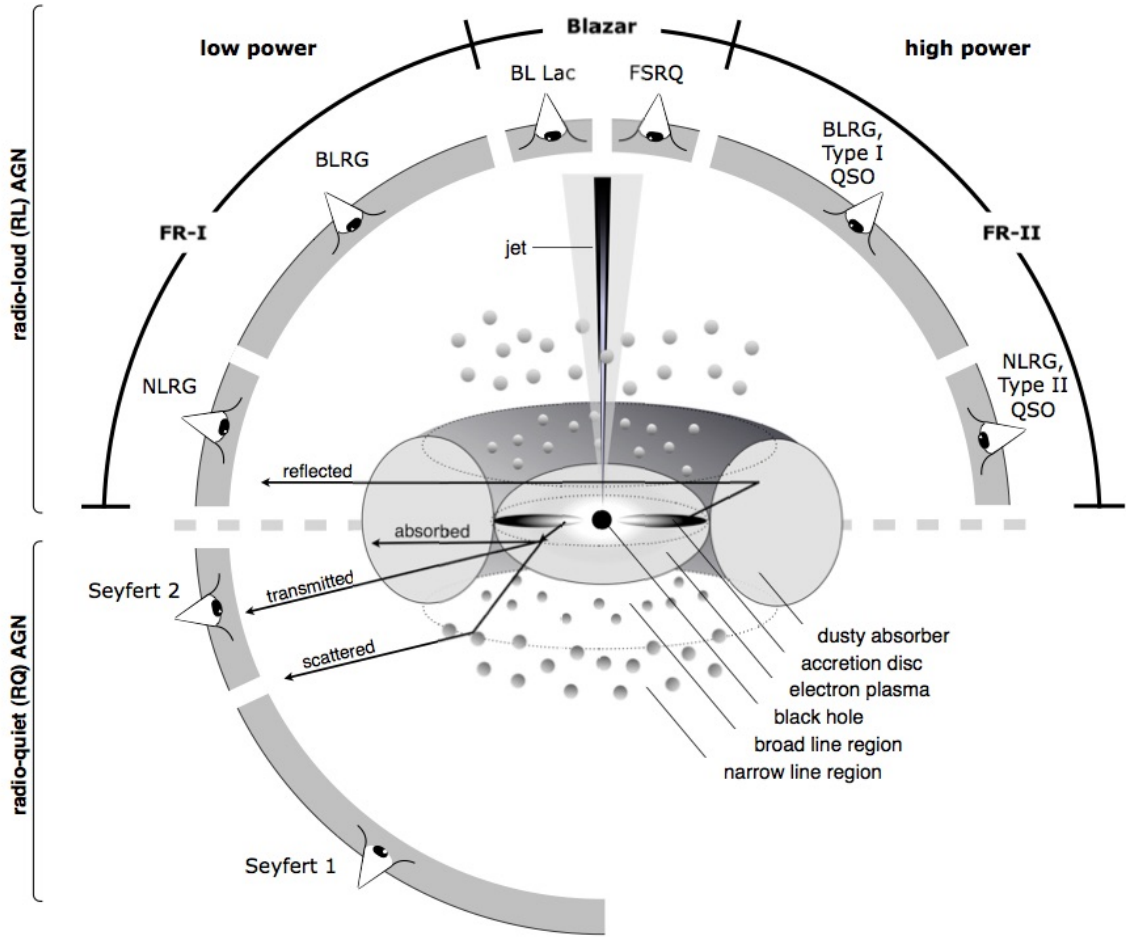

Figure 1.4: Sketch of the unified model for AGN, splitting into two categories: radio-quiet and radio-loud. The other differences observed are dependent only on viewing angle. From Beckmann and Shrader (2012).

come from the gas near to the nucleus, which has velocities in the order of 10^4 km s^{-1}. Forbidden broad line emission is not seen, suggesting the gas must be of very high density (electron number density, $n_e \sim 10^9$ cm^{-3}) in order to collisionally suppress non-electric dipole transitions. Highly excited allowed and forbidden narrow line transitions are seen in all Seyferts, arising from slower (10^{3-4} km s^{-1}), lower density gas, further from the nucleus. Broad line Seyferts are classified as Type I with other Seyferts called Type II. This is interpreted in the unified model as the dusty torus obscuring the broad line region if viewed from a wide angle (Type II). This obscuration is not an obstacle when viewed more face on (Type I).

Radio-loud AGN all produce a highly collimated jet. This is produced as fully ionised gas is accelerated to relativistic speeds along coiled magnetic field lines. Free-free radiation

in the jet is the cause of the radio emission. Radio galaxies are elliptical galaxies that are highly luminous at radio wavelengths. In the same fashion as Seyferts, they are further subcategorised as narrow line (NLRG) or broad line (BLRG). Blazars are radio-loud AGN seen face on so as to completely obscure emission lines. QSOs were originally observed to be star like objects that were radio-loud (Matthews and Sandage 1963). Now accepted to be AGN, they are some of the most intrinsically bright objects in the sky, and have been measured at redshift, z >7 (Mortlock et al. 2011). Although originally observed as radio loud, only 10% of QSOs emit strongly in the radio.

The effect the SMBH has on the surrounding gas can play a significant part in large scale star formation. This AGN feedback occurs due to the interaction between the flux of photons and massive particles generated from accretion, and the interstellar medium. It is possible for this stream of particles to clear the central region of the galaxy of its interstellar gas, thus completely halting star formation. The lack of material available for accretion will also lead to the cessation of the AGN. The primary mode by which the feedback occurs in AGN close to their Eddington limit is through radiative processes (Silk and Rees 1998). This can be through radiative pressure on charged dust grains in the ISM or through a wind generated much closer to the AGN (Fabian 2012). Gas is pushed outwards and dispersed, depressing star formation. Evidence of this AGN feedback is seen is some galactic outflows, where outflow rates have been observed at several times the star formation rate (e.g. Mrk 231, Rupke and Veilleux 2011). The second mode is the the kinetic mode. It is most applicable to galaxies with a hot halo or which are centralised in a cluster. If a galactic centre has been cleared of its gas it will try to refill with intracluster or halo material. The kinetic mode keeps the galaxy clear of this material. This occurs through the heating of gas by the radio source generated at the AGN. The energy input from the AGN is balanced through loss of energy from cooling while the nucleus is active (Cattaneo et al. 2009).

Instabilities in the AGN feedback process disrupt the balance of the heating and cooling. It therefore makes sense to introduce a duty cycle determining the lifetime of the source, which may cover numerous episodes of activity (Schmidt 1966). The timescale for an AGN can be calculated from observations of radio lobes; by determining both their separation and velocity to gain the age. Alternatively, timescale can be estimated from assuming that all galaxies go through an AGN. If this is the case average lifetime can be calculated by multiplying galactic lifetime ($\sim 10^{10}$ years) by the fraction of galaxies that

are observed to be active ($\sim$ 1%). Both methods give a similar estimate of age in the order of 10^8 years.

1.4.3 Molecular Tracers

Molecules can be used to trace different environments. This can be because they are only formed in observable qualities in given conditions, or because they are only excited enough to be observed above a certain density and/or temperature, or a combination of the two. Here we present a list of common tracer molecules and what they are predominantly used to trace. We focus in particular on the molecules that are used in this thesis. It should be noted that these molecules may be observed in a number of different environments, and this list is only a guide as to their use. **CO**

Carbon monoxide, CO, is the second most abundant molecule in the universe, after H_2. It the most widely used molecular tracer and is used to trace molecular gas as a whole. CO has a weak permanent dipole moment ($\mu \approx 0.11$ D) and ground state rotational transition with an excitation temperature of just $\sim$ 5.5 K. This means that CO is readily excited in the very low temperatures of cold molecular clouds.

CS

Carbon monosulphide, CS, is mostly used as tracer of dense gas. Low-J transitions of CS trace the moderately dense gas (e.g. CS$(2-1)$ has a critical density of 2×10^5 cm^{-3} at 100 K), whereas higher-J transitions trace very dense gas (e.g. CS$(7-6)$ has a critical density of 8×10^6 cm^{-3} at 100 K). It is has been particularly well used in starburst galaxies (Mauersberger and Henkel 1989; Bayet et al. 2008a; Aladro et al. 2011b). Observing many transitions can be very useful, allowing for an almost complete coverage of the densest regions of molecular gas clouds. An advantage that CS has in this respect over other dense gas tracers (e.g. HCN) is the spacing of the transitions. A J-ladder from J=1-0 to J=7-6 covers a frequency range of 294 GHz in CS, whereas the same in HCN covers a range of 532 GHz[1]. This allows for potentially easier observing of more transitions.

HCN

Hydrogen cyanide is another dense gas tracer. Extensively used in observations of gaint molecular clouds (GMCs) in the Milky Way (e.g Smith and Wardle 2014), as well as in external galaxies (Davies et al. 2012). HCN$(4-3)$ has a critical density comparible to CS$(7-6)$.

[1] http://www.cv.nrao.edu/php/splat/

CH_3OH

Methanol has been claimed to be a good tracer of dense gas due to critical densities comparable to those of low-J CS and HCN transitions. However, methanol is formed largely on grain surfaces from accreting CO (Das et al. 2008). It is therefore found largely in grain mantles until it is sublimated. This can occur efficiently through the gas being shocked but can also happen due to a warming of the gas or other non-thermal processes.

H_2CO

Formaldehyde is formed efficiently on grain surfaces through hydrogenation of CO (Woon 2002), and like methanol has been used as a dense gas and shock tracer.

SiO

Silicon monoxide is the most widely used shock tracer. Although formed in the gas phase, its formation rate is highly dependent on the abundance of atomic silicon. Dust grain cores contain a large amount of silicon (Krügel 2002). A strong shock is capable of sputtering silicon from the dust (Jiménez-Serra et al. 2008). This significantly enhances the abundance of Si in the gas phase. This then can react with molecular oxygen or a hydroxy radical, forming SiO.

HNCO

HNCO is also used as a shock tracer. It is formed on grain mantles and can be readily sublimated during even a weak shock event. However, its formation routes in the gas-phase are quite uncertain and it has gone undetected in some galaxies where it is expected to be observed (Aladro et al. 2011a).

1.5 Chemical modelling

Modelling of the chemistry in interstellar gas has become more complex as more molecules are observed and further reaction pathways are investigated. More detailed modelling is also required as observational tools become more advanced. The process requires the calculation of the density n_i of all species, i, in the model. However, the values stated are often given as a fractional abundance, X_i, against the density of hydrogen nuclei, n_H: $X_i = n_i/n_H$. The density of a species changes when it takes part in a chemical reaction. This is modelled through the solving a number of non-linear ordinary differential equations to calculate the rate of change of a species based on all the reactions for which it is involved.

In this thesis, chemical modelling generally follows a cold gas cloud from its initial

largely atomic form, though the formation of molecules and its subsequent collapse and heating. In the initial stages, where density and temperature are both low, the chemistry is dominated by gas phase ion-neutral reactions. Over time, via the mechanisms discussed in Section 1.3, species accrete onto dust grain surfaces, forming new molecules and depleting the gas. As the gas cloud collapses and warms, the grain mantle sublimates and gas phase neutral-neutral reactions begin to dominate. This is of course a very general overview and the chemistry is highly dependent on many physical conditions. The most important parameters determining the chemistry of the cloud include: gas and dust temperature; density; the UV radiation field; the cosmic ray ionisation rate; and the initial chemical composition and elemental abundances.

The rate at which a reaction proceeds is calculated either via experimental means or through theory. These rates have been collated and stored in several databases. The database used in this thesis is the University of Manchester Institute of Science and Technology Database for Astrochemistry (UMIST, Woodall et al. 2007; McElroy et al. 2013). Reaction rate coefficients are determined differently depending in the type of reaction taking place. For two body reactions, the rate coefficient, k, is given by Equation 1.3.

$$k = \alpha\Big(\frac{T}{300}\Big)^{\beta} \exp\Big(\frac{-\gamma}{T}\Big) \mathrm{cm^3 s^{-1}} \tag{1.3}$$

Where T is the gas temperature in K and α, β and γ are constants for the each individual reaction, representing the rate coefficient at 300 K, the dependence on temperature and the thermal activation barrier, respectively.

For direct cosmic ray ionisation, the rate is much simpler. The rate goes as Equation 1.4

$$k = \alpha s^{-1} \tag{1.4}$$

Where α is the cosmic ray ionisation rate relative to molecular hydrogen. The Milky Way standard ISM rate is usually taken as $\sim 10^{-17}$ s^{-1} (Indriolo et al. 2007).

Cosmic rays may also lead to the emission of UV photons which then leads to photoreactions. This occurs when a cosmic ray photon collisionally excites H_2, which then relaxes back to its ground state (Sternberg et al. 1987). Where a cosmic ray induces a

photoreaction, the rate is given as Equation 1.5

$$k = \alpha\Big(\frac{T}{300}\Big)^{\beta}\frac{\gamma}{1-\omega}\mathrm{s}^{-1} \tag{1.5}$$

Where α is the cosmic ray ionisation rate. Everything to the right of α is related to the UV photon (and reaction partner), not the cosmic ray. Most UV photons will be absorbed by dust grains, which is accounted for through ω; the dust grain albedo in the far UV, and γ; the efficiency of the cosmic ray ionisation event that is given by Equation 1.6, from Gredel et al. (1989)

$$\gamma = \int \frac{\sigma_M(\nu)P(\nu)}{\sigma_g}d\nu \tag{1.6}$$

Where $\sigma_M(\nu)$ is the photoionisation cross-section at frequency, ν, $P(\nu)$ is the probability for photon emission, and σ_g is the dust grain extinction cross-section.

For direct photoreactions, the rate coefficient is given as Equation 1.7

$$k = \alpha\exp\left(-\gamma A_v\right)\mathrm{s}^{-1} \tag{1.7}$$

Where α is the unshielded rate coefficient for the Draine radiation field (Draine 1978), A_v is the visible extinction and γ is a correction for the increased extinction at UV wavelengths.

Gas-grain and grain-surface reactions are handled in different ways in different models. A rate must be calculated at which each species depletes from the gas phase onto the grain surface to form an icy mantle. This rate is governed by kinetic theory and is given by Equation 1.8 (Spitzer 1978; Umebayashi and Nakano 1980; Rawlings et al. 1992)

$$\frac{dn_i}{dt} = 4.57\times10^4 d_g\sigma_g^2 T^{1/2} C n_H S_i m_i^{-1/2} n_i\mathrm{cm}^{-3}\mathrm{s}^{-1} \tag{1.8}$$

Where d_g is the ratio of dust grains to hydrogen nuclei; σ_g is the grain radius in cm; S_i is a sticking coefficient to approximate physisorption and chemisorption, where S_i is between 0 and 1; m is the mass of species i in amu; and C is a factor to account for electrostatic effects

and is equal to 1 for neutral species and is equal to $1 + 16.71 \times 10^{-4}/\sigma_g T$ for a singly charged cation, indicating charged species will freeze out quicker than neutral species. Reactions in the grain mantle are not well understood. We will describe the processes and assumptions made in this thesis, although there are other methods for considering grain surface reactions. We assume that when a species freezes out, it instantaneously reacts with hydrogen, until fully hydrogenated (e.g. atomic carbon forms methane etc). This is on the basis that hydrogen is by far the most abundant species on the grain and as the lightest, it is also the most mobile. The hydrogen is simply taken from the gas reservoir and implies that molecular hydrogen is formed on the grain surface. This allows for very rapid calculation of mantle species abundance.

Sublimation of mantle ices back into the gas phase may proceed via thermal and non-thermal processes. Non-thermal mechanisms of sublimation have been successfully modelled to include desorption through exothermic surface reactions (Garrod et al. 2007) and cosmic rays (both directly and through induced photoreactions; Roberts et al. 2007). In contrast, laboratory experiments find that it is very difficult to characterise temperatures for thermal desorption processes. Values are found to be highly dependent on the composition of the ice and on the heating rate (e.g. Noble et al. 2012).

1.5.1 UCL_CHEM

The model used in this thesis is UCL_CHEM (Viti and Williams 1999; Viti et al. 2004b, 2011). This model has been adapted to many different environments, e.g. hot cores (Viti et al. 2001), molecular outflows (Viti et al. 2004a), nearby galaxies (Bayet et al. 2008a) and high redshift galaxies (Lintott et al. 2005). The model is time dependent and is split into two phases:

- Phase I: A diffuse cloud collapses. Spherical Symmetry is assumed. While this may not be the case in reality, the model does account for some rotational and magnetic support. In terms of chemistry, since we are modelling to such a large observed area, any non-symmetry should not affect our results significantly. Initially all species are atomic, other than hydrogen, which is assumed to be half atomic and half molecular. The initial elemental abundances are either assumed to be solar, altered to consider the metallicity of the environment being modelled, or may take a value to take into consideration depleted to dust grain cores. The collapse may be treated as free fall

or as a modified free fall. From Spitzer (1978), the equation of motion for collapse of a cold sphere of uniform density, ρ, assuming that the sphere is at rest at time, t = 0, is given as:

$$\frac{d^2r}{dt^2} = -\frac{GM_0}{r^2} = -\frac{4\pi G\rho_0 r_0^3}{3r^2} \tag{1.9}$$

Where r is the radius of a particular mass shell as a function of time and M_0 is the mass interior to the initial radius of the shell. This is multiplied by dr/dt and integrated to give:

$$\frac{dr}{r_0 dt} = -\Big[\frac{8\pi G\rho_0}{3}(\frac{r_0}{r} - 1)\Big]^{1/2} \tag{1.10}$$

This is then combined with the conservation of mass in a spherical cloud to give Equation 1.11 (Brown et al. 1988; Nejad et al. 1990; Rawlings et al. 1992)

$$\frac{dn}{dt} = B\Big(\frac{n_H^4}{n_0}\Big)^{1/3}\left[24\pi G m_H n_0\Big[\Big(\frac{n_H}{n_0}\Big)^{1/3} - 1\Big]\right]^{1/2}, n_H > n_0 \tag{1.11}$$

Where n_0 is the initial diffuse cloud density, G is the gravitational constant and B is a retardation factor $\leqslant 1$ to approximate magnetic and rotational support. The temperature is set to be a constant 10 K. During the collapse, freeze out occurs according to Equation 1.8 as well those gas-phase reactions which proceed at low temperature. The freeze out occurs as described previously, with the addition that a small percentage of CO freezes to form methanol. The collapse runs until the density reaches a set value. This is mostly treated as a free parameter in this thesis.

- Phase II: The new molecular cloud undergoes heating assumed to be from external sources. As previously stated, thermal desorption is not well understood. Therefore the model handles it in a simplified way. At temperatures >100 K, the mantle is assumed to sublimate at timescales much shorter than the lifetime of the cloud and the desorption occurs instantaneously. In the case where temperature is less than 100 K, only selected molecules are allowed to desorb. This is based on the work of

Collings et al. (2004), who study 16 astrophysically relevant molecules. They find that certain molecules may become trapped within water ice at T <100 K meaning that they do not desorb as efficiently as may be expected based solely on their binding energies. In addition, the cloud may be subjected to a number of external forces, such as an FUV field, cosmic ray flux or it may undergo a shock. UCL_CHEM handles shocks in one of two ways. Firstly, a simplified shock may be simulated by swiftly heating and then cooling the gas. A more complex approach is described in Viti et al. (2011), and couples the chemical model to the parametric shock code of Jiménez-Serra et al. (2008). This calculates the the physical structure of a shock as it propagates through the previously unperturbed gas cloud. A saturation time is input to the model to determine at what time point the icy grain mantles are sputtered. The final density and initial velocity of the shock are input and determine the maximum temperature attainable in the neutral gas within the shock (Draine et al. 1983).

1.6 Radiative transfer

Although determining if and how molecules form in a specific medium is a useful tool in itself, it is also important to calculate how molecular emission is transported through that medium. The radiative transfer equation (1.12) describes the change in intensity, I_ν, of a beam along path, ds at frequency, ν

$$\frac{dI_\nu}{ds} = j_\nu - \alpha_\nu I_\nu \tag{1.12}$$

Where j_ν is the emission coefficient and α_ν is the absorption coefficient. We can also refer to the source function, $S_\nu = j_\nu/\alpha_\nu$, the emissivity of the medium per unit optical depth, τ_ν, where $d\tau_\nu = \alpha_\nu ds$. This then allows Equation 1.12 to be rewritten as Equation 1.13

$$\frac{dI_\nu}{d\tau_\nu} = S_\nu - I_\nu \tag{1.13}$$

Which in integral form is given by Equation 1.14

$$dI_\nu(\tau) = \int_0^\tau S_\nu \tau' \exp(\tau' - \tau) d\tau' \tag{1.14}$$

Where τ is the optical depth between the point where I_ν is evaluated and s = -∞ (i.e. spatial infinity along the line of sight). Ideally this integral will be evaluated along all possible lines of sight, but from a modelling perspective, this will be a sampling covering as much space and direction as possible. The determination of the emission and absorption coefficients, j_ν and α_ν is given by the transition rates between rotational and vibrational levels, and the level populations. For a transition from level i to j, j_ν and α_ν are given by Equations 1.15 and 1.16

$$j_{ij}(\nu) = n_i A_{ij} \tag{1.15}$$

$$\alpha_{ij}(\nu) = n_j B_{ji} - n_i B_{ij} \tag{1.16}$$

Where n_i and n_j are the population densities of upper level i and lower level j; A_{ij} is the Einstein coefficient for spontaneous decay from i to j; B_{ji} is the Einstein coefficient for radiatively induced excitation from j to i; and B_{ij} is the Einstein coefficient for radiatively induce de-excitation from i to j. We then find that the source function can be given by Equation 1.17

$$S_{ij} = \frac{n_i A_{ij}}{n_j B_{ji} - n_i B_{ij}} \tag{1.17}$$

We must also consider collisional effects, which can be described with the collisional Einstein coefficients for excitation from level j to i to j, C_{ij} and the inverse for de-excitation, C_{ji}. C_{ij} and C_{ji} are given by Equation 1.18

$$C_{ij} = n_{col} K_{ij}, \qquad C_{ji} = n_{col} K_{ji} \tag{1.18}$$

Where K are the collisional rate coefficients and n_{col} is the density of the collisional partners (usually taken to be H_2). Taking statistical equilibrium, we can determine the level populations through Equation 1.19

$$\sum_{j>i}[n_j A_{ji}+(n_j B_{ji}-n_i B_{ij})J]-\sum_{j>i}[n_i A_{ji}+(n_i B_{ij}-n_j B_{ji})J]+\sum_{j\neq i}[n_j C_{ji}-n_i C_{ji}] = 0 \quad (1.19)$$

Where J is the mean intensity over solid angle, Ω, given by Equation 1.20

$$J = \frac{1}{4\pi}\int I_\nu d\Omega d\nu \quad (1.20)$$

Equations 1.12 to 1.20 are coupled. To solve them, the radiation field and the level populations must be determined simultaneously. This must be completed at each spatial position. This is an exceptionally computationally expensive problem. Many simplifications may be used during the modelling process in order to speed up the process. Here we discuss the methodology of the two models used in this thesis.

1.6.1 RADEX

RADEX is a popular non-LTE radiative transfer code developed by van der Tak et al. (2007). Its methodology is to decouple the radiative transfer calculations from the calculations of the level populations. For this, it uses the escape probability method, which was first introduced for expanding envelopes by Sobolev (1960). A factor, β, is introduced as a measure of the chance that a photon escapes the system. From Equation 1.19, the mean intensity must be found in order to calculate the level populations. If no photons can escape the system (the source is completely opaque), J will equal the mean source function, S. Taking into account β, $J = S(1 - \beta)$. This leaves Equation 1.19 in the form:

$$\sum_{j>i}[n_j A_{ji}\beta - \sum_{j>i}[n_i A_{ji}\beta] + \sum_{j\neq i}[n_j C_{ji} - n_i C_{ij}] = 0 \quad (1.21)$$

Which allows us to solve the level populations and the radiation field separately. The background radiation temperature may also be added here, at a probability of penetrating

the source of 1 - β. We are however still left with the task of estimating β. The first approach by Sobolev (1960) was for expanding stellar envelopes. Here a spherical large velocity gradient (LVG) exists. This means that the line-of-sight velocity in each direction is changed by more than the thermal line width on a short scale. Emission from level i to j at one point in the cloud is not seen at the same frequency at the next point in the cloud. In this case, β is given by Equation 1.22

$$\beta = \frac{1 - \exp(-\tau)}{\tau} \tag{1.22}$$

RADEX allows for the more complex calculation of β in a uniform sphere though Equation 1.23 (Osterbrock 1974)

$$\beta = \frac{1.5}{\tau}[1 - \frac{2}{\tau^2} + (\frac{2}{\tau} + \frac{2}{\tau^2})\exp(-\tau)] \tag{1.23}$$

RADEX uses the last formula to estimate the excitation and radiation field by first guessing the level populations in LTE, giving τ and therefore β. It then calculates new level populations and repeats the process until convergence.

1.6.2 SMMOL

Spherical Multi-Mol (SMMOL) is a code first used in Rawlings and Yates (2001). It is more complex than RADEX in that it does not attempt to decouple the radiation field from the level populations. It iteratively solves all the the equations 1.14 to 1.20. This is completed through the Approximated/Accelerated Lambda Iteration (ALI) method (Scharmer and Carlsson 1985). This is a modified version of Lambda Iteration. In the Lambda Iteration method, a value of J is first found via the Λ operator as Equation 1.24

$$J = \Lambda[S] \tag{1.24}$$

Λ is a matrix operator connecting all points and levels to one another. To solve the radiative transfer numerically, the problem has to be split both in space and frequency and initial level populations have to be assumed (as in RADEX, these are assumed to be LTE).

With these level populations, Λ is constructed by solving Equations 1.14 and 1.20, which are then used to recalculate level populations. This is then repeated until convergence. The only difference with a ALI scheme is that Equation 1.24 is preconditioned for convergence, in order to speed up calculations. ALI introduces the approximated Λ operator, Λ^*, to give Equation 1.25

$$J = \Lambda^*[S] + (\Lambda - \Lambda^*)[S^n] \tag{1.25}$$

Where S^n is the source function on the n^{th} iteration and Λ^* is the diagonal part of Λ. SMMOL completes calculations for 50 points along the line profile and convolves the emergent intensity with the telescope beam at each point. Therefore the output is a direct prediction of the line profile for a given source, observed with a given telescope.

1.7 This Thesis

This thesis focusses on using molecules to determine the properties of active regions of several nearby galaxies. In Chapter 2, we observe the dense gas tracer CS in two nearby starburst galaxies to determine how the conditions of the dense gas varies across the circumnuclear regions in starburst galaxies. In Chapter 3, we further the work of the previous chapter by linking a time and depth dependent chemical model with a molecular line radiative transfer model. In Chapter 4, we present and compare the distribution of two shock tracers, SiO and HNCO, in the Circumnuclear Disk (CND) of NGC 1068. In Chapter 5, we analyse spectra of five transitions, CO$(3-2)$, CO$(6-5)$, CS$(7-6)$, HCN$(4-3)$ and HCO$^+(4-3)$, which are mapped in NGC 1068 with ALMA. A summary and conclusions can be found in Chapter 6.

Chapter 2

Mapping CS in starburst galaxies: Disentangling and characterising dense gas. Part 1: Observations

The work presented in this chapter is based on the paper by Kelly et al. (2015), in collaboration with S. Viti, E, Bayet, R. Aladro and J. Yates.

The formation of stars, in particular the most massive ones, is one of the most important processes regulating the evolution of galaxies; to trace this process, it is crucial to identify the chemical nature of the gas involved and to determine the physical conditions that are more prone to lead to star formation. Massive stars usually form in large concentrations of dense, warm gas (Zinnecker and Yorke 2007). In particular, starburst galaxies are powered by exceptionally high rates of massive star formation, possibly triggered by mergers between galaxies rich in interstellar matter. As discussed in Chapter 1, such events must be relatively short-lived, persisting only until the interstellar gas reservoir is significantly depleted.

Subject to a proper interpretation, observations of molecules in starbursts can be used for many purposes: tracing the leftover reservoir of matter from the star formation process; tracing the star formation process itself; and determining the galaxy energetics through the influence of young stars on the surrounding environments (Kepley et al. 2014; Sliwa et al.

2014). More specifically, and as discussed in Chapter 1, the detection of molecular star-forming gas is one of the most direct ways to measure the star formation rate and activity in a galaxy, allowing us to significantly improve our understanding of galaxy formation and evolution. To date, the wealth of molecular data for at least the nearest galaxies, shows a chemical diversity and complexity that cannot be explained by a one-component, static model, and indicates how relative abundances between molecules may be able to provide insights into the physical distribution of the molecular gas and the energetics of these galaxies.

While some observed molecular transitions may arise from a UV-dominated gas, many can only be explained by the presence of large reservoirs of dense, warm gas (possibly pre-processed on dust grains) that are a part of the star formation process (Gao and Solomon 2004; Onishi et al. 1998). In dense regions (n(H_2) $>10^4$ cm^{-3}), the galactic interstellar radiation field is unimportant for the chemistry since it occurs in conditions of high extinction in the UV. Molecules that are particularly enhanced during the star formation process (including the warm up phase that follows the birth of protostars) are therefore good tracers of the formation of massive stars in galaxies.

From a chemical point of view, sulphur-bearing species have been extensively shown to be particularly enhanced during massive star formation in our own Galaxy, as well as in nearby galaxies (Mauersberger et al. 1989; Martín et al. 2006). As discussed in Chapter 1, among sulphur-bearing species, carbon monosulphide (CS) appears as one of the best tracers of very dense gas (Bronfman et al. 1996). Observationally, CS has been identified in several studies of nearby galaxies (Mauersberger et al. 1989; Martín et al. 2006; Bayet et al. 2008a; Aladro et al. 2011b). Following theoretical studies (Bayet et al. 2008b, 2011), multi-line observations of the CS molecule in nearby (D $<$ 10 Mpc) extragalactic environments were carried out (Bayet et al. 2009a). These studies show that despite the lack of spatial resolution it is possible to point to a reservoir of gas of relatively high density, $\sim 10^5$ cm^{-3}, traced by the *low J* (up to 4) transitions of CS and an even higher ($> 10^6$ cm^{-3}) density component traced by the *high J* (up to 7) transitions. So far surveys have focused on CS detections in the centre of galaxies. However, to gain insight into the distribution of this gas in the environment surrounding the nucleus, galaxy mapping in CS is required. In this work, the spatial distribution of CS in two nearby galaxies, NGC 6946 and NGC 3079, is studied. We detect CS $J = (2-1)$ and $J = (3-2)$ lines in the central region and various offset positions in each galaxy.

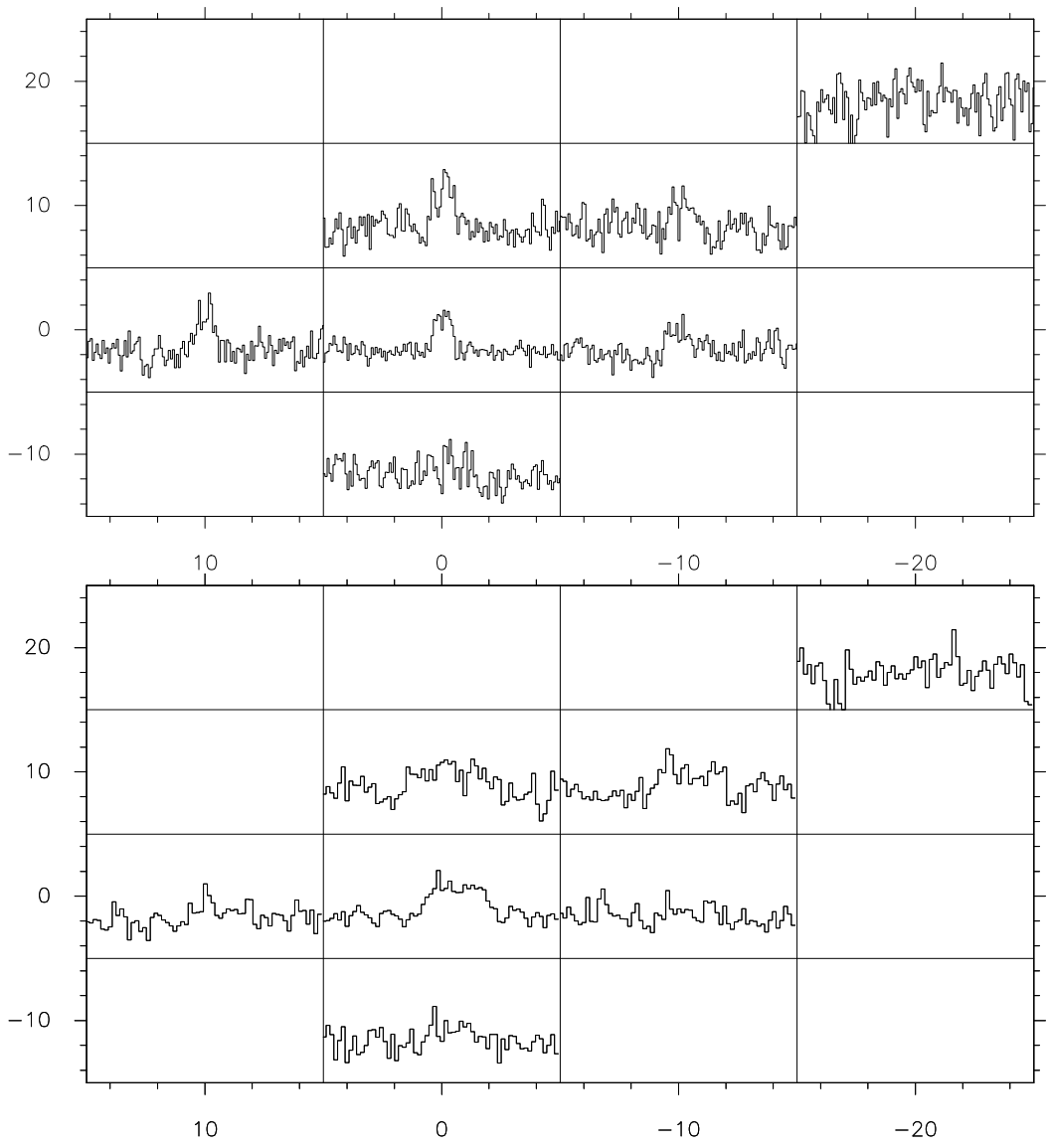

Figure 2.1: Maps of NGC 3079 in, *top*: CS (J = 2 – 1) and; *bottom*: CS (J = 3 – 2). Units are arc seconds. Δv = 8 km s^{-1}

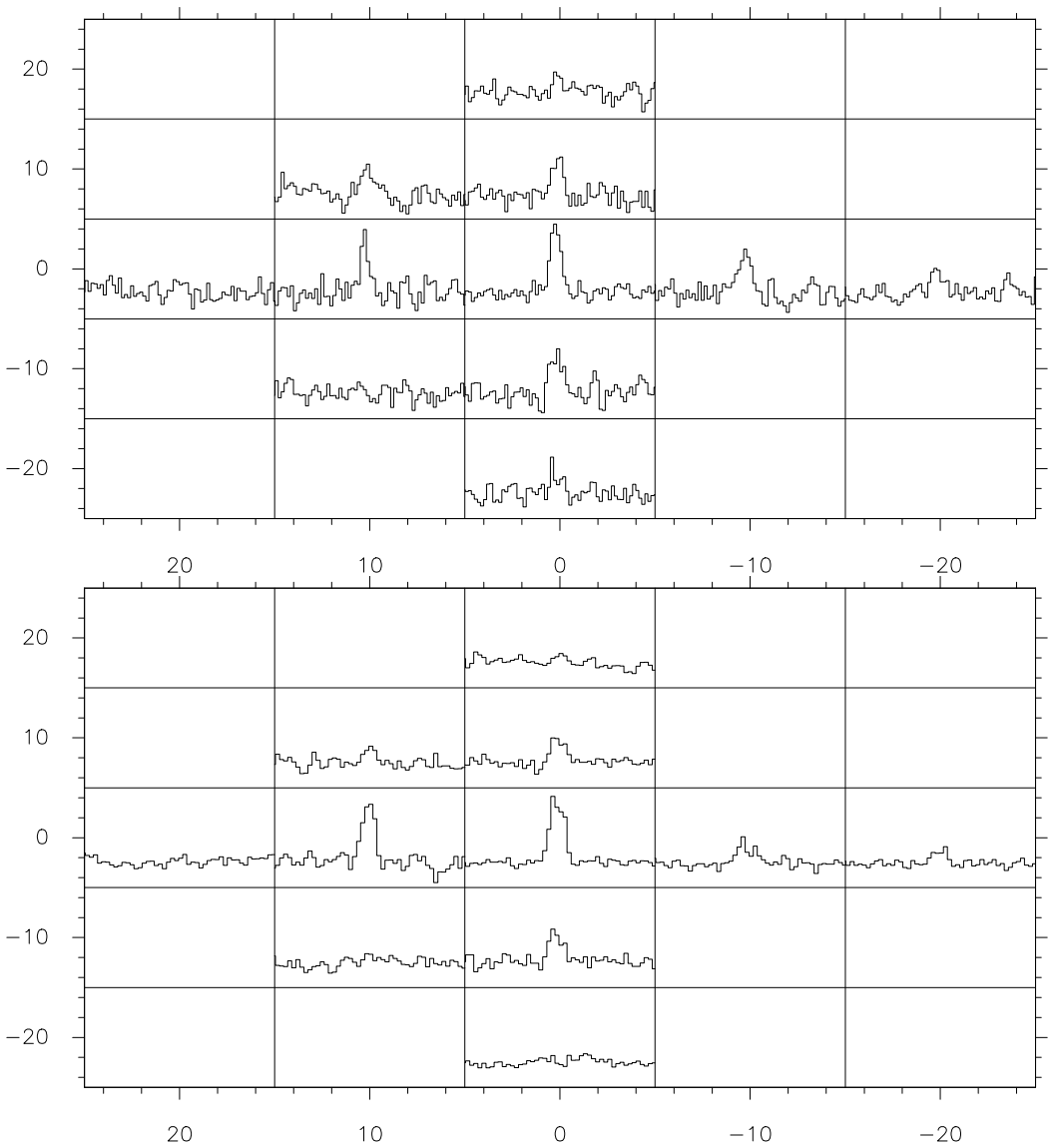

Figure 2.2: Maps of NGC 6946 in *top*: CS (J = 2 – 1) and; *bottom*: CS (J = 3 – 2). Units are arc seconds. Spectral resolution, Δv = 8 km s^{-1}

2.1 Target galaxies

We observed NGC 3079 and NGC 6946, which are discussed in more detail below. The galaxies were chosen as they are known to show starburst activity in their centres, and are both easily observable with the IRAM-30m telescope. We observe CS lines in the central point of each galaxy as well as at offset points staggered at increments of 10″ (Figures 2.2 and 2.1). Further information on both galaxies can be found in Table 2.1.

2.1.1 NGC 3079

NGC 3079 is a nearby Seyfert 2 galaxy with a high inclination angle of 84 degrees and a nuclear bubble of starburst activity (Irwin and Seaquist 1991; Baan and Irwin 1995). At a distance of ∼19 Mpc, we observe 92 pc arcsec^{-1}. As a consequence, we map out to a maximum of 2.8 kpc from our central pointing. Veilleux et al. (1994) discovered the line emitting superbubble in NGC 3079 extending 13″ to the east of the nucleus. Within this bubble, they find extremely violent gas motions ranging over 2000 km s^{-1}, which is also seen to the opposite, western side of the nucleus. In addition to this, unusual excitation shows that shocks may be important and could be a significant contributor to line emission across the bubble. From CO observations, Koda et al. (2002) show that the central 2 kpc region of the galaxy contains a smoothly distributed $\approx 2 \times 10^9$ M$_\odot$ of molecular gas.

2.1.2 NGC 6946

NGC 6946 is a nearby late type spiral galaxy with numerous registered supernovae, also with nuclear starburst activity (Engelbracht et al. 1996). It is not classed as a Seyfert galaxy, but it does show some weak Seyfert activity (Kormendy et al. 2007). At a distance of ∼5.5 Mpc, we observe 27 pc arcsec^{-1}. We map a region up to 810 pc from our central pointing. From CO observations, Leroy et al. (2011) observe that NGC 6946 is also highly rich in molecular gas, both in the central region we observe and out into the details of the spiral arms. Starburst activity in the nucleus of NGC 6946 is more moderate than NGC 3079 (Turner and Ho 1983). NGC 6946 has a small 15″ bulge, within a larger 63″ bar around it. Dense gas has been studied in the central region of this galaxy using tracers HCN (Schinnerer et al. 2007) and HCO$^+$ (Levine et al. 2008). Levine et al. (2008) study the central kpc and find that the density of the gas is roughly constant across the area studied and find that a plausible distribution is of dense clumps bound by self-gravity,

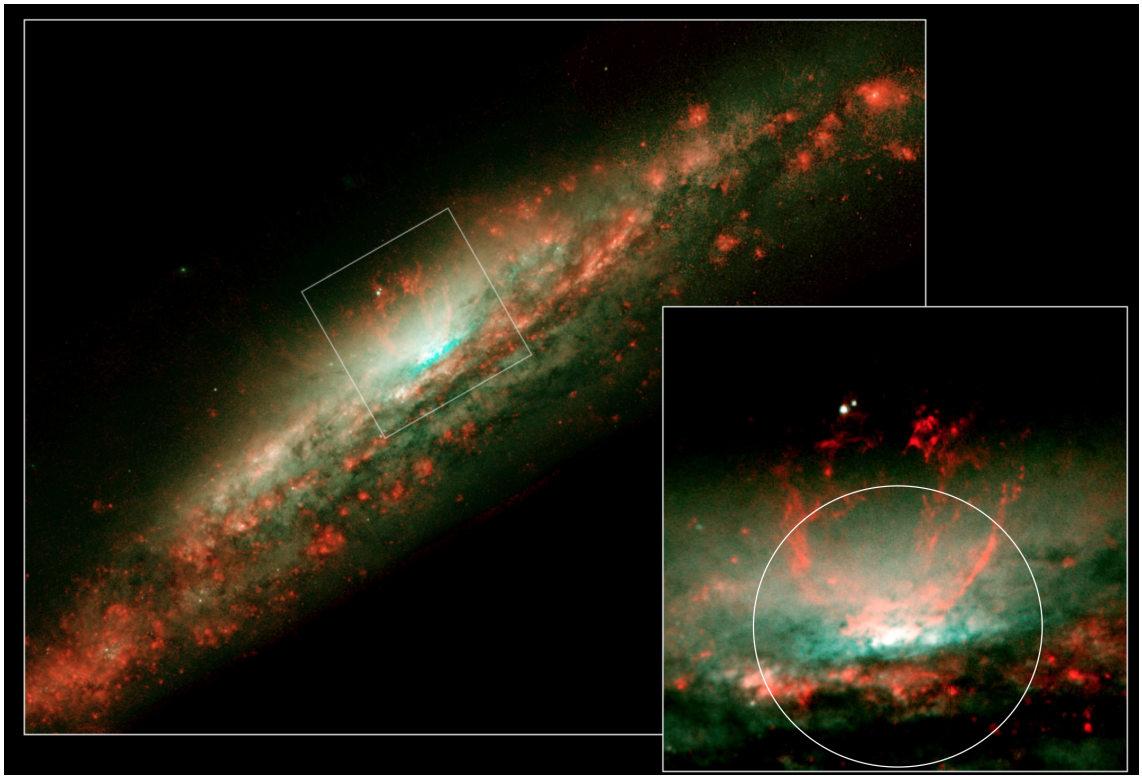

Figure 2.3: Optical image of NGC 3079 - image credit: Hubble, NASA/Space Telescope Science Institute. The approximate observed region is shown with the white circle.

interspersed throughout the lower density molecular gas. However, they also state that it could be possible that the dense gas is homogeneously distributed about the galactic centre. Schinnerer et al. (2007) observed in great detail the central 50 pc of the galaxy and find that the HCN$(1-0)$ intensity distribution in the very centre of the galaxy is centred around two peaks. They find that these peaks correspond quite well to the molecular gas as traced by CO$(2-1)$. They state that one possible interpretation is that these gas peaks are the result of two spiral arms connecting in the central 100 pc. Although there have been detections of CS in the centre of many nearby galaxies (e.g. Zhang et al. 2014), a mapping and full analysis of its distribution in those galaxies has not yet been undertaken. The location and the characteristics of this gas away from galactic centres is crucial to our understanding of the processes and conditions that are necessary for massive star formation to occur.

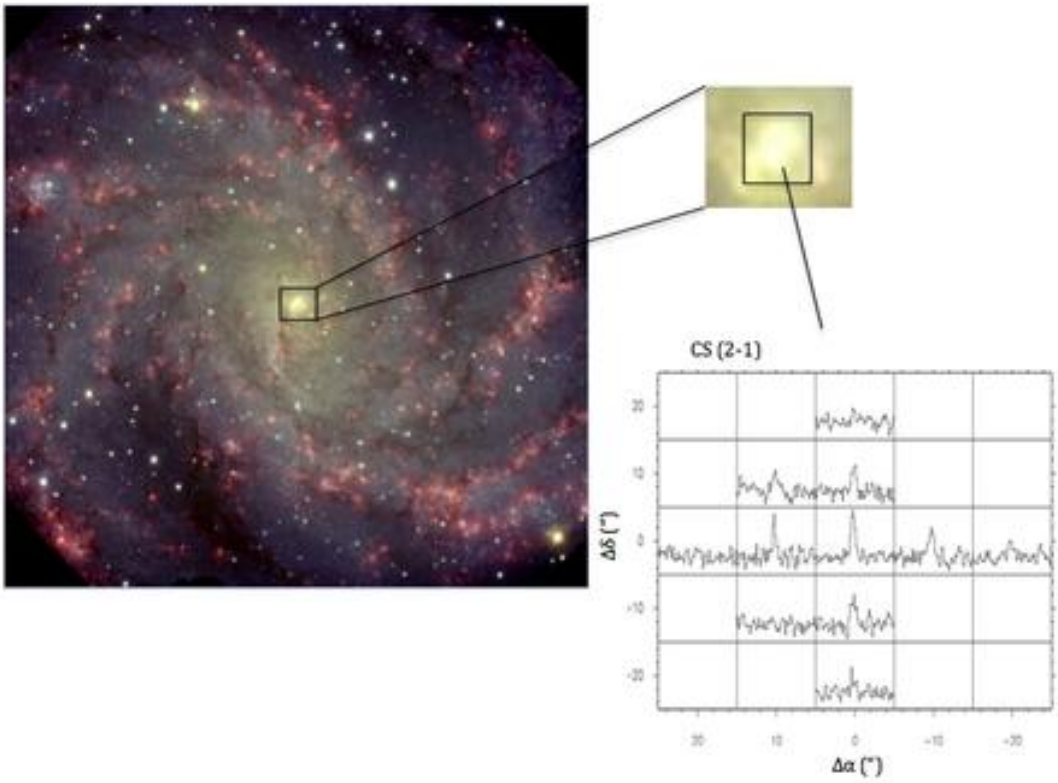

Figure 2.4: Optical image of NGC 6946 - image credit: Subaru, Robert Gendler. The approximate observed region is shown with the CS($2-1$) line at each pointing.

2.2 Observations

The observations were carried out in August 2010 using the IRAM-30m telescope to include the CS($2-1$) and CS($3-2$) lines ($\nu = 97.980$ GHz and 146.969 GHz, respectively). In order to capture other species (methanol, formaldehyde) and isotopologues of CS, each observation was not centred upon the CS line. Instead a line survey from 95.5 GHz to 99 GHz and from 144 GHz to 147.5 GHz was performed in order to detect as many chemical tracers as possible of the dense, star-forming gas. At the observed frequencies of CS($2-1$) and CS($3-2$), IRAM 30m has a HPBW of $\approx 25''$ and $17''$ with main beam efficiencies, $B_{\rm eff}$, of 0.81 and 0.74, respectively. These beam sizes correspond to between approximately 450 pc and 650 pc (NGC 6946), and 1.5 kpc and 2.3 kpc (NGC 3079). During observing, approximately every 2 hours, the pointing, focus and calibration were completed on planets and evolved stars. The pointing error was estimated to be $\leq 3''$. The observations were carried out under varying weather conditions. $T_{\rm sys}$ was between 100 K and 300 K with medium-good weather conditions (τ_{225} <0.15). The observations were done by wobbling

the secondary mirror with a beam throw of 180″ in azimuth. For the observed spectra, the antenna temperature (T_a*) was converted to main beam temperature ($T_{\rm mb}$) using $T_{\rm mb}$ = ($F_{\rm eff}/B_{\rm eff}$)$T_{\rm a}$*, where $F_{\rm eff}$ is the forward efficiency of the telescope (values ranging from 0.93 to 0.95). The channel width spacing was 4 km s^{-1} and has been smoothed down to a 8 km s^{-1}, in order to improve the signal to noise. The EMIR E0 and E1 receivers were used in configurations to optimise observing time. We combined this with the Wilma backend. The data reduction was carried out using the CLASS program, part of GILDAS software[1].

[1]http://www.iram.fr/IRAMFR/GILDAS

Table 2.1: Galaxy properties

Galaxy	RA (J2000)	Dec (J2000)	Velocity (km s^{-1})	Classification	SFR ($M_\odot$ yr^{-1})	Colour (B - V)	StellarMass $M_\odot$
NGC 6946	20:34:51.88	60:09:14.9	48^a	Scd	3.2^b	0.4^d	6.4×10^{10e}
NGC 3079	10:01:57.79	55.40:47.0	1124^a	SB(s)c	6^c	0.7^f	3.3×10^{10g}

References. a) Crook et al. (2007), b) Leroy et al. (2008), c) Walsh et al. (2002), d) Carignan et al. (1990), e) Mineo et al. (2014), f) Gil de Paz et al. (2007), g) Yamagishi et al. (2010)

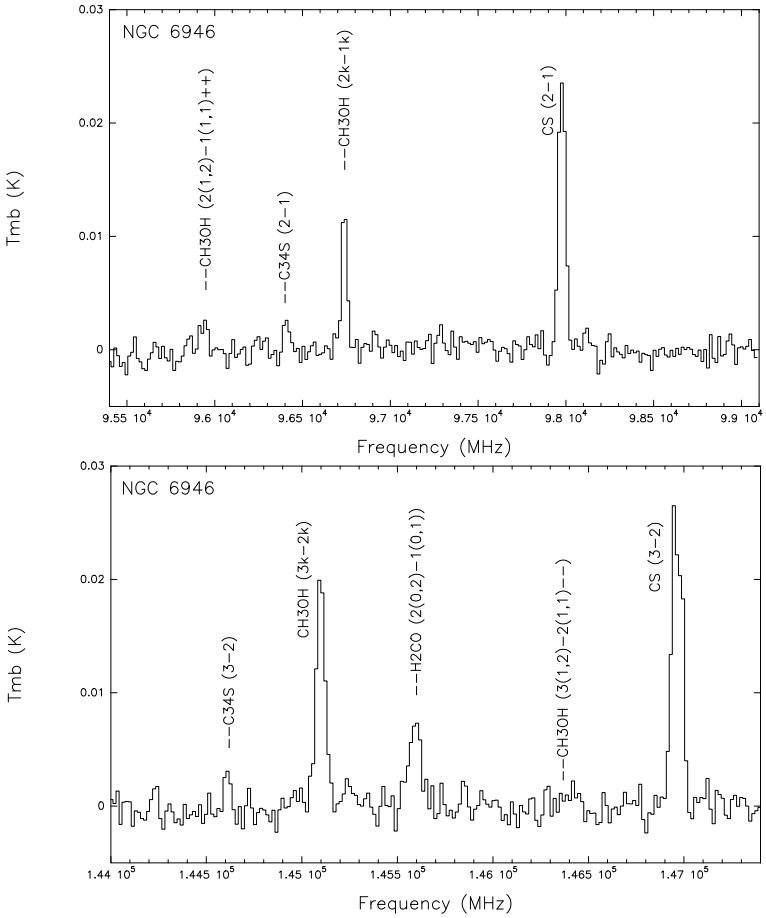

Figure 2.5: Potential detections in centre of NGC 6946

2.3 Results and analysis

2.3.1 Results

Broadly, the strongest emission is seen in the central position (see Tables 2.2 and 2.3 for coordinates) of both galaxies, with two exceptions. In NGC 3079, the CS($2-1$) line is stronger when the beam is offset by +10" in Declination (Dec), and separately, when offset by +10" in Right Ascension (RA).

NGC 6946 shows the strongest emission in the centre, getting weaker out towards offsets of ±20" in all directions. Mauersberger et al. (1989) discovered CS in NGC 6946 and found CS($3-2$) in offset position (RA = $0''$, Dec = $0''$) and (RA = $10''$, Dec = -$10''$) from coordinates α_{2000} = 20:34:51 and δ_{2000} = 60:09:25. This is a few arc seconds from our central position. Our results appear to agree with this. In addition, ours also show

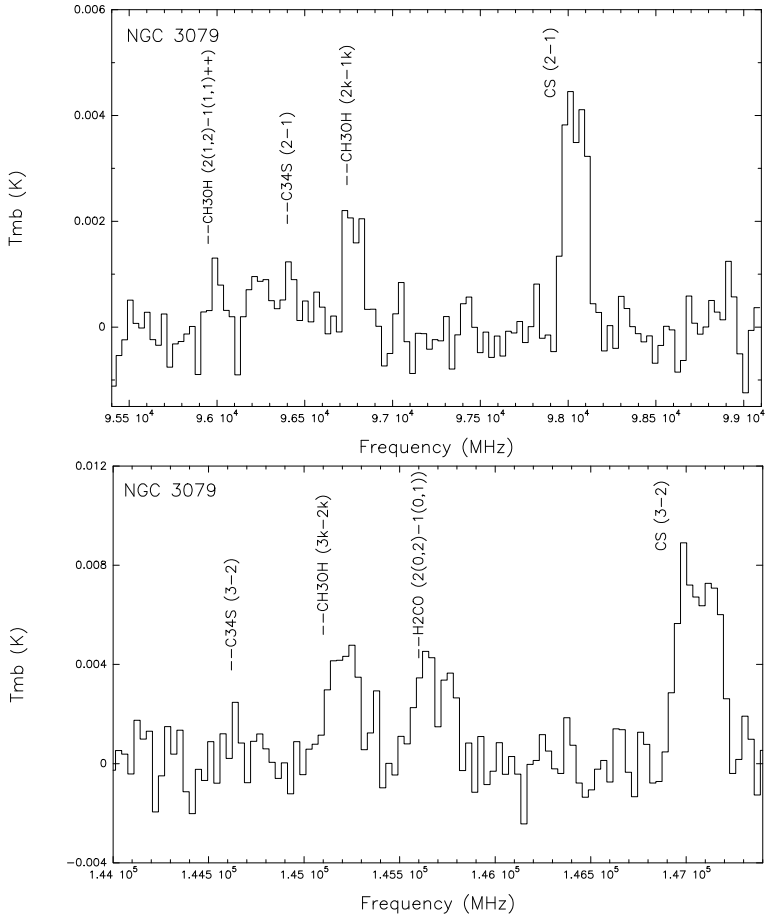

Figure 2.6: Potential detections in centre of NGC3079

strong CS emission from other regions, most notably from the offset of $+10''$ in RA.

We fit single Gaussian profiles to all detections of CS (Figure 2.7 and 2.8). We also detect methanol (CH_3OH) and formaldehyde (H_2CO) in both galaxies. The isotoplogue of CS, $C^{34}S$ was marginally detected, also in both galaxies. Tables 2.2 and 2.3 show the Gaussian fit parameters for these detections.

Since we have no prior knowledge as to the location of CS emission, we consider each position as separate and assume the source fills the beam. The signal-to-noise (S/N) of CS in some offset positions is less than 3, and therefore they are considered as tentative detections. Still, we used them in our analysis, as the fitted line widths and velocity positions agree with the values expected. NGC 6946 and NGC 3079 angular sizes are $\sim 12'$ x $8'$ and $\sim 4.5'$ x $1'$ in the IR (Skrutskie et al. 2006) so observations focus on the area surrounding the centre. It is interesting to note that in offset positions of just ± 20" in any direction in both galaxies we fail to see (or only marginally detect) CS.

Ball et al. (1985) found a bar structure, running approximately north-south in NGC

6946 of size 11" by 55". More material in this bar may mean that there is more dense gas, so it might be expected that some CS is detected further away from the centre, in at least one direction.

Table 2.2: NGC 6946 observational parameters and Gaussian fits. For a two component fit, NGC 6946-1 corresponds to the component at lower velocity and NGC 6946-2 the higher velocity component.

Source	Line	ν	Offset	Offset	$\int(T_{mb}d\nu)$	FWHM	T_{peak}	rms	v_{peak}
		(GHz)	RA (")	Dec (")	(K km s^{-1})	(km s^{-1})	(mK)	(mK)	(km s^{-1})
NGC 6946	CS(2 − 1)	97.980	0	0	3.9 ± 0.1	140.1 ± 4.2	25.9	1.6	60.4 ± 1.7
			0	-10	2.2 ± 0.1	136.6 ± 8.6	15.0	2.1	69.0 ± 4.1
			0	+10	1.9 ± 0.1	146.8 ± 10.9	12.2	2.1	56.1 ± 4.7
			+10	0	2.9 ± 0.1	139.2 ± 7.3	19.8	2.5	47.0 ± 3.6
			-10	0	2.1 ± 0.1	133.8 ± 7.0	14.8	2.0	70.4 ± 3.5
			-20	0	1.6 ± 0.1	157.6 ± 13.7	9.3	1.7	70.3 ± 6.4
			+20	0	1.0 ± 0.1	150.1 ± 18.1	6.3	2.2	33.9 ± 10.3
			+10	+10	1.4 ± 0.1	140.0 ± 15.7	9.1	2.3	41.6 ± 6.2
			+10	-10	-	-	-	-	-
			0	-20	1.1 ± 0.1	123.5 ± 15.3	8.6	1.9	71.8 ± 6.6
			0	+20	0.9 ± 0.1	126.0 ± 22.4	6.4	2.0	35.0 ± 10.1
	CS(3 − 2)	146.969	0	0	3.8 ± 0.1	135.2 ± 3.7	26.3	2.1	63.3 ± 1.8
			0	-10	1.7 ± 0.2	124.2 ± 16.5	12.7	3.3	74.0 ± 6.7
			0	+10	1.4 ± 0.2	128.5 ± 15.8	10.3	3.9	54.1 ± 7.7
			+10	0	3.1 ± 0.2	114.6 ± 8.8	25.5	4.9	48.1 ± 4.1
			-10	0	1.2 ± 0.2	160.8 ± 7.2	7.3	3.4	79.7 ± 11.4
			-20	0	0.7 ± 0.1	124.3 ± 20.1	5.3	2.8	38.4 ± 11.3

			+20	0	-	-	-	-	-
			+10	+10	0.7 ± 0.1	98.1 ± 19.8	6.9	3.5	35.4 ± 11.0
			+10	-10	-	-	-	-	-
			0	-20	-	-	-	-	-
			0	+20	0.4 ± 0.1	93.6 ± 29.8	3.9	3.0	32.9 ± 15.1
	$C^{34}S(2-1)$	96.413	0	0	0.4 ± 0.1	122.5 ± 25.9	3.3	1.4	65.9 ± 12.7
	$C^{34}S(3-2)$	144.617	0	0	0.3 ± 0.1	68.3 ± 16.2	3.6	2.1	64.7 ± 9.8
	$H_2CO(2(0,2)\text{-}1(0,1))$	145.603	0	0	1.3 ± 0.1	161.2 ± 16.4	7.6	2.0	73.0 ± 6.2
	$CH_3OH(2_k-1_k)$	96.745	0	0	1.5 ± 0.1	97.8 ± 6.2	14.5	1.6	71.5 ± 2.5
	$CH_3OH(3_k-2_k)$	145.125	0	0	2.4 ± 0.1	106.0 ± 5.0	21.4	2.1	105.3 ± 1.8
NGC 6946-1	$CS(2-1)$	97.980	0	0	1.25 ± 0.2	65.1 ± 7.2	18.0	2.1	45.1 ± 3.3
			0	-10	0.6 ± 0.1	49.9 ± 10.0	11.3	2.1	-0.8 ± 5.1
			0	+10	-	-	-	-	-
			+10	0	1.23 ± 0.2	61.1 ± 9.6	19.1	2.5	16.5 ± 5.3
			-10	0	0.68 ± 0.2	59.5 ± 9.4	10.7	2.0	12.8 ± 5.2
			-20	0	-	-	-	-	-
			+20	0	0.4 ± 0.1	42.7 ± 9.5	9.7	2.2	-5.7 ± 5.0
			+10	+10	-	-	-	-	-
			+10	-10	-	-	-	-	-
			0	-20	-	-	-	-	-
			0	+20	-	-	-	-	-

	CS(3 − 2)	146.969	0	0	1.2 ± 0.1	48.1 ± 3.9	23.0	2.1	8.0 ± 1.8
			0	-10	-	-	-	-	-
			0	+10	-	-	-	-	-
			+10	0	-	-	-	-	-
			-10	0	-	-	-	-	-
			-20	0	0.4 ± 0.1	46.6 ± 8.5	7.9	2.8	1.4 ± 5.1
			+20	0	-	-	-	-	-
			+10	+10	-	-	-	-	-
			+10	-10	-	-	-	-	-
			0	-20	-	-	-	-	-
			0	+20	-	-	-	-	-
NGC 6946-2	CS(2 − 1)	97.980	0	0	2.5 ± 0.2	86.7 ± 7.8	26.6	2.1	101.2 ± 4.1
			0	-10	1.5 ± 0.1	80.4 ± 8.2	17.8	2.1	88.0 ± 4.0
			0	+10	-	-	-	-	-
			+10	0	1.6 ± 0.3	73.3 ± 13.5	19.9	2.5	94.9 ± 3.2
			-10	0	1.4 ± 0.1	77.8 ± 9.7	16.8	2.0	96.2 ± 3.5
			-20	0	-	-	-	-	-
			+20	0	0.5 ± 0.1	83.0 ± 19.3	6.0	2.2	85.7 ± 9.9
			+10	+10	-	-	-	-	-
			+10	-10	-	-	-	-	-
			0	-20	-	-	-	-	-

		0	+20		-		-	-		-
	CS(3 – 2)	146.969	0	0	2.4 ± 0.1	79.2 ± 5.1	28.6	2.1	87.1 ± 1.9	
			0	-10	-		-	-		-
			0	+10	-		-	-		-
			+10	0	-		-	-		-
			-10	0	-		-	-		-
			-20	0	0.3 ± 0.1	54.6 ± 21.4	5.6	2.8	83.4 ± 7.4	
			+20	0	-		-	-		-
			+10	+10	-		-	-		-
			+10	-10	-		-	-		-
			0	-20	-		-	-		-
			0	+20	-		-	-		-

Table 2.3: NGC 3079 observational parameters and Gaussian fits. For a two component fit, NGC 3079-1 corresponds to the component at lower velocity and NGC 3079-2 the higher velocity component.

Source	Line	ν (GHz)	Offset RA (")	Offset Dec (")	$\int(T_{mb}d\nu)$ (K km s^{-1})	FWHM (km s^{-1})	T_{peak} (mK)	rms (mK)	v_{peak} (km s^{-1})
NGC 3079	$CS(2-1)$	97.980	0	0	2.2 ± 0.2	429.5 ± 34.6	4.7	1.4	1153 ± 15
			0	-10	-	-	-	-	-
			0	+10	2.7 ± 0.4	464 ± 72	5.4	2.5	1213 ± 26
			+10	0	2.4 ± 0.3	472 ± 67	4.8	2.6	1149 ± 26
			-10	0	-	-	-	-	-
			-10	+10	-	-	-	-	-
			-20	+20	-	-	-	-	-
	$CS(3-2)$	146.969	0	0	4.3 ± 0.3	484.9 ± 40.8	8.2	2.5	1140 ± 14
	$H_2CO(2(0,2)\text{-}1(0,1))$	145.603	0	0	1.9 ± 0.2	444 ± 59	4.0	2.7	1190 ± 28
	$CH_3OH(2_k - 1_k)$	96.745	0	0	0.9 ± 0.1	362 ± 61	2.3	1.1	1240 ± 31
	$CH_3OH(3_k - 2_k)$	145.125	0	0	2.0 ± 0.3	394 ± 64	4.7	3.2	1158 ± 27
NGC 3079-1	$CS(2-1)$	97.980	0	0	0.9 ± 0.2	208.3 ± 42.1	4.3	1.5	1010 ± 21
	$CS(3-2)$	146.969	0	0	2.0 ± 0.4	244.4 ± 41.1	7.8	2.5	994 ± 22
NGC 3079-2	$CS(2-1)$	97.980	0	0	1.2 ± 0.2	222.0 ± 35.4	4.8	1.5	1270 ± 20
	$CS(3-2)$	146.969	0	0	2.1 ± 0.4	230.3 ± 37.6	8.5	2.5	1279 ± 19

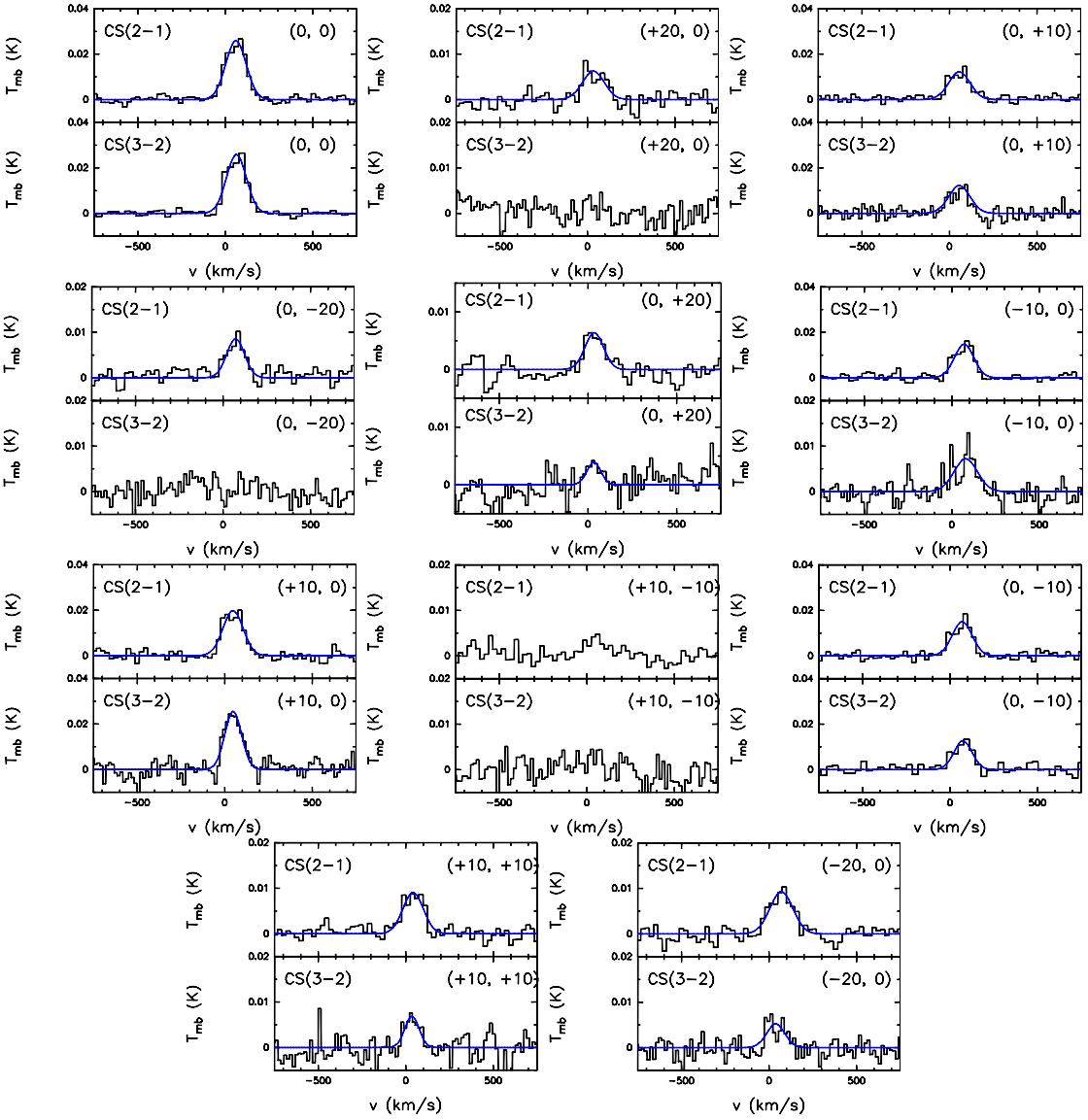

Figure 2.7: Single component fits for CS(2 − 1) and CS(3 − 2) in NGC 6946. Label in right corner shows offset in RA (″) and Dec (″) from central position.

2.3.2 Line analysis

Under the assumption that emission from different lines is coming from the same regions, we calculate velocity integrated line ratios for some species. We note that this assumption may not hold completely true, as we shall see later in Section 2.3.3, but include the values as they may be instructive. We calculate the ratio of CS(3 − 2) / CS(2 − 1) where possible, accounting for the difference in beam sizes between the two detections. Since we only record detections of lines other than CS(2 − 1) in our central pointing in NGC

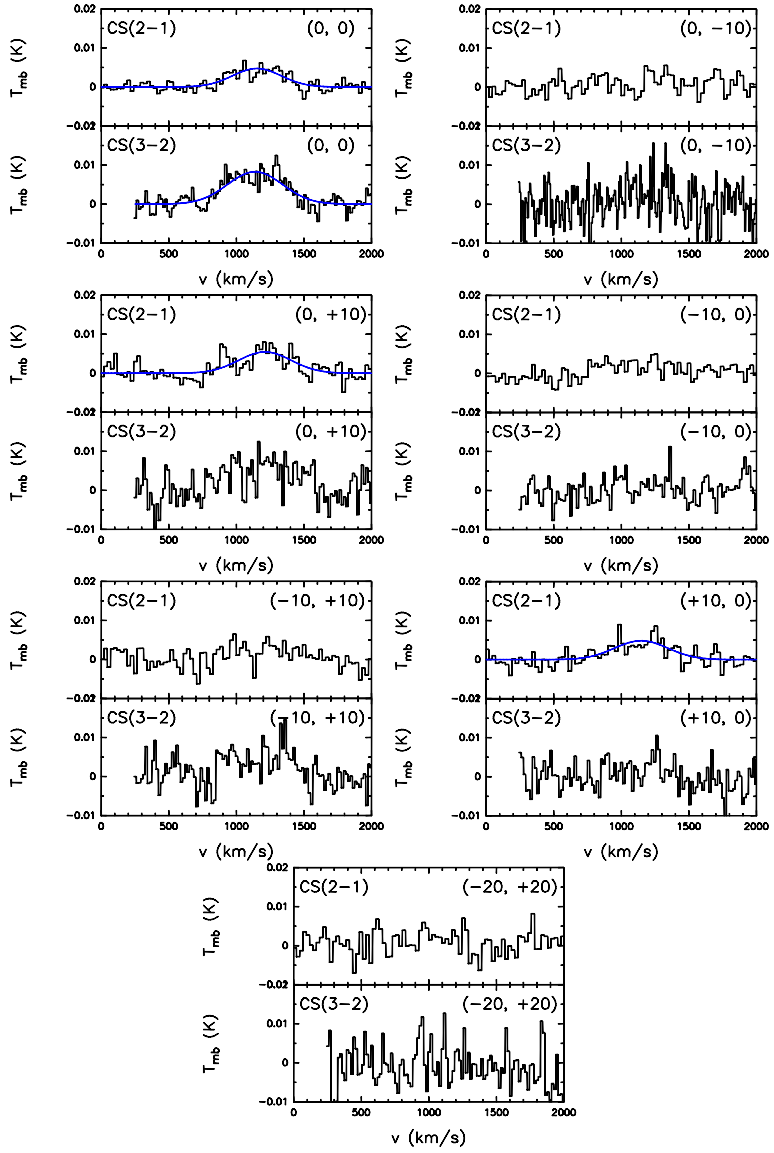

Figure 2.8: Single component fits for CS(2 − 1) and CS(3 − 2) in NGC 3079. Label in right corner shows offset in RA (″) and Dec (″) from central position.

3079, we only find ratios for the central position in this galaxy. These are listed in Table 2.4, together with ratios in the central position of NGC 6946. In NGC 3079 we see much stronger emission from CS(3 − 2) when compared to all other lines. In the central position, the CS(3 − 2) / CS(2 − 1) ratio is approximately double the equivalent in NGC 6946.

CS(3 − 2) / CS(2 − 1) ratios in NGC 6946 are shown in Table 2.5. The same is seen when comparing CS(3 − 2) to other lines. In NGC 6946 the CS(3 − 2) / CS(2 − 1) ratio is highest at offset +10" in RA (approximately 270 pc). Other than this, the general trend is for these values to drop as the beam is pointed away from the galactic centre, although the value is always >1.

Although we have treated lines as being a single peak, when the data is less smoothed, detected CS lines in both galaxies show a double peak profile (Figure 2.9 and 2.10), although this is not very clear in the tentative detections. Costagliola et al. (2011) observe another dense gas tracer line, HCN(1 − 0) in NGC 3079. Their data show signs of a similar line profile, although it is not discussed. Of their sample of 19 galaxies, this profile can be seen in three: NGC 3079, NGC 4388 and UGC 5101, all Seyfert galaxies. However, we note that there are Seyferts in their sample that do not show this profile. We consider a possible cause of this to be a rotating torus of dense gas around the nucleus, leading to red- and blue-shifted components. Profiles like these have been observed in NGC 253 (Martín et al. 2005) (also a Seyfert) leading the authors to a similar conclusion. However, we note that this might be due to other factors, such as self absorption.

The profiles seen in NGC 6946 are also possibly due to rotation. Tsai et al. (2013) find that ionised gas velocities shift from $V_{LSR} \sim 30$ km s^{-1} in the east to $V_{LSR} \sim 90$ km s^{-1} in the west. Schinnerer et al. (2006) find a higher velocity gradient of >100 km s^{-1} between east and west in the molecular gas, as traced by CO. The regions "east" and "west" are both within our beam, and the difference between the peaks of our two components is $\sim$ 100 km s^{-1}. To conclude that this is the source of our double-horn profiles, we must assume that the CS emission we see is either coming form the same gas component as CO emission, or, more likely the dense gas as traced by CS is moving with the larger molecular gas clouds.

Analysing the CS double-horn profile, we see that the lower velocity (red-shifted) component in both galaxies is narrower, possibly meaning that the gas moving away has a lower turbulent velocity than the gas coming towards. We show the double-horn Gaussian fits for the centre of each galaxy and compare with the isotopolgue C^{34}S in NGC 6946

(Figure 2.9). Detections of isotopologues were marginal (<2 σ) in NGC 3079 so only the double-horn CS profile is fitted (Figure 2.10). These data have been included with the single peak data in Table 2.2 and 2.3. For both single and double peak profiles, a good agreement can be found between the Gaussian fits and the observations. Where possible we fit to the double peak but we also calculate for a single fit. If a double fit is not possible (as with many of the offset points), we only fit a single Gaussian. For double fits we have designated the component at lower velocity 1 and the higher velocity component 2 (e.g. NGC 6946-1 and NGC 6946-2).

Table 2.4: Other line ratios for central pointing

Galaxy	Lines	Ratio
NGC 6946	CS(3 − 2) / CS(2 − 1)	3.2 ± 0.2
	$CH_3OH(2_k - 1_k)$ / CS(2 − 1)	0.4 ± 0.1
	$CH_3OH(3_k - 2_k)$ / CS(3 − 2)	0.6 ± 0.1
	$CH_3OH(2_k - 1_k)$ / CS(3 − 2)	0.1 ± 0.006
	$CH_3OH(3_k - 2_k)$ / CS(2 − 1)	2.0 ± 0.1
NGC 3079	CS(3 − 2) / CS(2 − 1)	6.7 ± 0.3
	$CH_3OH(2_k - 1_k)$ / CS(2 − 1)	0.4 ± 0.1
	$CH_3OH(3_k - 2_k)$ / CS(3 − 2)	0.5 ± 0.1
	$CH_3OH(2_k - 1_k)$ / CS(3 − 2)	0.06 ± 0.003
	$CH_3OH(3_k - 2_k)$ / CS(2 − 1)	3.0 ± 0.2

Values are the ratio between the velocity integrated Gaussian fit to the profile for each line. The errors are propagated from the error in fitting each line

2.3.3 LTE analysis

We used two methods to perform an analysis of our observations under the assumption of Local Thermodynamic Equilibrium (LTE). Firstly, we used the rotational diagram method (Goldsmith and Langer 1999), which allows us to calculate a temperature and column density. Under LTE we assume that the observed molecules are thermally excited and therefore rotational excitation should follow a Maxwell-Boltzmann distribution. The emission can therefore be used as a measure of the local temperature. This assumes firstly that the density of the region is above the critical density (n_{crit}) of the molecule. This is given as:

$$n_{crit} = \frac{A_{ul}}{\gamma_{ul}} \tag{2.1}$$

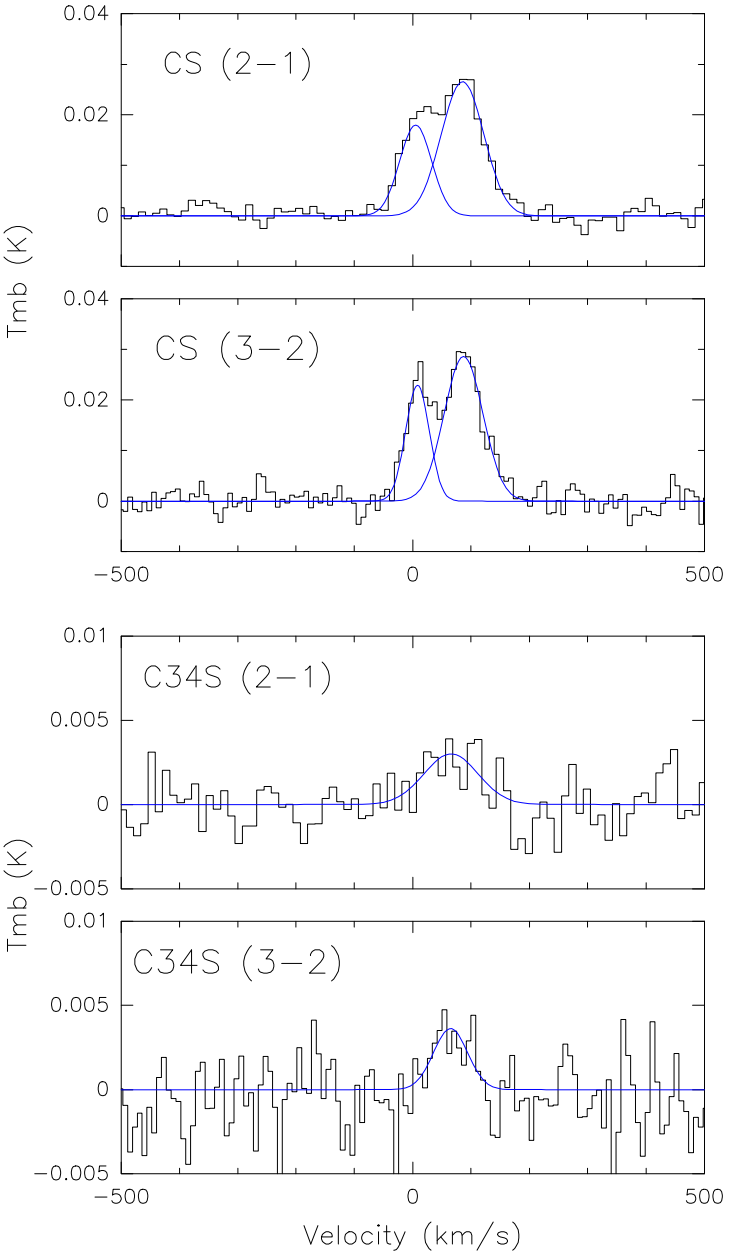

Figure 2.9: CS detections in the centre of NGC 6946. $^{12}C^{32}S$ displaying a double-horn profile.

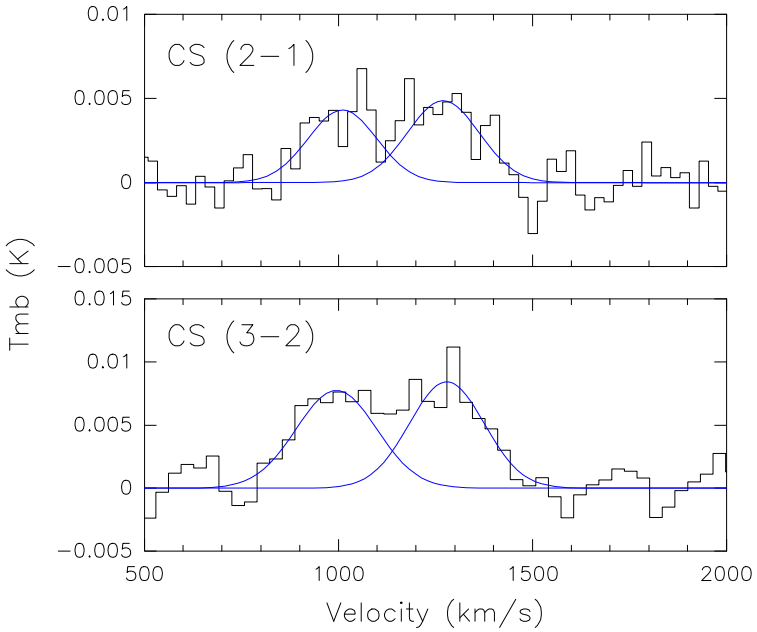

Figure 2.10: CS detections in the centre of NGC 3079 displaying a double-horn profile.

Where A_{ul} is the Einstein A-coefficient for radiative de-excitation and γ_{ul} is the rate of collisional de-excitation, both from levels u to l. At densities significantly above n_{crit} the rotational excitation temperature (T_{rot}) approaches the kinetic temperature of the gas (i.e. the line is thermalised). This LTE analysis also assumes that the emission is optically thin. We are also assuming the temperature is uniform, and therefore we are calculating an average temperature for our observed regions. Under these assumptions the following equation is true:

$$\frac{N_u}{g_u} = 8.6 \times 10^{37} \frac{8\pi}{hc^3} \frac{W}{\nu \mu^2 S} = \frac{N}{Q(T_{rot})} \exp(\frac{E_u}{T_{rot}}) \tag{2.2}$$

Where N_u is the column density of the upper energy level u, g_u is the degeneracy of the upper energy level, W is the integrated flux $= \int T_{\rm mb} {\rm d}V$, V is velocity in km s^{-1}, ν is the frequency in GHz, μ is the dipole strength in Debye, S is the line strength, N is the total column density in cm^{-2}, E_u is the energy of the upper level in K and Q is the partition function. This allows us to plot N_u/g_u against E_u. The derivative is then a function of T_{rot} and the intercept with the y-axis allows the calculation of N. This method assumes the gas is in LTE but since the gas may not be thermalised the kinetic temperature may be greater than the rotational temperature (Goldsmith and Langer 1999).

Methanol has a critical density for low-J transitions at low temperature of $\approx 10^5$ cm^{-3}. This is only a little below CS ($n_{crit} \approx 1 \times 10^6$ for low-J transitions at low temperature). Methanol can therefore also be considered a high density gas tracer. We use this molecule to constrain a minimum temperature with which to begin an LTE analysis using CS. We do this only for the centre of NGC 6946, as lines here are strong enough to allow the use of this technique. We detected two bands of methanol in our spectra (J = 2_k - 1_k, 3_k - 2_k). Martín et al. (2006) used a method to separate individual transitions in these bands using the ratios of Einstein coefficients A'_{ul} and A''_{ul}, upper energy levels E'_u and E''_u and degeneracies g'_u and g''_u. This is shown in the equation 2.3, assuming two transitions in the band.

$$\frac{W'}{W''} = \frac{\nu''^2 A'_{ul} g'_u}{\nu'^2 A''_{ul} g''_u} e^{(E''_u - E'_u)/kT^0_{rot}}, \tag{2.3}$$

Where T^0_{rot} is the estimate for the rotational temperature. The method works on the basis that in LTE we should see a linear regression in the rotation diagram, the correct temperature is the one that produces the best fit. We therefore iterate over many temperatures using both methanol bands until we find a best fit. The methanol rotation diagram for the centre of NGC 6946 (Figure 2.11) shows a fit to a temperature of 14 K. We show no error bars as they may be misleading, due to the error in this method being larger than the calibration error on the telescope.

In order to obtain an estimation of the CS column density, we use only our CS$(2-1)$ detections, as we do not detect CS$(3-2)$ in as many locations as CS$(2-1)$. This allows us to calculate values in locations where we have only one detection. In the same way as with the rotational diagram method, we assume LTE conditions and optically thin emission. However, it does not constrain a temperature. A rotational temperature must therefore be assumed. With methanol, we obtained a kinetic temperature of 14 K. This is a lower limit because all the levels may not be thermalised. Column densities are therefore calculated for 15 K, 50 K and 300 K. These calculations have been carried out using both single- and (where possible) double-fits. A double horned profile could be present due to a rotating torus of gas about the centre of the galaxy. However, this profile is not clear and does not appear in all observations. Therefore, while we show the double fit parameters for completeness, the single fits will be used as the basis for this Chapter and for Chapter 3.

All values are listed in Table 2.6. These results will be useful as a guide to future chemical modelling, presented in Chapter 3 as they represent a lower limit to the column density of CS as all levels may not be thermalised and we lack information about the optical depth. We will therefore be able to discard chemical models which show a column density of CS of less than these values at a particular temperature. Our LTE results show that reasonable values of column density (N(CS) $\approx 10^{14}$ cm^{-2}) are seen up to temperatures of 300 K.

Table 2.5: CS$(3-2)$/CS$(2-1)$ ratios in NGC 6946

Dec offset (") \ RA offset (")	20	10	0	-10	-20
20			1.5		
10		1.7	2.4		
0		3.5	3.2	1.9	1.5
-10			2.5		
-20					

2.4 Conclusions

CS emission has been mapped across two nearby starburst galaxies - NGC 3079 and NGC 6946. We observe the low-J, CS$(2-1)$ and CS$(3-2)$ transitions. In the centre of both galaxies, we see evidence of a double-horn line profile in CS$(3-2)$ and CS$(2-1)$. We conclude that this may be either down to the kinematics of the gas, as in other galaxies (i.e. NGC 253), or self-absorption. We tabulate observational data including the FWHM, intensity and peak velocity of each line at each pointing, for both galaxies. We use these data to complete LTE calculations. We first use methanol detections at the central pointing to determine a lower limit to the kinetic temperature in NGC 6946 of 14 K. Then, using CS detections at each pointing, LTE column densities were derived for temperatures between 15 K and 300 K across both galaxies, resulting in values between N(CS) $= 3 \times 10^{12}$ cm^{-2} and N(CS) $= 2 \times 10^{14}$ cm^{-2} in NGC 6946 and values between N(CS) $= 5 \times 10^{12}$ cm^{-2} and N(CS) $= 1 \times 10^{14}$ cm^{-2} in NGC 3079. Since these values are made under the approximation of LTE, and only for estimates of the temperature, robust

Table 2.6: LTE Column Densities

Source	Line	Offset RA (")	Offset Dec (")	N(CS) x 10^{14} T = 15 K	T = 50 K	T = 300 K
NGC 6946	CS(2 − 1)	0	0	0.176	0.42	2.25
		0	-10	0.099	0.24	1.27
		0	+10	0.087	0.21	1.11
		+10	0	0.133	0.32	1.71
		-10	0	0.096	0.23	1.22
		-20	0	0.071	0.17	0.91
		+20	0	0.046	0.11	0.58
		+10	+10	0.062	0.15	0.79
		+10	-10	-	-	-
		0	-20	0.051	0.12	0.66
		0	+20	0.039	0.09	0.5
NGC 6946-1	CS(2 − 1)	0	0	0.057	0.14	0.73
		0	-10	0.027	0.07	0.35
		0	+10	-	-	-
		+10	0	0.056	0.14	0.72
		-10	0	0.031	0.07	0.4
		-20	0	-	-	-
		+20	0	0.02	0.05	0.26
		+10	+10	-	-	-
		+10	-10	-	-	-
		0	-20	-	-	-
		0	+20	-	-	-
NGC 6946-2	CS(2 − 1)	0	0	0.111	0.27	1.43
		0	-10	0.069	0.17	0.89
		0	+10	-	-	-
		+10	0	0.071	0.17	0.9
		-10	0	0.063	0.15	0.81
		-20	0	-	-	-
		+20	0	0.024	0.06	0.31
		+10	+10	-	-	-
		+10	-10	-	-	-
		0	-20	-	-	-
		0	+20	-	-	-
NGC 3079	CS(2 − 1)	0	0	0.098	0.24	1.26
		0	-10	0.031	0.08	0.4
		0	+10	0.122	0.29	1.56
		+10	0	0.11	0.26	1.41
		-10	0	0.067	0.16	0.86
		-10	+10	0.074	0.18	0.95
		-10	+20	0.045	0.11	0.58

"-" indicates no fit was possible

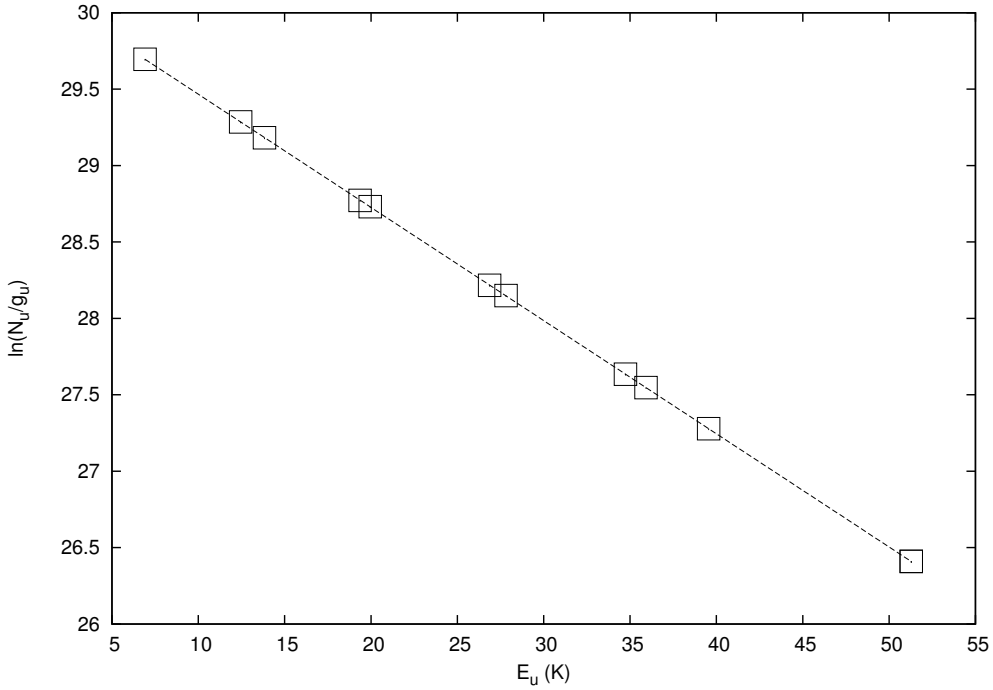

Figure 2.11: Rotation diagram for methanol in centre of NGC 6946. The parameters for this diagram are T = 13.6 K and N(CH_3OH) = 4.6×10^{14} cm^{-2}.

calculations should be carried out to constrain the conditions of the star-forming dense gas in each galaxy. We complete this further analysis in Chapter 3.

This page was intentionally left blank

Chapter 3

Mapping CS in starburst galaxies: Disentangling and characterising dense gas. Part 2: Modelling

The work presented in this chapter is based on the paper by Kelly et al. (2015), in collaboration with S. Viti, E, Bayet, R. Aladro and J. Yates.

In the previous Chapter, we made observations of the two nearby starburst galaxies, NGC 6946 and NGC 3079. We mapped both galaxies in the dense gas tracer, CS. We took pointings at the centre of each galaxy and then at offsets of 10″ out to 20″. We now complete a more detailed modelling with the aim of determining more accurately the conditions of the dense star-forming gas. This is completed through a non-LTE radiative transfer modelling which takes as an input the final abundance of CS from a time-dependent chemical model.

3.1 Non-LTE analysis

3.1.1 Chemical modelling

A time-dependent chemical model is necessary in order to take into consideration the history of the gas. Here we are looking at a dense core environment. The CS molecule

has numerous formation and destruction routes (see, for example, the UMIST database - McElroy et al. 2013, and section 3.1.2). These are dependent both directly on the physical conditions and also on the formation and destruction of precursor species, both in the gas and solid (i.e. dust grain surface) phases. It is therefore impossible to uncouple the physics of the dense molecular regions observed, with the chemistry which occurred during their formation.

Table 3.1: The species that were included in the chemical model. Species preceded by "M" are grain mantle surface species.

Species
e^-, H, H^+, H_2, H_2^+, H_3^+, O, O^+, OH^+, OH, O_2, O_2^+, H_2O, H_2O^+, H_3O^+, O_2H^+
H_2CN, C, C^+, CH, CH^+, CH_2, CH_2^+, CH_3, CH_3^+, CH_4, CH_4^+ CH_5 CH_5^+, C_2, C_2^+
C_2H, C_2H^+, $C_2H_2^+$, C_3^+ CO, CO^+, HCO, HCO^+, H_2CO, H_2CO^+, H_3CO^+
HCO_2^+, S, S^+, HS, HS^+, H_2S H_2S^+, H_3S^+ OCS, OCS^+, S_2, S_2^+, HS_2, HS_2^+, $H_2S_2^+$, CS
CS^+, HCS, HCS^+, H_2CS, H_2CS^+, SO, HSO^+, SO_2 SO_2^+, HSO_2^+, H_3CS^+
$HOCS^+$, O_2H, CO_2, He, He^+, HeH^+, Mg, Mg^+, SO^+, N, N^+, NH^+, NH_2, NH_3
CN, CN^+, HCN, HCN^+, $HCNH^+$, N_2, N_2H^+, NS, NS^+ HNS^+, NO, NO^+
HNO, HNO^+, NO_2, H_2NO^+, N_2^+ OCN CH_3OH, HNC, HC_3N, C_2H_2, CH_3CN, C_2H_4
CH_2CO, C_2H_5, C_2H_3, $C_2H_5^+$, CH_3CCH C_2H_5OH, $C_2H_5OH_2^+$, $CH_3OH_2^+$
$H_5C_2O_2^+$, $HCOOCH_3$, C_2N, C_3N, C_2N^+ C_2NH^+, $C_2H_2^+$, C_4N^+, CH_3CNH, CH_3CNH^+
Si, SiO, SiH, Si^+, SiH^+, SiH_2, SiH_2^+, SiH_3, SiH_3^+ SiH_4, SiH_4^+, SiC, SiC^+
SiC_2, SiC_2^+, SiC_3, SiC_3^+ SiO^+, $SiOH^+$, SiS, SiS^+ $HSiS^+$
H_2SiO, SiH_5^+, Cl, Cl^+ HCl, HCl^+, H_2Cl^+, HNCO, HOC^+, C_4H
C_3H_2, MCH_3CNH, M, $HCOOCH_3$, MCO, MH_2O, MCO_2, MCH_4 MN_2, MHCN
MC_2H, MNH_3, MO_2, MCS, MSO, MH_2S, MHCS, MOCS, MSO_2, MNS, MH_2CS
MMg, MOCN, MH_2CN, MS_2 MHS_2, MO_2H, MNO_2, MHNO
MCH_3OH, MHNC, MHC_3N, MC_2H_2, MCH_3CN, MC_2H_5
MH_2CO, MC_2, MNO MCH_2CO, MC_2H_4, MC_2H_3, MCH_3CCH, MC_2H_5OH
MS, MSi, $MSiH_4$, MSiO, MSiC, $MSiC_2$, $MSiC_3$, MH_2SiO, MSiS MC_4H, MC_3H_2

To determine the properties of the gas in this type of environment, we first complete a detailed chemical modelling, and subsequently link the outputs of this with a molecular line radiative transfer model, as detailed in Benedettini et al. (2006). Since the majority of CS emission is likely to be from dense, star forming regions, we model the formation of CS through the collapse of diffuse molecular gas to a dense core. The chemical model we use is UCL_CHEM (Viti et al. 2004b). As discussed in more detail in Chapter 1, UCL_CHEM is a time and depth dependent gas-grain chemical model operating over two phases. The species included in the model are displayed in Table 3.1. Phase I simulates the collapse of initially atomic gas to a dense molecular cloud. During this phase, the temperature is a constant at 10 K. Freeze out of species onto grain surfaces occurs; the

model uses the chemical network from the UMIST database (Woodall et al. 2007) of which we use 211 species and 2303 gas and grain surface reactions. Phase II simulates the gas once it has reached a dynamical equilibrium, after the free fall collapse in Phase I. A burst of star formation is simulated, warming the cloud, increasing the temperature up to a maximum of 400 K. The species included in the model include all simple extragalactic molecules recorded so far, as well as many galactic species. Surface reactions are mainly based around hydrogenation, allowing saturated species to form. We run a large grid of models varying four parameters. These are, the temperature in phase II (T) in K, the UV radiation field (χ) as a multiple of the standard Milky Way ISM field (Habing 1968), the cosmic ray ionisation rate (ζ) as a multiple of the standard Milky way rate of 10^{-17} s^{-1} and the final gas density of the cloud in phase I ($n(H_2)$) in mol cm^{-3}. We vary each parameter over a wide range, given the lack of prior knowledge of the environment we are considering. Each model is ran over a period of up to 10^6 years. This is an approximate timescale for the cloud to collapse and sufficient chemistry to occur. By doing this we can see the effect on the chemistry and ultimately the formation of CS in different environments. In the models, all other parameters are taken as solar, scaled to the metallicity of the two galaxies where necessary. The grid of models we ran is summarised in Table 3.2.

Table 3.2: All permutations of these parameters were ran through UCL_CHEM

T (K)	χ (Habing)	ζ (1.3×10^{-17} s^{-1})	$n(H_2)$ (cm^{-3})
30	1	1	10^3
50	10	10	10^4
100	100	100	10^5
200	1000	1000	10^6
300	10000	10000	10^7
400	-	-	10^8

3.1.2 CS formation

In this section we analyse the outputs from UCL_CHEM in order to determine what factors influence CS chemistry. The dominant formation routes to CS are not completely understood. There was initially some agreement (Drdla et al. 1989; Lucas and Liszt 2002) that most CS formation in the gas phase is a product of the dissociative recombination reaction:

$$HCS^+ + e^- \longrightarrow CS + H, \tag{3.1}$$

What is less clear is the route to the formation of HCS^+. Drdla et al. (1989) found that the following gas-phase reaction scheme reproduced CS in abundances in the same range as their observations in relatively diffuse regions:

$$\begin{aligned} S^+ + CH &\longrightarrow CS^+ + H, \\ S^+ + C_2 &\longrightarrow CS^+ + C, \\ CS^+ + H_2 &\longrightarrow HCS^+ + H, \end{aligned} \tag{3.2}$$

However, Lucas and Liszt (2002) found that the abundances of S^+, C_2, and CH were an order of magnitude lower than observed if the mechanism above was producing the observed quantities of CS. Its high efficiency at low temperatures mean that reaction 3.1 is still likely to contribute to CS formation in certain environments. A general, more well agreed upon formation route (Destree et al. 2009; Nilsson et al. 2000; Lucas and Liszt 2002) is the substitution reaction:

$$SO + C \longrightarrow CS + O, \tag{3.3}$$

Chemical modelling (Bergin and Langer 1997) has shown that this reaction leads to a high abundance of CS quite swiftly, until formation of CO locks away much of the atomic carbon needed for reaction 3.3 . At later times, CS abundance drops as a result of efficient destruction of CS with atomic oxygen:

$$CS + O \longrightarrow CO + S, \tag{3.4}$$

Routes 3.3 and 3.4 are now believed to dominate the formation and destruction of CS (Lucas and Liszt 2002). Analysis of our chemical models tends to broadly agree with these findings. Both these reactions are neutral-neutral so should be highly dependent on

temperature. In Figure 3.1, we show selected models, all with a density of n(H_2) = 10^5 cm^{-3} with standard UV field and cosmic ray ionisation rate, only varying the temperature. We see that at the low temperatures of 30 K and 50 K, CS is not formed efficiently in early times and its abundance drops at later times. At 100 K, CS forms efficiently before dropping off slightly at late times as it reacts with atomic oxygen. At 300 K, CS formation is very efficient and we do not see any drop off in CS formation.

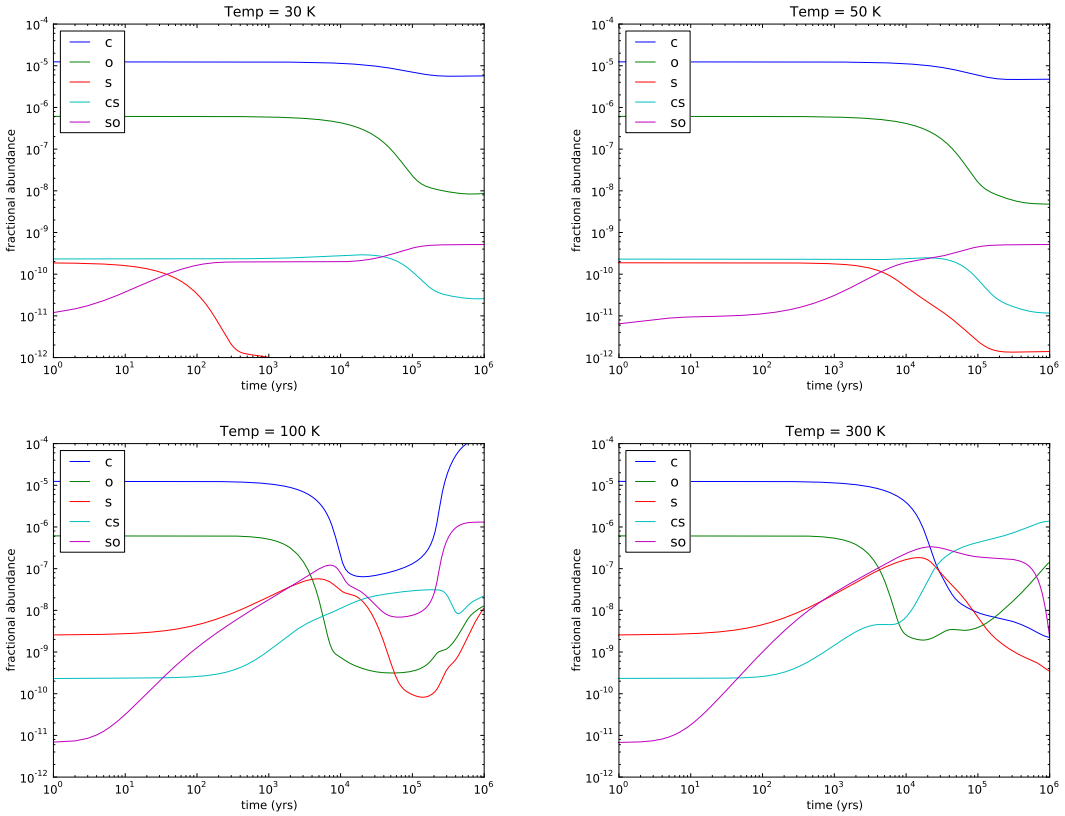

Figure 3.1: Chemical models with n(H_2) = 10^5 cm^{-3} with standard UV field and cosmic ray ionisation rate, and varying temperature. All the reactants from the dominant formation and destruction mechanisms shown in Reactions 3.3 and 3.4 are shown.

While temperature is clearly very important in determining CS abundance, we find that is not the only factor. Firstly, we find that at n(H_2) <10^4 cm^{-3}, CS formation is considerably less efficient, even at high temperatures. Figure 3.2 shows the same model as in Figure 3.1 for 300 K but at a density, n(H_2) = 10^3 cm^{-3}. We see that CS is not formed nearly as efficiently as at higher density.

We also find the cosmic ray ionisation rate is an important parameter in determining the dominant mechanisms. A high cosmic ray ionisation rate, leads to the destruction

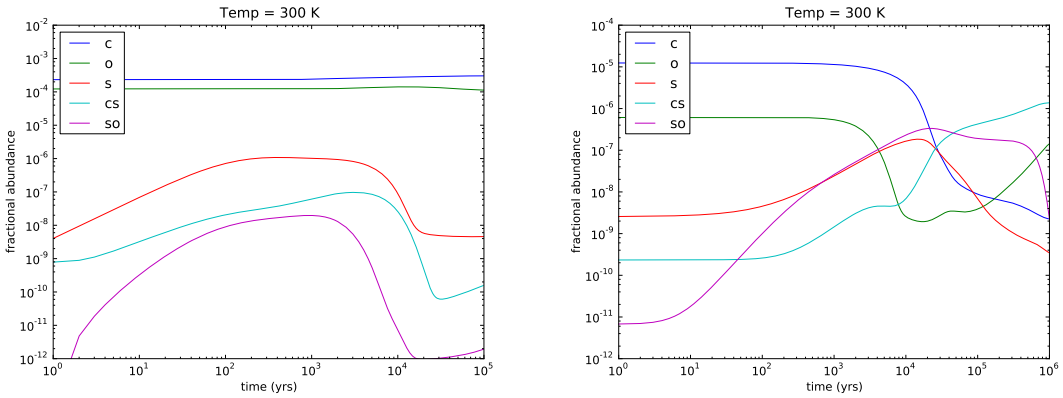

Figure 3.2: *Left*: Chemical model with n(H_2) = 10^3 cm^{-3} with standard UV field and cosmic ray ionisation rate, at T = 300 K. *Right*: The same model but at n(H_2) = 10^5 cm^{-3}

of a small percentage of available CO, providing enough atomic carbon to allow reaction 3.3 to counteract the destruction from reaction 3.4. However, this is also more efficient as there is more atomic oxygen available from CO. Figure 3.3 is the same at the 100 K model in Figure 3.1 but with an increased comic ray ionisation rate of $10\zeta_0$, where ζ_0 is the standard ISM cosmic ray ionisation rate = 10^{-17} s^{-1}. We see just over half an order of magnitude increase in CS abundance on the $1\zeta_0$ model. Studying these two models, we find that at $1\zeta_0$, a significant source of CS destruction is from Reaction 3.5. Both the formation and destruction processes are near two orders of magnitude slower when ζ is lowered from 10 ζ_0 to 1 ζ_0.

$$H_3O^+ + CS \longrightarrow HCS^+ + H_2O, \tag{3.5}$$

3.1.3 Radiative transfer modelling

The chemical abundances of CS given by UCL_CHEM are input to the radiative transfer model SMMOL (Rawlings and Yates 2001). This is an accelerated Λ-iteration (ALI) code for solving multi-level radiative transfer problems. Data on the CS molecule - including energy levels, transition frequencies, Einstein A coefficients and collisional rates - are taken from the LAMDA database (Schöier et al. 2005). The code is discussed in Chapter 1 and its ability to predict a line profile allows us to compare with our observations, giving us a single model that best fits the chemical history and physical conditions of the environment

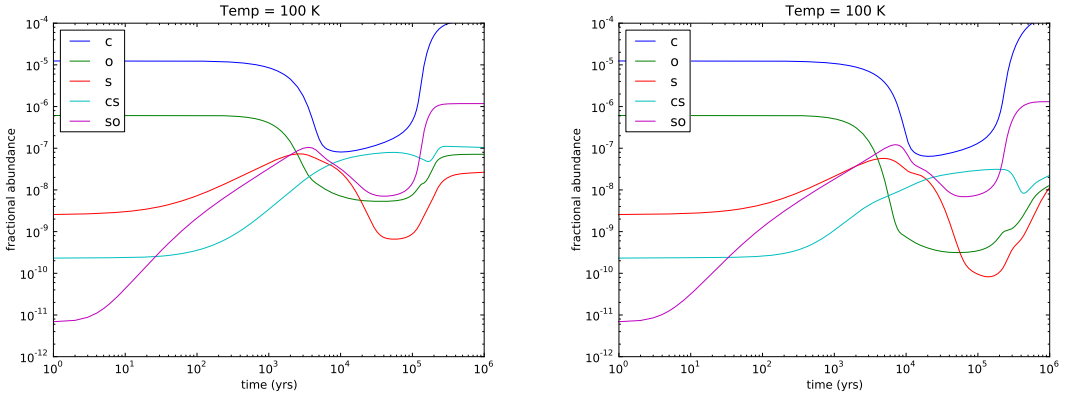

Figure 3.3: *Left*: Chemical model with $n(H_2) = 10^5$ cm^{-3} with standard UV field and cosmic ray ionisation rate of $10\zeta_0$, at T = 100 K. *Right*: The same model but with a cosmic ray ionisation rate of $1\zeta_0$

observed. Both SMMOL and UCL_CHEM are modelling the formation of one dense core. In our beam, there must be many dense cores. At most, the beam covers an area ≈2 kpc (CS(2 − 1) in NGC 3079) and the typical scale of dense cores is 0.05 pc (Shimajiri et al. 2015). It is extremely unlikely CS emission is emanating only from one dense core. If it was, we would not see it as the signal would be too diluted in the beam. It is more likely that the emission is coming from a number of these dense core regions. To account for this, we estimate the number of cores in our beam and scale up the emergent flux by this factor. Our estimate is based on a study by Lintott et al. (2005). They estimate that there are 10^4 hot dense cores in the Milky Way, and calculate a scale factor for other galaxies based on their star formation rate. We adopt the same methodology, based on the star formation rates of our observed galaxies (see Table 2.1) and the likely central location of the gas. Our targets are both starburst galaxies which see a greater rate of star formation than the Milky Way, concentrated over the nuclear bulge of both galaxies (Tsai et al. 2013; Yamagishi et al. 2010; Schinnerer et al. 2006). As these calculations are only estimates, we scale up by orders of magnitude, and by the same values for both galaxies, although we acknowledge that the regions observed in NGC 3079 are larger than in NGC 6946. We use scale factors of 1, 10, and 100; leading to our estimates for the number of dense cores to be 10^4, 10^5, and 10^6. We note that we take the arbitrary end point of the chemical model (10^6 years) to input into SMMOL. While we do not claim this to be the age of our cores, we use it as a representative chemical age of the molecular gas at large scales. In fact, time dependent effects may be important in energetic extragalactic environments

and have been discussed elsewhere (Meijerink et al. 2013; Bayet et al. 2008b).

Analysis of the models is completed using a χ^2 method. We use the equation

$$\chi^2 = \frac{1}{N}\sum_{i=1}^{N}\left[\frac{F_{\rm mod}(i) - F_{\rm obs}(i)}{F_{\rm obs}(i)}\right]^2, \tag{3.6}$$

Where N is the number of lines used, $F_{\rm mod}$ is the integrated flux of the modelled line, and $F_{\rm obs}$ is the integrated flux of the observed line. This formula has been used in previous works in a similar way (e.g. Benedettini et al. 2006, Doty et al. 2004). We use the difference between the model flux and the observed flux instead of the measurement error because the errors associated with the modelling are greater than those in the observations. This also has the advantage of avoiding giving brighter lines a higher weight. It is possible to use SMMOL to model line profiles of CH_3OH and H_2CO. Since neither of these molecules were detected outside of the centre of either galaxy, it was not possible in this study.

Table 3.3: Best fit parameters for each location in each galaxy (10^6 cores). NA indicates that the model was insensitive to variation in the parameter; an equally good fit is produced whatever its value

Galaxy	$\Delta\alpha$	$\Delta\delta$	T (K)	χ (Habing)	ζ ($\zeta_0 = 1.7 \times 10^{-17}$ s^{-1})	n (cm^{-3})	χ^2	Notes
NGC 6946	0	0	100	NA	100	10^6	0.20	
NGC 6946	0	-10	100	NA	1	10^5	0.032	
NGC 6946	0	+10	100	NA	1	10^5	0.046	
NGC 6946	+10	0	100	NA	1	10^5	0.021	
NGC 6946	-10	0	100	NA	1	10^5	0.13	
NGC 6946	-20	0	100	NA	10	10^7	0.55	poor fit
NGC 6946	+20	0	300	NA	100	10^7	0.06	$(2-1)$ only
NGC 6946	+10	+10	100	NA	10	10^7	1.1	poor fit
NGC 6946	+10	-10						no fit
NGC 6946	0	-20	400	NA	1000	10^7	0.02	$(2-1)$ only
NGC 6946	0	+20	100	NA	10	10^7	0.80	poor fit
NGC 3079	0	0	400	NA	10	10^6	0.088	
NGC 3079	+10	0	400	NA	10	10^6	0.009	$(2-1)$ only
NGC 3079	0	+10	400	NA	10	10^6	0.08	$(2-1)$ only

Table 3.4: Best fit parameters for each location in each galaxy (10^5 cores). NA indicates that the model was insensitive to variation in the parameter; an equally good fit is produced whatever its value

Galaxy	$\Delta\alpha$	$\Delta\delta$	T (K)	χ (Habing)	ζ ($\zeta_0 = 1.7 \times 10^{-17}$ s^{-1})	n (cm^{-3})	χ^2	Notes
NGC 6946	0	0	400	NA	10	10^6	0.30	
NGC 6946	0	-10	200	NA	1	10^6	0.24	
NGC 6946	0	+10	100	NA	10	10^5	0.25	
NGC 6946	+10	0	400	NA	10	10^6	0.22	
NGC 6946	-10	0	100	NA	10	10^5	0.24	
NGC 6946	-20	0	100	NA	10	10^5	0.21	
NGC 6946	+20	0	400	NA	10	10^6	0.0001	$(2-1)$ only
NGC 6946	+10	+10	100	NA	10	10^5	0.31	
NGC 6946	+10	-10						no fit
NGC 6946	0	-20	400	NA	10	10^6	0.01	$(2-1)$ only
NGC 6946	0	+20	400	NA	100	10^5	0.02	$(2-1)$ only
NGC 3079	0	0	400	NA	1	10^5	0.37	
NGC 3079	+10	0	400	NA	1	10^5	0.02	$(2-1)$ only
NGC 3079	0	+10	400	NA	1	10^5	0.05	$(2-1)$ only

3.2 Discussion

We now analyse the results of our models. It is important to note that while the observations cover a large area, CS emission is predominantly emanating from smaller regions of dense, star forming gas. We assume that there are many of these regions in our beam, based on the work by Levine et al. (2008). Since we complete this study under the assumption of either 10^4, 10^5 or 10^6 dense cores in the beam, we discuss each set of models separately. The model line profiles that we analyse can be found in Appendix A, Figures A.1 to A.4. Firstly, under the assumption of 10^6 cores in the beam, the best fit models for all positions in NGC 3079 are the same (Table 3.3). Temperature and density are quite high - 400 K and 10^6 cm^{-3}, respectively - with a cosmic ray ionisation rate of 100 times the standard rate (ζ_0). The high temperature is likely to be somewhat higher than the average temperature across the region we are observing. The high temperature is possibly an indication of the presence of shocks, which we discuss later.

Models for NGC 6946 follow the general pattern of decreasing density (10^6 cm^{-3} $\rightarrow$ 10^5 cm^{-3}) moving away from the centre of the galaxy (when only including models with good fits to both lines). Temperature is fairly constant at 100 K. Models for the outer regions of our observations generally do not provide good fits, or there is not enough data to fit to although the lowest χ^2s are all for high density (10^7 cm^{-3}) models. We include these results for completeness, but note that - given the high χ^2 values - there are large degeneracies in these models. There are no models with a density $<10^5$ cm^{-3} that provide a good fit to the data (i.e. with χ^2 <1). We note that in other works of the study of the molecular gas in NGC 6946 (Mangum et al. 2013; Pan et al. 2015), the temperature was found to be considerably lower (T <50 K) than we find. This, however, is not in contradiction to the work presented here as previous studies of this galaxy have focused on using tracers of the more extended molecular gas clouds. Taking results from this and previous work, a pattern of giant molecular clouds (GMCs) with dense cores within them can be assumed, as is found in Galactic GMCs such as Orion A (Shimajiri et al. 2015). The models indicate an increased cosmic ray ionisation rate in the centre of NGC 6946. For this to occur, there must be an enhanced source of cosmic rays. The predominant source is likely to be supernovae. NGC 6946 has nine observed supernovae over the last century. This is the highest number of recorded supernovae in any galaxy. This rate compares to that of the Milky Way of two per century (Diehl et al. 2006). It is therefore

possible that NGC 6946 would have an enhanced cosmic ray ionisation rate, although 100 times the Milky Way value may be an overestimate.

When considering 10^5 cores in the beam, the best fit models for each position (see Table 3.4) in NGC 3079 arise from a different set of parameters from the previous set of models, although again there is no variation across position. Again from a high temperature model, the density and cosmic ray ionisation rate are lower than for the 10^6 core simulation but do not provide the same quality fit as shown in Table 3.3. In contrast with the results for NGC 6946 in Table 3.3, the 10^5 cores models show a higher temperature and higher density for some best fit models, although as with NGC 3079, these do not fit as well as the 10^6 core models. All our model results, no matter how many cores in the beam are assumed, show an insensitivity to UV radiation field. This is due to the high extinction in the UV associated with the high density regions where CS emission originates. We note that this does not imply there is a lack of UV radiation but simply that UV is unable to penetrate down to dense cores. We find that we cannot successfully fit the observations using 10^4 cores for any region of either galaxy because the antenna temperature of the theoretical lines is too low to match observations. In many cases, the profiles do not match either. This possibly provides a lower limit on the number of star forming cores we see within our beam.

3.2.1 Total dense gas mass

Since we have estimated the number of dense cores required to replicate our observations, it is possible to calculate a very simple estimate for the total mass of dense gas, as traced by CS, in the observed region. More specifically, we are calculating the mass of gas in our dense cores. This is completed here for the central pointing of NGC 6946. We know the size of our dense cores so we can therefore work out the volume of one dense core as $4/3\ \pi\ \times\ (0.025\ \times\ 3.086 \times 10^{16})^3 = 1.9 \times 10^{45}$ m^3. For our best fit model in the central region the molecular hydrogen density is 10^6 cm^{-3}. The mass of a hydrogen molecule is 3.27×10^{-27} kg. Assuming solar metallicity, for this rough calculation, this is scaled up by a factor of 1.41 taking the mean mass of a molecule in the cloud to 4.62×10^{-27} kg. At a density of 10^6 cm^{-3}, or 10^{12} m^{-3}, the total mass of one dense core is $1.9 \times 10^{45}\ \times$ $4.62 \times 10^{-27}\ \times\ 10^{12} = 8.7 \times 10^{30}$ kg. Depending on whether we have 10^5 or 10^6 dense cores, this gives us a mass of $\sim 5 \times 10^5\ M_\odot$or $5 \times 10^6\ M_\odot$. Crosthwaite and Turner (2007) find that the total molecular gas mass for the galaxy is $3 \times 10^9\ M_\odot$. Furthermore, Israel

and Baas (2001) calculate that the molecular gas mass within the central 0.5 kpc of the galaxy is $\sim 2 \times 10^7$ $M_\odot$. These values are consistent with our estimate, since we are not including a large proportion of the molecular gas and are only interested in the dense gas. The central region observed in Israel and Baas (2001) is very similar in size to our own. Given this, we calculate that the dense gas mass ($n(H_2) \approx 10^6$ cm^{-3}) as a fraction of molecular gas mass is 0.025 - 0.25.

Battisti and Heyer (2014) find that the mean dense gas fraction of milky way GMCs is $0.07^{+0.13}_{-0.05}$. The technique used for this utilised overdensities of dust, and assumed that this correlated with gas density. They state that their cutoff point is dust emission correlating with a gas density of 10^4 cm^{-3}. Since we are observing CS lines that trace gas only slightly denser than this, we take this as a reasonable comparison. However, Solomon et al. (1992) find that the dense gas mass ratio for starbursts is higher than that of regular galaxies. Using the ratio of total HCN luminosity to total CO luminosity, they find values of 0.07-0.3 for several starbursts. This indicates that both our estimates are reasonable, but 10^6 may be more accurate.

3.2.2 Shocks

All the discussion above assumes there are no shocks. However, CS has recently been shown to be enhanced in shocked regions (e.g. Nicholas et al. 2012). This is also indicated by the high temperature models which successfully fit many of the emission regions. Shock temperatures are unlikely to be sustained for the timescale of our models but could be very significant for CS chemistry even over a shorter timescale. As discussed in Chapter 1, UCL_CHEM is capable of simulating shocks. Here we model a simplified shock, by introducing a short-lived increase in temperature (Viti et al. 2001). We ran shock models for the central position of both galaxies. These were completed with the same best fit parameters as in the 10^6 core models, as these give the lowest χ^2 values. During the shocked period, the temperature rises from 100 K to 500 K, and then reduces back to 100 K. This would be the temperature experienced during a relatively weak shock of v $\sim$ 15 km s^{-1} (Jiménez-Serra et al. 2008). During this period, anything remaining on grain surfaces is sublimated. In our radiative transfer code we then vary the number of cores as before. We see that the best fits to the line intensities of CS$(2-1)$ and CS$(3-2)$ now come from the model assuming that there are 10^4 dense cores within the beam (see Figures 3.4 and 3.5). The total dense gas mass would therefore only be $\sim 5 \times 10^4$ $M_\odot$, just 0.25% of

the total molecular gas mass. This suggests that since shocks have a significant effect on CS emission, it is necessary to know whether the region being observed is (or has been) shocked, in order to fully characterise the environment observed. Therefore, observations of shock tracers (such as SiO), would be very useful in conjunction with CS detections.

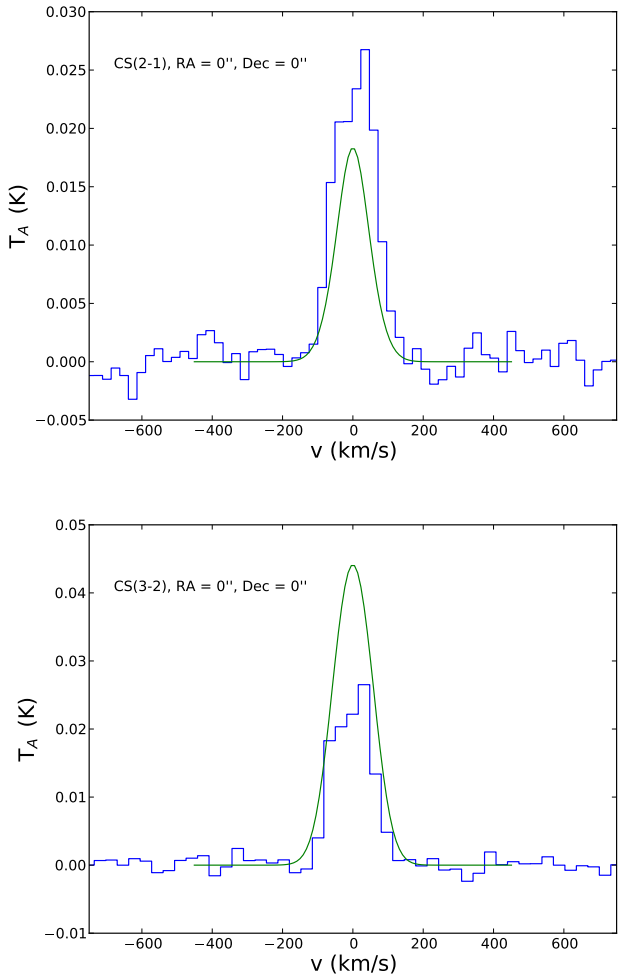

Figure 3.4: Shock model fits for NGC 6946

Examining the chemical models, during shock treatment the following formation reaction also becomes important:

$$C_2 + S \longrightarrow CS + C. \tag{3.7}$$

Reaction 3.7 is important during the shock as it both becomes more efficient at high temperatures and the abundance of the reactant species increases. This points to there not

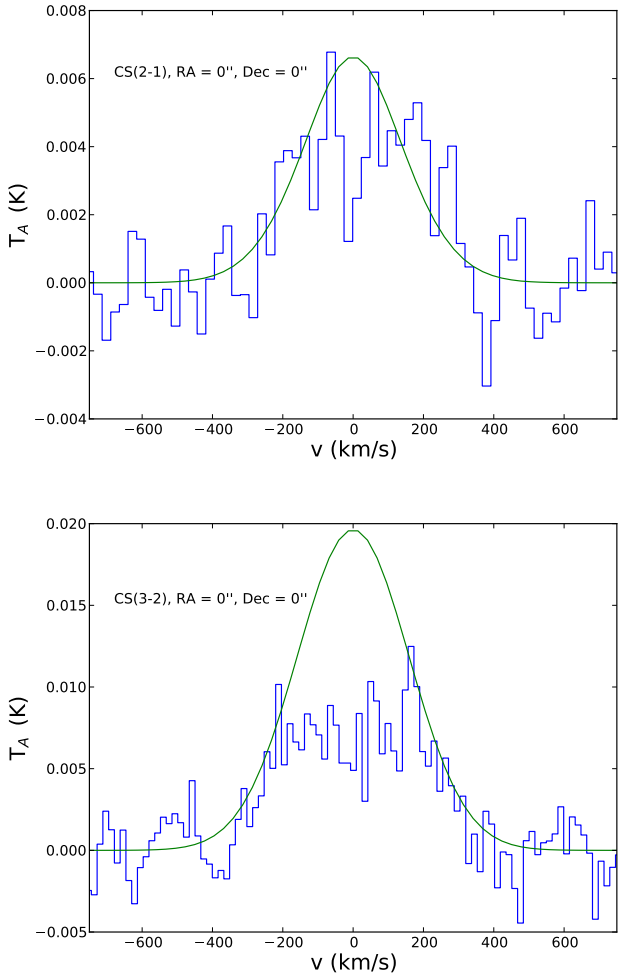

Figure 3.5: Shock model fits for NGC 3079

being one overwhelmingly dominant way of forming CS. Different reactions are responsible for its formation (and destruction) in different conditions. Based on the UMIST database (McElroy et al. 2013), there are 48 formation routes to CS and 17 destruction reactions. We have shown in this work that some of them are very dominant in certain conditions, while others play little or no role in producing or destroying CS. We also show that this can vary strongly with environment and that mechanisms that maybe dominant in certain conditions, are less so when those conditions alter even in quite a small way.

3.3 Conclusions

In Chapter 2, we mapped CS emission across two nearby starburst galaxies - NGC 3079 and NGC 6946. To further the LTE analysis in Chapter 2 and determine conditions

in the dense gas environments being traced by CS, a time dependent gas-grain chemical model (UCL_CHEM) was linked to a radiative transfer code (SMMOL) to simulate the line emission. Comparing the observations to the models led to the conclusion that the amount of dense ($>10^5$ cm^{-3}) gas needed to replicate our models was $\sim 5 \times 10^5$ $M_\odot$or 5×10^6 $M_\odot$in both galaxies. This is under the assumption that emission is coming from between 10^5 and 10^6 dense cores of $\sim$ 0.05 pc. Comparing to results of previous works, this amounts to a dense to molecular gas fraction of 0.025 to 0.25.

Many regions in our galaxies are found to have high temperatures (up to T = 400 K). We inferred from this that we may be observing shocked gas, as these would raise the temperature of the observed regions. We were able to adapt our models to account for the presence of shocks. We find that in order to match the observations, there may be up to an order of magnitude less dense gas if it is in the process of being (or previously has been) shocked. This is largely due to the increased efficiency of CS formations routes under high temperatures. If shocks are present, the required dense gas mass fraction reduces to just 0.25%.

The routes to the formation of CS are important factors in successfully modelling regions of dense gas. With ever more complex chemical webs, predicted abundances of molecules become highly sensitive to set conditions. We find that shocks provide conditions that are effective in efficiently forming CS in necessary abundances due in part to increased efficiency of Reaction 3.7. A high cosmic ray ionisation rate ($\approx$100 ζ_0) could also have a significant influence on CS chemistry by increasing the rate of Reaction 3.3. In conclusion, CS observations, combined with chemical and radiative transfer modelling are capable of disentangling dense star forming regions from surrounding molecular gas. With better spatial resolution it should be possible to quantify further the chemical differentiation across the central regions of starburst galaxies.

Chapter 4

Molecular shock tracers in NGC 1068: SiO and HNCO

The work presented in this chapter is based on a paper by Kelly et al. (2016), in collaboration with S. Viti, S. García-Burillo, A. Fuente, A. Usero, M. Krips, and R. Neri

Molecular emission is now routinely used to probe and trace the physical and chemical processes in external galaxies. Over the past 20 years or so, different molecules have been found to trace different gas components within a galaxy (for example HCO, HOC^+ in PDRs (e.g. Savage and Ziurys 2004; García-Burillo et al. 2002, HCN and CS for dense gas (e.g. Gao and Solomon 2004; Bayet et al. 2008a)). However, it is seldom possible to identify one molecular species with one gas component only, as often energetics play a key role in shaping the spectral energy distribution of the molecular ladders. Of particular interest to this study are the molecules SiO and HNCO, which are both well known tracers of shocks (Martín-Pintado et al. 1997; Rodríguez-Fernández et al. 2010). Both these molecules have been observed and used as shock tracers in external galaxies (Meier and Turner 2005; Usero et al. 2006; Martín et al. 2009a; García-Burillo et al. 2010).

As discussed in Chapter 1, HNCO may be formed mainly on dust grain mantles (Fedoseev et al. 2015) or possibly in the gas phase, followed by freeze out to the icy mantles (López-Sepulcre et al. 2015). In either case its location on the outer regions of the dust grain means that it is easily sublimated even in weakly shocked regions; hence HNCO

may be a particularly good tracer of low velocity shocks. Silicon, on the other hand, is partially depleted from the gas to make up the dust grain itself. This extra silicon is only released into the gas phase in higher velocity shocked regions through sputtering. Once it is in the gas phase, it can react with molecular oxygen or a hydroxyl radical to form SiO (Schilke et al. 1997), which can then be used to trace more heavily shocked regions. Thus HNCO and SiO concomitant detection in a galaxy where shocks are believed to take place may be able to give us a fuller picture of the shock history of the gas. This would be of particular interest in a galaxy where an outflow may be interacting with gas in the ISM. For this reason, we observe NGC 1068.

NGC 1068 is a well-studied nearby (D = 14 Mpc (Bland-Hawthorn et al. 1997), $1'' \approx 78$ pc) Seyfert 2 galaxy. Its molecular gas is distributed over three regions (Schinnerer et al. 2000): a starburst ring with a radius ∼1.5 kpc, a ∼2 kpc stellar bar running north East from a circumnuclear disk (CND) of radius ∼200 pc. García-Burillo et al. (2010) use the PdBI to map the galaxy and found strong detections of SiO$(2-1)$ in the East and West of the CND. The SiO kinematics of the CND point to an overall rotating structure, distorted by non-circular and/or non-coplanar motions. The authors conclude that this could be due to large scale shocks through cloud-cloud collisions, or through a jet-ISM interaction. However, due to strong detections of CN not easily explained by shocks, they also suggest that the CND could be one large X-ray dominated region (XDR). More recently, the CND has been mapped at very high resolution with ALMA in several molecular transitions (García-Burillo et al. 2014; Nakajima et al. 2015; Garcia-Burillo et al. 2016). In Garcia-Burillo et al. (2014), five chemically distinct regions were found to be present within the CND: the AGN, the East Knot, West Knot and regions to the north and south of the AGN (CND-N and CND-S). Viti et al. (2014) combined these ALMA data with PdBI data and determined the physical and chemical properties of each region using a combination of CO rotation diagrams, LVG models and chemical modelling. It was found that a pronounced chemical differentiation is present across the CND and that each sub-region could be characterised by a three-phase component interstellar medium: one of these components comprises shocked gas and seems to be traced by the high J, 7-6, CS line.

We now resolve the CND in both SiO$(3-2)$ and HNCO$(6-5)$ and couple these with previous lower-J observations. In Section 4.1, we describe the observations, while in Section 4.2 we present the molecular maps. In Section 4.3 we present the spectra at each location. In Section 4.4 we perform an LTE and RADEX analysis in order to constrain

the physical conditions of the gas, as well as chemical modelling to determine its origin. We briefly summarise our findings in Section 4.5.

4.1 Observations

Observations of NGC 1068 were carried out with the PdBI array (Guilloteau et al. 1992) between January 23 and March 5, 2010. The AB configurations and six antennae were used. We simultaneously observed the (v=0, J=3–2) line of SiO (at 130.2686 GHz) and the J=6–5 band of HNCO (at 131.4–132.4 GHz). The HNCO(6–5) band is split up into many hyperfine lines blended around five groups (($K_{\rm p}, K_{\rm o}$)=$(1,6)-(1,5), (2,5)-(2,4), (2,4)-(2,3), (0,6)-(0,5)$, and $(1,5)-(1,4)$). The strongest group of lines, (($K_{\rm p}, K_{\rm o}$)=$(0,6)-(0,5)$), lies at 131.8857 GHz. During the observations the spectral correlator was centred at the mock rest frequency 131.0765 GHz. This choice allowed us to cover simultaneously the SiO and HNCO lines. Rest frequencies were corrected for the recession velocity initially assumed to be $v_o(HEL)$=1137 km s^{-1}. The correlator configuration covers a bandwidth of 1 GHz for this setup, using eight 320 MHz-wide units with an overlap of 90 MHz; this is equivalent to 2290 km s^{-1} at 131.0765 GHz. Observations were conducted in single pointing mode of size 38.8″ centred at α_{2000}=$02^h42^m40.71^s$ and δ_{2000}=–00°00′47.94″. The latter corresponds to the nominal position of the AGN core, as determined from different VLA and VLBI radio continuum images of the galaxy (e.g. Gallimore et al. 1996). Visibilities were obtained through on-source integration times of 20 minutes framed by short ($\sim$2 min) phase and amplitude calibrations on nearby quasars. The absolute flux scale in our maps was derived to a 10% accuracy based on the observations of primary calibrators whose fluxes were determined from a combined set of measurements obtained at the 30m telescope and the PdBI array.

The image reconstruction was done with the standard IRAM/GILDAS software (Guilloteau and Lucas 2000). We used natural weighting and no taper to generate the SiO and HNCO line maps with a size of 133″ and 0.13″/pixel sampling; the corresponding synthesised beam is 1.1″ × 0.7″ ($\sim$ 86 pc ×55 pc, PA=23°. The conversion factor between Jy beam^{-1} and K is 90 K Jy^{-1} beam. The point source sensitivities were derived from emission-free channels. They are 1.2 mJy beam^{-1} in 5 MHz-wide channels. Images of the continuum emission of the galaxy, not shown in this Chapter, were obtained by averaging those channels free of line emission at both frequency ranges.

We have also used the SiO(v=0, J=2–1) PdBI map of García-Burillo et al. (2010) to derive the 3–2/2–1 line ratio map in T_{mb} units at the common (lower) spatial resolution of $3.6'' \times 2.1''$, PA=29° of the 2–1 line map. This required the use of a Gaussian kernel of $3.4'' \times 1.9''$, PA=29° to convolve the SiO(3–2) map. Hereafter, velocities are referred to $v_o(HEL)$=1137 km s^{-1}.

Table 4.1: Locations of peak emission for each line, with offset from CO(3 − 2) emission

Line	Position	RA	Dec	ΔRA, ΔDec (″)	Location
SiO(3 − 2)	East Knot	02:42:40.771	-00:00:47.98	0, 0.1	East Knot 1
HNCO(6 − 5)	East Knot	02:42:40.763	-00:00:48.60	-0.1, -0.8	East Knot 2
CO(3 − 2)	East Knot	02:42:40.771	-00:00:47.84	0, 0	-
SiO(3 − 2)	West Knot	02:42:40.608	-00:00:48.43	-0.3, -0.6	West Knot 1
HNCO(6 − 5)	West Knot	02:42:40.590	-00:00:48.77	-0.6, -0.48	West Knot 2
CO(3 − 2)	West Knot	02:42:40.630	-00:00:47.84	0, 0	-

4.2 Molecular gas maps

4.2.1 SiO

Figure 4.1 shows the SiO(3 − 2) intensity map over the central $6'' \times 6''$ region. Data are included across a 500 km s^{-1} spectral window centred around the SiO transition. We see strong emission to the East of the AGN, with weaker detections to the south and West. In agreement with SiO(2 − 1) (García-Burillo et al. 2010), little emission is seen around the AGN itself. Table 4.1 shows the coordinates of the peak emission of SiO(3 − 2) to both the East and West of the AGN. This is compared to those in Viti et al. (2014) from CO(3 − 2), which is used to identify an East Knot and a West Knot. This notation is continued for the rest of this Thesis.

We see that the peak SiO(3 − 2) emission matches well with the molecular gas traced by CO(3 − 2) in the East Knot (see Table 4.1) but it is slightly offset in the West Knot. It should be noted that since emission here is weak and extended and the beam size is 1″, this offset may not be meaningful. We do not see any noticeable emission outside of the circum-nuclear region about the AGN. The starburst ring is not detected in the SiO(3−2).

We also present SiO maps for varying velocities (Figure 4.2). These are split into 100 km s^{-1} bands, centred around v - v_o = 0 km s^{-1}. Examining these plots, it is clear that the majority of SiO emission in the East Knot is coming from the central 100 km s^{-1},

with minor contributions from >50 km s^{-1} and <-50 km s^{-1}. However, in the West Knot, although the line is much weaker, the majority of SiO emission is from velocities >50 km s^{-1}. This is further analysed in section 4.3.

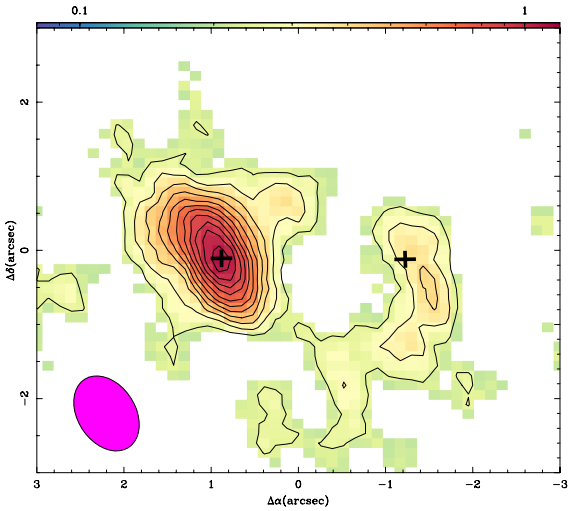

Figure 4.1: SiO(3 − 2) map. Contours are from 3σ in increments of 1σ where σ ∼0.08 Jykm/s/beam. The black crosses indicate the approximate position of the CO(3 − 2) peak. The beam size is displayed in the bottom left.

4.2.2 HNCO

Figure 4.3 shows the HNCO(6 − 5) map over the same region as the SiO(3 − 2) map, and integrated across the same spectral window. The strongest emission is seen in the West Knot, but is also clear in the East Knot. There is little to the north or south of the AGN. Nothing is seen around the AGN itself. When compared to both the SiO and CO peaks, it is clear that the HNCO emission is offset in both regions. It is significantly south (∼1″) and slightly West of the other peaks. We show this in Figure 4.4, where we overlap the two sets of data.

Although we do not split HNCO(6 − 5) emission into bands, due to its weaker emission compared to that SiO(3 − 2), we analyse HNCO spectra in section 4.3.

4.3 Spectral analysis

We extract spectra from four regions of the CND. These are the peaks in the East Knot and West Knot of SiO and HNCO. We extract a spectrum from both species in these regions,

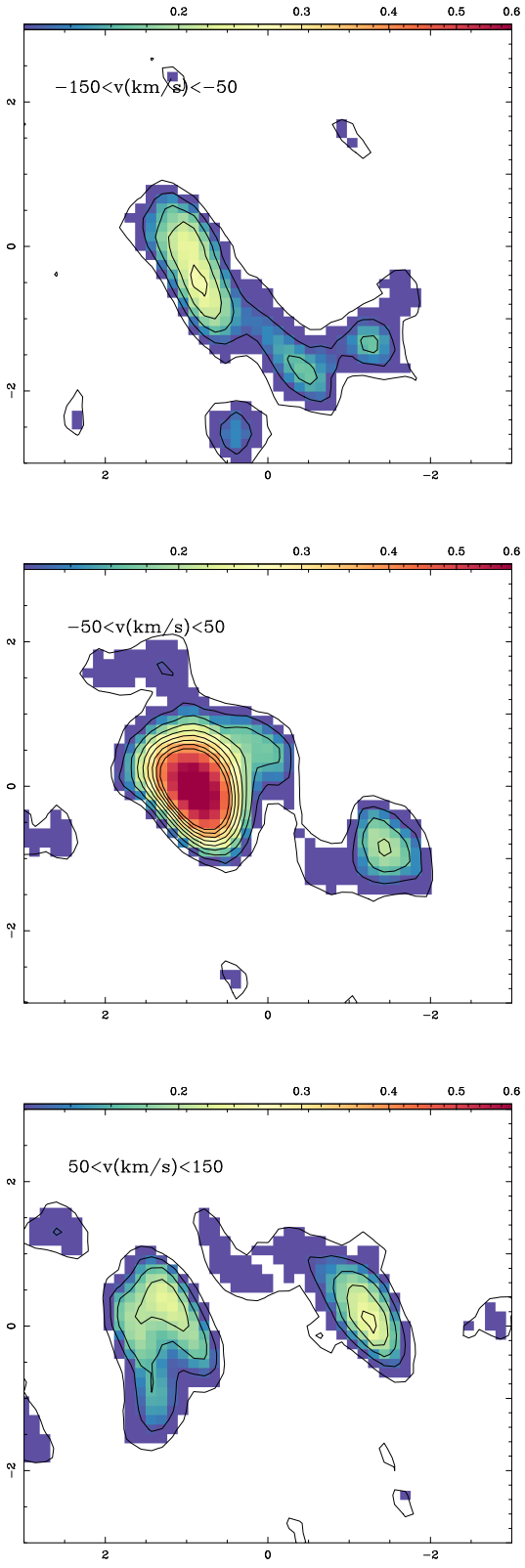

Figure 4.2: SiO(3 − 2) maps for velocity widths of 100 km/s. Contours are from 3σ in increments of 1σ where σ ∼0.04 Jykm/s/beam

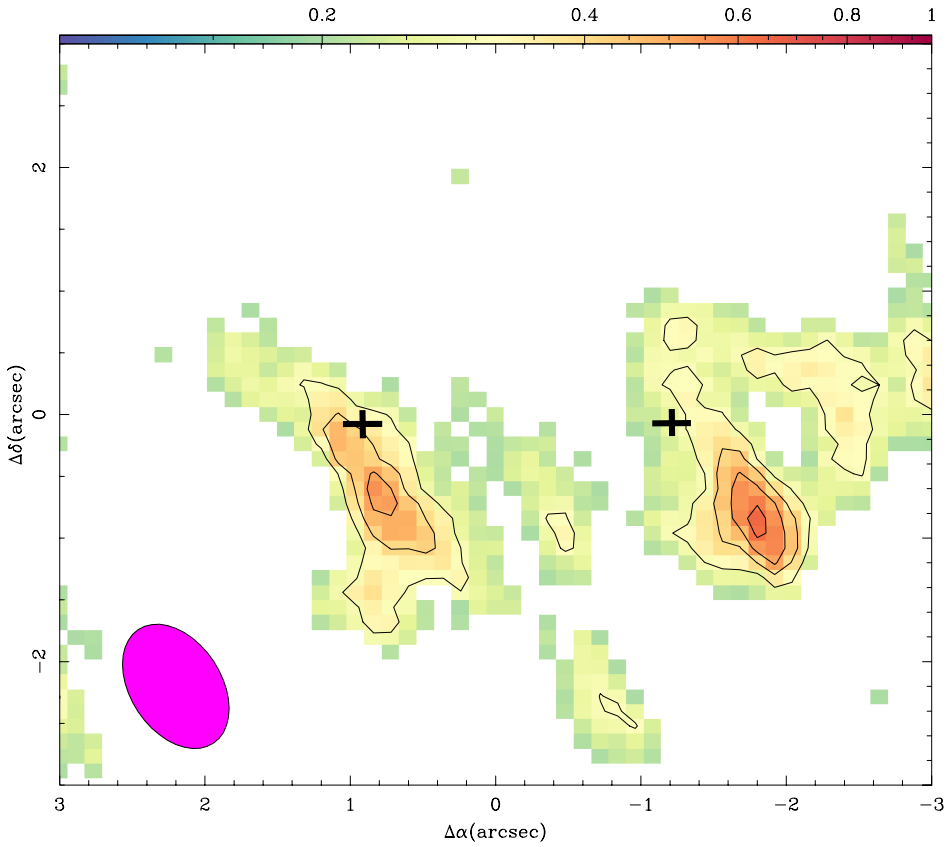

Figure 4.3: HNCO($6-5$) map. Contours are from 3σ in increments of 1σ where σ ∼0.1 Jykm/s/beam. The black crosses indicate the approximate position of the CO($3-2$) peak. The beam size is displayed in the bottom left.

giving us eight spectra in total. We also overlay the CO($2-1$) line (its peak scaled to the HNCO($6-5$) peak), from PdBI observations, degraded to the same resolution as the SiO($3-2$) line. We do this to confirm that the HNCO($6-5$) emission we see, in particular in West Knot 2, is real. In this location, although the profiles are different, we see contiguous emission from 200 km s^{-1} down to -200 km s^{-1} in CO($2-1$). The wings of the CO($2-1$) line are at detection confidence level of 4σ. We also see a clear detection of CO($3-2$), which is not shown so as not to confuse the figure, at high velocities in West Knot 2, from ALMA observations. This is not to suggest that CO is tracing shocked gas: in fact CO is present in the shocked region as well as in the other components of the molecular gas. We use CO only as a guide to see the allowed velocities for SiO and HNCO. As further reassurance our detection of HNCO in the West Knot is real, there are no other detectable transitions of other species near the HNCO($6-5$) band frequency.

The four locations are displayed in Figure 4.4 and Figure 4.5 . We see in East Knot

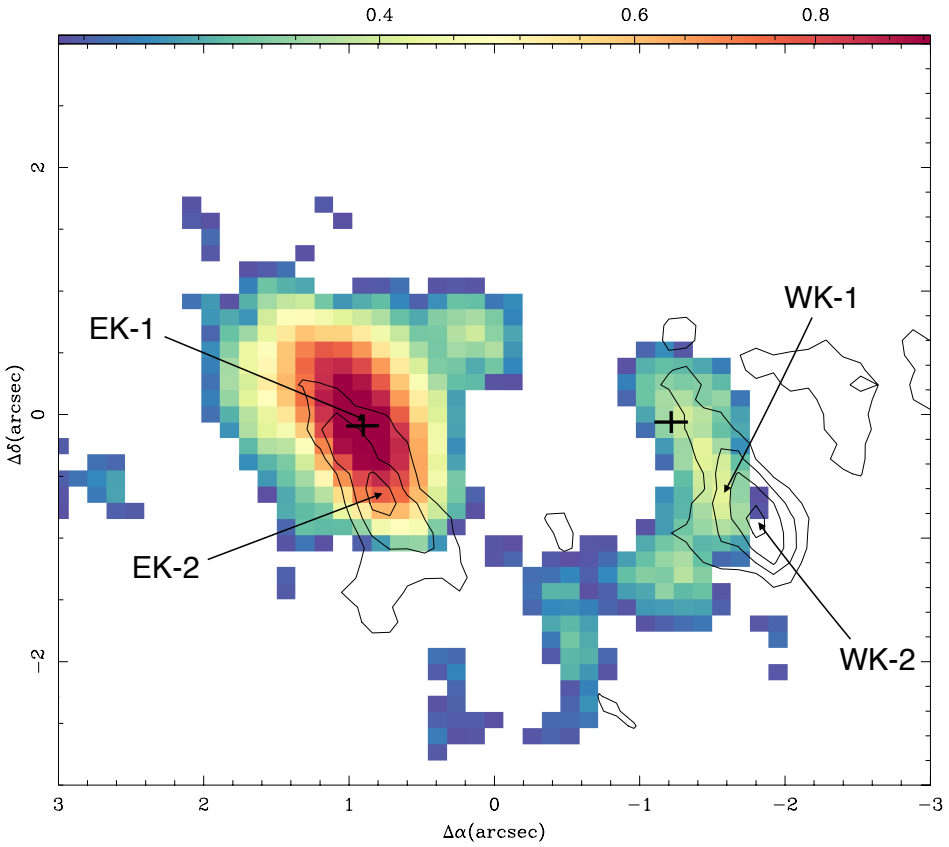

Figure 4.4: Overlap of SiO (colours) and HNCO (contours). The locations identified for further analysis are labelled. Contours are from 3σ in increments of 1σ where σ ~0.1 Jykm/s/beam. The black crosses indicate the approximate position of the CO(3 − 2) peak.

1, the point of peak SiO emission in the East Knot, a strong SiO line centred around -12 ± 4 km s^{-1}, compared to v_{sys}, where there is also evidence of a double peak. In the same location, HNCO displays a similar feature, but is much weaker. It is centred around -6 ± 15 km s^{-1}, compared to v_{sys}. Moving to East Knot 2, the Eastern peak of HNCO, we see a notably weaker detection of SiO. Both are centred around ∼ 30 km s^{-1}, compared to v_{sys}. In the position West Knot 1, we see only a marginal increase in SiO signal above the baseline noise, despite this being the peak signal for SiO in the West. We also see weak emission for HNCO in this location. At the HNCO peak, West Knot 2, the SiO spectrum displays the same characteristics as in West Knot 1. This is not surprising judging from Figure 4.1, which shows a diffuse SiO peak. The HNCO peak is weak, but very broad if one assumes a single peak, with a linewidth of 399 ± 57 km s^{-1}.

We compare the velocity integrated line ratios for each location (Table 4.2). In the

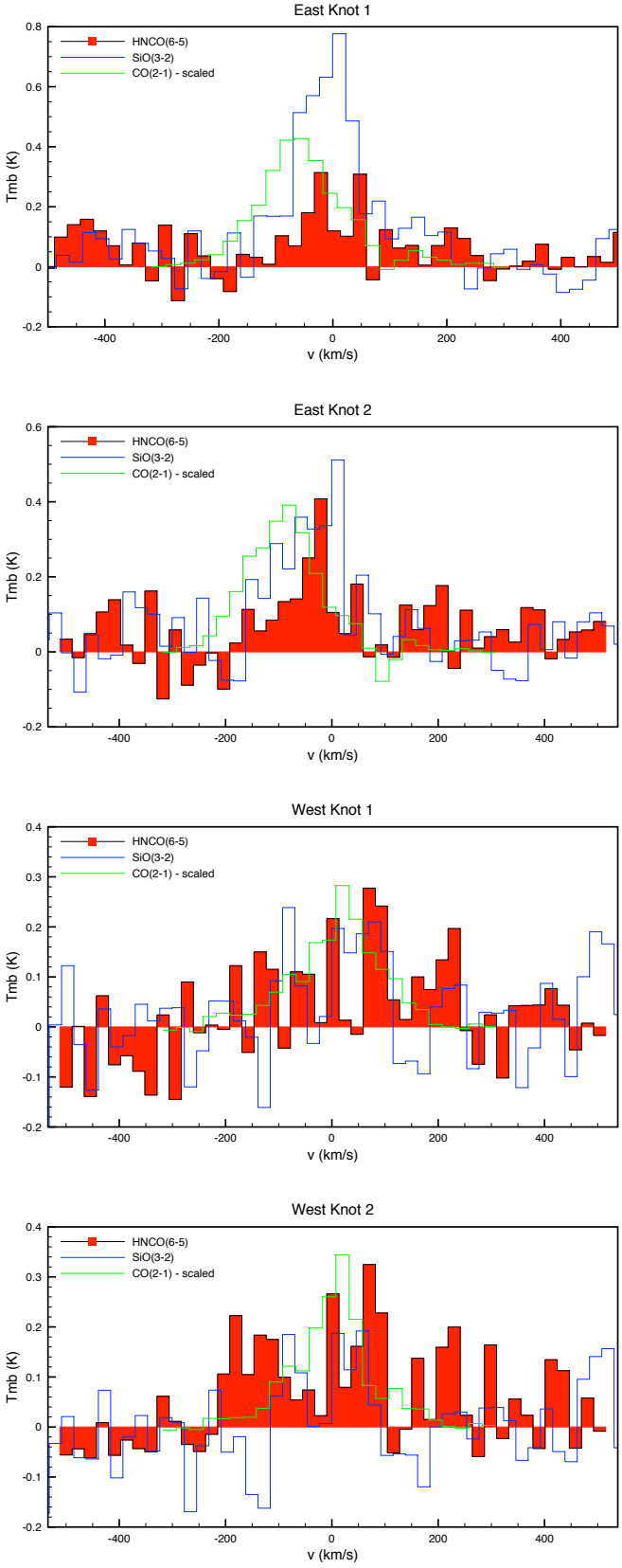

Figure 4.5: SiO$(3-2)$, HNCO$(6-5)$ and CO$(2-1)$ at four different positions listed in Table 4.1. Δv = 24 km s^{-1}.

.

Table 4.2: Velocity integrated line ratios

Location	HNCO(6 – 5) / SiO(3 – 2)
EK-1	0.48 ± 0.09
EK-2	0.38 ± 0.08
WK-1	1.8 ± 0.46
WK-2	3.5 ± 1.2

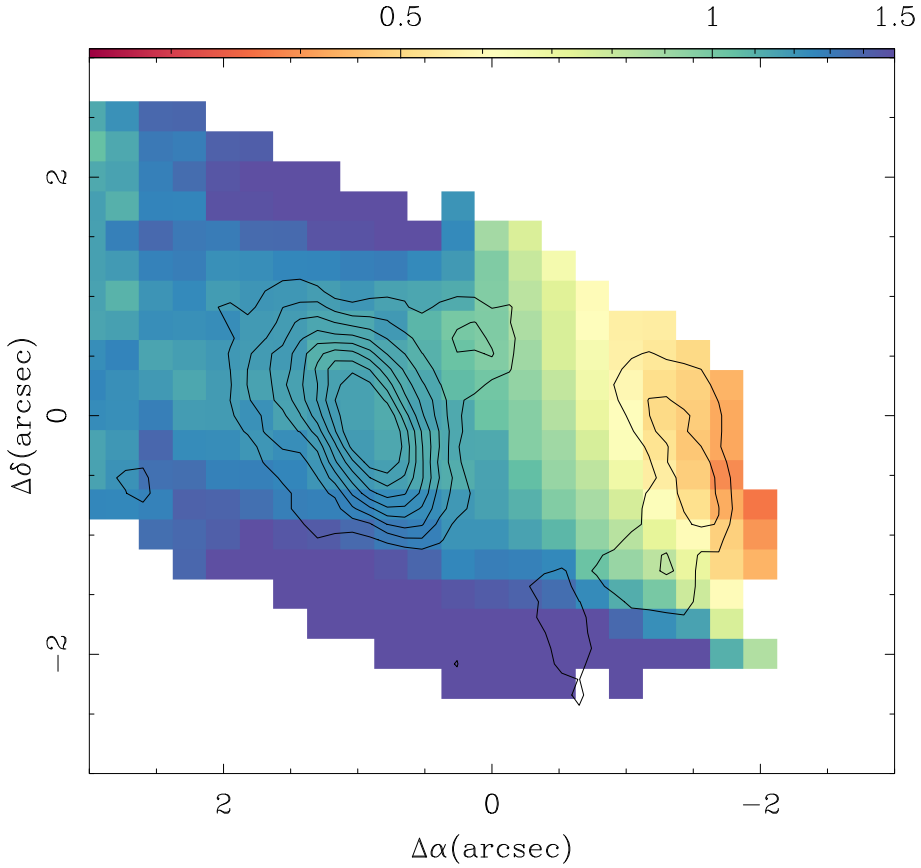

Figure 4.6: Colours: ratio of SiO(3 – 2)/SiO(2 – 1). Contours: SiO(3 – 2) at original resolution.

East, locations 1 and 2, SiO dominates by a factor of 3. In the West, West Knot 1, HNCO is a factor of 1.8 stronger, and twice that in West Knot 2. As a first approximation, the HNCO/SiO ratio may be considered a measure of the shock strength, since it takes a stronger shock event to increase the SiO abundance. This indicates that if we take the velocity integrated line ratios, shocks in the East Knot are significantly stronger than those in the West Knot. The average ratio in the East Knot is HNCO$(6-5)$ / SiO$(3-2)$ = 0.35 ± 0.13 and in the West Knot, HNCO$(6-5)$ / SiO$(3-2) = 2.5 \pm 1.3$. In addition, the shock strength might be considered to be relatively constant to the East, but due to the disparity in ratio in the two locations in the West Knot, shock velocities may differ on comparatively small scale.

In addition, using SiO$(2-1)$ data from García-Burillo et al. (2010), we produce a SiO$(3-2)$/SiO$(2-1)$ ratio map. To do this the resolution of the SiO$(3-2)$ observations is degraded to match the lower transition. The map is displayed in Figure 4.6. There is a clear gradient from East to West. In the East the ratio is ~ 1.2 but this drops to ~ 0.5 in the West. This compares well with previous observations in García-Burillo et al. (2014) and Viti et al. (2014), who find a comparatively higher excitation of other molecular lines in the East Knot compared with the West Knot.

Our velocity integrated line ratio (HNCO$(6-5)$ / SiO$(3-2)$) values in the East Knot are comparable to the inner disk of NGC 253, which were calculated using the slightly lower J transitions, HNCO$(5-4)$ / SiO$(2-1)$ (Meier et al. 2015). The NGC 253 compact (r $\approx$ 170 pc) region has a large quantity of dense gas and an increased rate of star formation. The values are also comparable to M82 (Martín et al. 2009b). The outer disk of NGC 253 shows similar ratios to that of the West Knot. The outer disk is suggested to be a region where gas is flowing radially inwards (in contrast to the radially outflowing gas in NGC 1068 (García-Burillo et al. 2000)). They also match well with the shocked Giant Molecular Clouds (GMCs) in the nearby spiral barred galaxy Maffei 2 (Meier and Turner 2012).

We note that we can not however simply correlate the shock strength with the HNCO/SiO ratio, especially as several gas phase reactions may contribute to the formation and destruction of both molecules. For example, HNCO is readily photodissociated at a rate $\sim$ 30 times faster that SiO (Sternberg and Dalgarno 1995). If in the presence of significant UV radiation, HNCO abundance will be significantly lowered compared to SiO. We would therefore see weaker emission and our ratios would be decreased by this effect.

4.4 Analysis

In this section we attempt to quantify the differences we observe between SiO $(3-2)$ and HNCO $(6-5)$ emission by position in the CND. There is strong SiO $(3-2)$ emission in the East Knot, peaking at East Knot 1, whereas HNCO $(6-5)$ emission is relatively weak in the same region. Conversely, we see that SiO $(3-2)$ and HNCO $(6-5)$ emission is more equal in the West Knot, and HNCO $(6-5)$ emission is stronger than SiO $(3-2)$ in West Knot 2. In order to explain these differences, we complete a three-phase analysis: a basic LTE analysis, a further radiative transfer modelling using RADEX (van der Tak et al. 2007), and a chemical modelling using UCL_CHEM, along the lines of the procedure set in Viti et al. (2014).

4.4.1 LTE

Here we calculate column densities, N, of SiO and HNCO, assuming local thermodynamic equilibrium (LTE) and optically thin emission. For that we use equation 1.

$$N_{mol} = 1.67 \times 10^{14} \frac{Q(T_{rot})}{\mu^2 \nu S} exp\left(\frac{E_u}{kT_{rot}}\right) \int T_{mb} dv \tag{4.1}$$

Where $Q(T_{rot})$ is the partition function, μ is the dipole moment in Debye, S is the line strength, E_u/k is the upper energy level in K, T_{rot} is the rotational temperature of the molecule. The units of the integral are K km s^{-1}; we therefore convert our data from Jy beam^{-1} to T_{mb}. Viti et al. (2014) find a minimum temperature of $\sim$ 50 K. We therefore use this temperature as our first T_{rot} in order to get the values of N(SiO) and N(HNCO) for each location. It is possible the average temperature of the gas is >50 K, especially if the gas is shocked. To account for this, we also calculate column densities for 100 K and 200 K. These temperatures also correlate with the findings of Viti et al. (2014). The calculated column densities are displayed in Table 4.3. HNCO $(6-5)$ is a band of several blended lines in our observations. To calculate a column density, we use average values from the strongest band, HNCO$(K_{\rm p}, K_{\rm o})$)=(0,6)-(0,5). It is possible that the gas density may be below the critical density of the transitions. However, since there may be shocks present, the density of the gas traced by these molecules may be much higher than the gas surrounding it. The critical densities, n_{cr}, of SiO$(3-2)$ and the strongest band of HNCO$(6-5)$ are in the order of 10^6 cm^{-3}. Since the gas may not be thermalised, our

LTE column density values should be used with caution.

Table 4.3: LTE column densities in each location

Location	N(SiO) (cm^{-2})	N(HNCO) (cm^{-2})
	T = 50 K	
EK-1	2.4×10^{14}	3.2×10^{14}
EK-2	1.5×10^{14}	6.8×10^{14}
WK-1	6.2×10^{13}	8.4×10^{14}
WK-2	4.9×10^{13}	1.3×10^{15}
	T = 100 K	
EK-1	4.3×10^{14}	7.2×10^{14}
EK-2	2.6×10^{14}	1.5×10^{15}
WK-1	1.1×10^{14}	1.9×10^{15}
WK-2	8.6×10^{13}	2.9×10^{15}
	T = 200 K	
EK-1	8.0×10^{14}	2.0×10^{15}
EK-2	4.8×10^{14}	4.2×10^{15}
WK-1	2.1×10^{14}	5.2×10^{15}
WK-2	1.6×10^{14}	7.8×10^{15}

Comparing the column densities from Table 4.3, we notice that, in East Knot 1, where SiO emission peaks, column densities for SiO and HNCO are quite similar, but N(HNCO) is greater than N(SiO) at all temperatures. In East Knot 2, the peak of HNCO emission in the East Knot, N(HNCO) is half an order of magnitude higher than N(SiO). In the West Knot, N(HNCO) is between 1-2 orders of magnitude greater than N(SiO). This is assuming that SiO and HNCO emission is coming from the same gas component. However, under the assumption that SiO traces a fast shock and HNCO traces slower shocks, the gas emitting in SiO may well be warmer. We find that, if one assumes the gas emitting SiO and HNCO has the same temperature, then East Knot 2, and West Knot 1&2, still show that HNCO column density is higher than that of SiO. In East Knot 1, if the temperature of the SiO emitting gas is 100 K, and the HNCO emitting gas is 50 K, N(SiO) is greater than N(HNCO). If N(SiO) is then calculated assuming the temperature is 200 K, it becomes greater than N(HNCO) by a factor of ~ 2.5.

4.4.2 RADEX

In order to further characterize the emitting gas in SiO and HNCO, we run a RADEX (van der Tak et al. 2007) analysis. Since we only have one transition for each molecule, we also take the SiO$(2-1)$ line from García-Burillo et al. (2010) and the HNCO$(5-4)$

line from Takano et al. (2014). We complete a separate analysis for each location, using the brightness temperature of the four observed lines, therefore assuming a common filling factor. Our grid of models are run varying hydrogen number density from 10^3 cm^{-3} to 10^8 cm^{-3} and temperature from 10 K to 300 K. We use an initial input of column density based on our LTE calculations at 50 K. We then vary the column density by up to an order of magnitude. For the purpose of our analysis, we divide our model grid in subsets where we consider a set of models as models with a constant column density. This results in sets containing over 15,000 models. RADEX requires an input value for column density over line width ($N_{mol}/\Delta V$). We measure the line width by fitting a Gaussian to each line. The mean value of the line width is $\sim$ 150 km s^{-1}. This is the value we use for all our RADEX models. We vary this value by a factor of 2 as a check of its influence on our results. A smaller or larger line width has a marginal effect on our best fit parameters, but not enough to alter our conclusions.

We calculate a reduced χ^2 for each model compared to observations in each of our four locations. The reduced χ^2 equation used is the same as in Viti et al. (2014), although here we compare observed and modelled brightness temperature, not ratios:

$$\chi^2_{\rm red} = \frac{1}{\rm K}\sum_{n=1}^{\rm K}[\log(\rm T_o) - \log(\rm T_m)]^2/\sigma^2 \tag{4.2}$$

Where K is defined as N - n, where N is the number of observed lines and n is the number of varied parameters. In this case, N = 4 and n = 2. $\rm T_o$ and $\rm T_m$ are observed and modelled brightness temperature respectively, and σ is the uncertainty on the observed brightness temperature. We estimate σ to be 20% for all our observations based on the systematic uncertainty from calibration. Our results are displayed in Figure 4.7. We find that the lowest median χ^2 values are for models within the set ran with our initial LTE estimated column density for 50 K, although the differences are quite small. In this section we therefore concentrate on analysis of this set, but note that the results of using a higher column density would lead to similar conclusions.

We describe below our findings per each location:

- East Knot 1: the values of χ^2 are generally quite high. Nevertheless the lowest χ^2 constrains both density and temperature at around 10^5–10^6 cm^{-3} and 10–30 K.

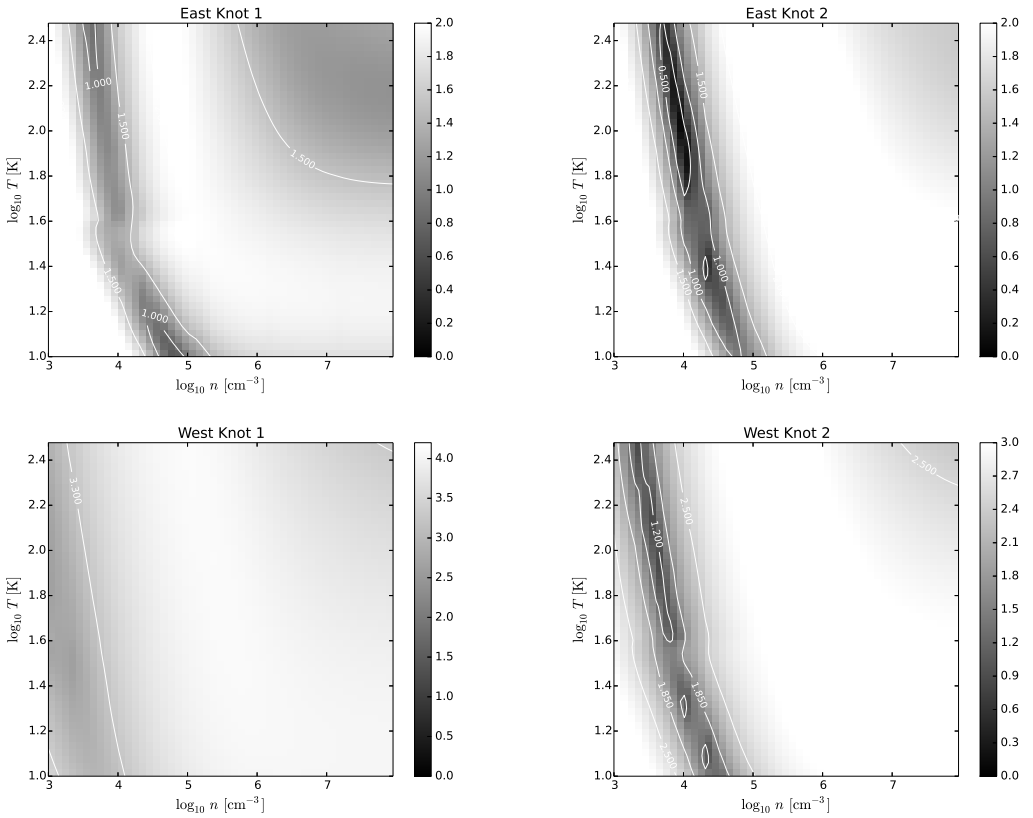

Figure 4.7: Log of χ^2 fits from RADEX modelling for each location with varying temperature and density. Darker regions show a lower χ^2 and therefore better fit than lighter regions

However we also note that if one accepts log of χ^2 of just 0.2 higher than the best fit then densities may be as high as 10^7 cm^{-3} and temperatures between 40-65 K.

- East Knot 2: we obtain a fairly low log of χ^2 for a density between 10^4 and 10^5 cm^{-3} but temperature is quite poorly constrained as low χ^2 values are found across our entire temperature range.

- West Knot 1: this location is not well fit at all. The lowest (but still very high) χ^2 are found for either a combination of very low densities ($< 10^4$ cm^{-3}) and a large range of temperatures or very high densities and temperatures ($> 10^7$ cm^{-3} and $>$ 250K respectively).

- West Knot 2: this location is well fit by a density between 10^4–10^5 cm^{-3}; however we are not able to constrain a temperature.

While we were not able to find a convincing solution for West Knot 1, two main results for the remaining Locations emerged: (i) the density of the gas is at least 10^4 cm^{-3}, with

East Knot 1 having the highest density and East Knot 2 and West Knot 2 having a similar density (consistent with all previous work on the dense gas of NGC 1068 from Krips et al. 2011 and Viti et al. 2014); (ii) the temperature of the gas is generally not well constrained. This may be due to the upper energy levels of our transitions being significantly lower than the actual temperature of the gas. Viti et al. (2014), using mostly transitions with upper energy levels similar to that of HNCO$(6-5)$, conclude that the temperature of the gas in the West Knot may be as high as 200 K. For HNCO$(6-5)$, $E_u \approx 65$ K. Alternatively, it also may be an indication that the gas component(s) where SiO and HNCO emission originates from are not at a constant temperature. This is not surprising since the emission may be coming from a shocked region, where temperatures vary swiftly with time and space (and the cooling rate is proportional to the square of the density). We investigate the shock chemistry that may give rise to the SiO and HNCO emissions in the next Section.

Since we cannot constrain temperature, we complete a second grid of RADEX models using the temperature for the East and West Knots found in Viti et al. (2014). These are $\sim$50 K for our East Knot locations and $\sim$200 K for the West Knot locations. We vary column density and gas density. We find that in both East Knot locations, the observations are best fit for a gas density of 10^4–10^5 cm^{-3}, which is consistent with previous RADEX findings. We find a column density, N, of both molecules of 10^{14}–10^{15} cm^{-2}, which is consistent with the fact that LTE values are lower limits. The West Knot locations are both poorly constrained. At a gas density of 10^5 cm^{-3} we find similar χ^2 values for a range of solutions for column density, N, from 10^{12}–10^{15} cm^{-2}. These results are summarised in Table 4.4. Our RADEX modelling findings are very similar to what has been found previously in Viti et al. (2014). However we are much more limited by the number of transitions we have. Our RADEX results must be used with caution. RADEX treats optical depth with an escape probability approximation and assumes a single phase homogenous medium. This leads to two complications. Firstly, we would not expect our observations to be well fit by a single temperature and density, because we are observing a large region with a range a physical characteristics. Secondly, for a true, absolute χ^2 analysis, it is important to know to a good degree of accuracy, the error on the result. The approximation in RADEX, discussed in Chapter 1, can sometimes lead to a large uncertainty. Tunnard and Greve (2016) find this to reach as high as a factor of 10 when attempting to recover RADEX input parameters, and that the error varies by a large degree. The best we can do is use the best estimate of error which is the calibration error

on the telescope. Therefore, while our analysis should give a reasonable estimate of the relative likelihood of the parameters fitting the average conditions of the region we observe, we cannot really use a χ^2 value to give an absolute probability of the model fitting the data.

Table 4.4: RADEX modelling results assuming a fixed temperature, showing ranges for which a best fit is found in each location

Location	T (K)	n(H_2)	N(SiO) (cm^{-2})	N(HNCO) (cm^{-2})
EK-1	50	10^4–10^5 cm^{-3}	10^{14}–10^{15} cm^{-2}	10^{14}–10^{15} cm^{-2}
EK-2	50	10^4–10^5 cm^{-3}	10^{14}–10^{15} cm^{-2}	10^{14}–10^{15} cm^{-2}
WK-1	200	10^5 cm^{-3}	10^{12}–10^{15} cm^{-2}	10^{13}–10^{15} cm^{-2}
WK-2	200	10^5 cm^{-3}	10^{12}–10^{15} cm^{-2}	10^{13}–10^{15} cm^{-2}

4.4.3 Chemical modelling

Following the methodology of Viti et al. (2014) we now adopt a chemical model in order to determine the origin of the emission in HNCO and SiO as well as shed light on the temperature of the gas. In particular, we investigate whether the passage of shocks may significantly affect the production or destruction of SiO or HNCO in the gas. We use UCL_CHEM, a time-dependent gas-grain chemical model (Viti et al. 2004a) coupled with a parametric shock code (Jiménez-Serra et al. 2008). Details of the coupled code can be found in Viti et al. (2011) and in Chapter 1 of this thesis. As discussed previously, the model is ran in two phases. Phase I simulates the gas phase chemistry during the formation of high or medium density clumps, along with a freeze out of gas phase species onto dust grain mantles and possible subsequent surface reactions. Other than molecular hydrogen, all initial species are atomic. Initial abundances were set to be solar, other than Si, where we vary an amount that is depleted into dust grain nuclei: this parameter is of particular importance when discerning between shock and non-shock models because in the former the Si in the nuclei would be sputtered back into the gas phase. Phase II simulates either the passage of the shock or simply an increase in gas and dust temperature due to energetics events such as a starburst; it then follows the time evolution of the chemistry in the gas and on the grain mantles. For the shock models this phase includes a plane-parallel shock component with a set velocity, V_s, temperature, T_{max} and saturation time, t_{sat}. For both shock and non shock models, the grain mantle, where both HNCO and Si

are present, is sublimated; in addition in the shock models the nuclei of the dust grains may be sputtered, depending on the shock velocity.

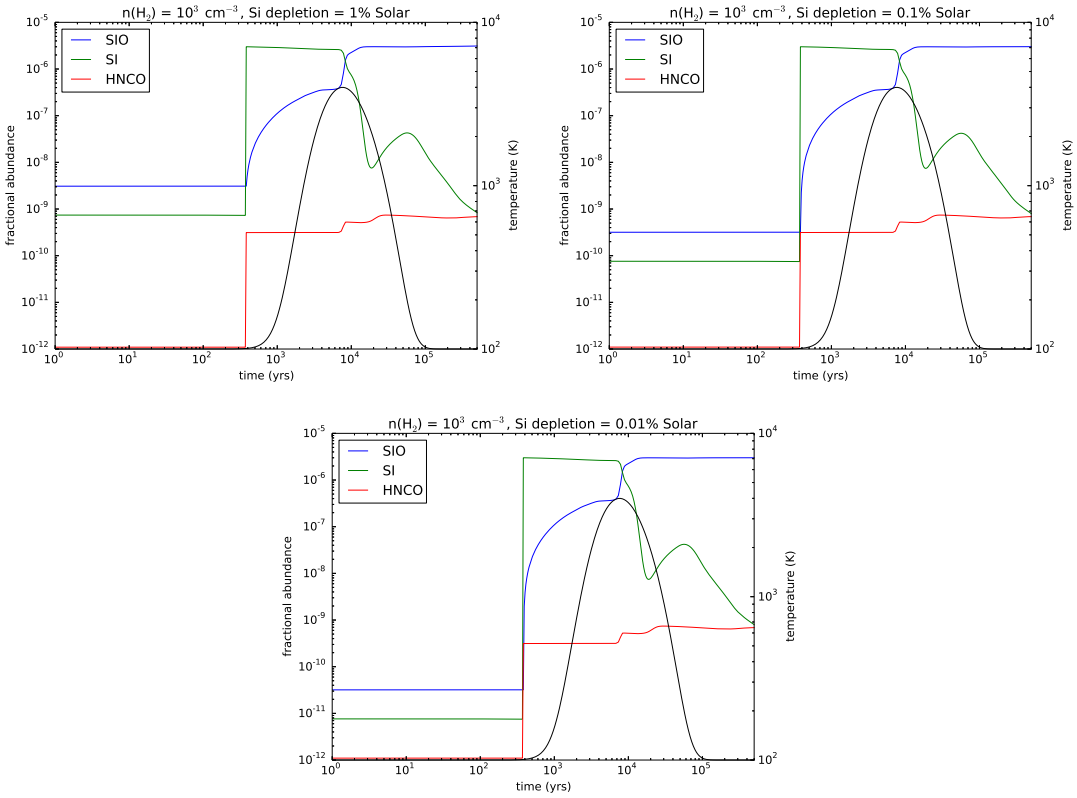

Figure 4.8: Chemical shock modelling showing Si, SiO and HNCO. These are fast (60 km/s) shock models 1-3.The black line shows temperature variation.

We run a grid of models, listed in Tables 4.5 and 4.6. García-Burillo et al. (2014) find that the outflow in NGC 1068 has velocities up to 100 km s^{-1}, but which vary strongly over the regions observed. The area is large and we are not just observing a single shocked area. As a representative fast shock, we take a value of 60 km s^{-1} for our models. At this velocity, some grain sputtering occurs; the percentage of Si from the grains that gets sputtered is debated: we use the results from the modelling of Jiménez-Serra et al. (2008), see their Figure 6, for the purpose of this study and we shall therefore assume that 10% of the Si locked in the dust grains will sputter. At these velocities, all the mantle is sputtered.

We also investigate the possibility that there are some much weaker shock events occurring, and take a value of 20 km s^{-1}. At this velocity, sputtering from grain nuclei is negligible but mantles should return to the gas-phase quite efficiently (Gusdorf et al. 2008). In addition, we run non-shock models, as a check to see if we could produce observable quantities of both species without the need for shock chemistry. Note that

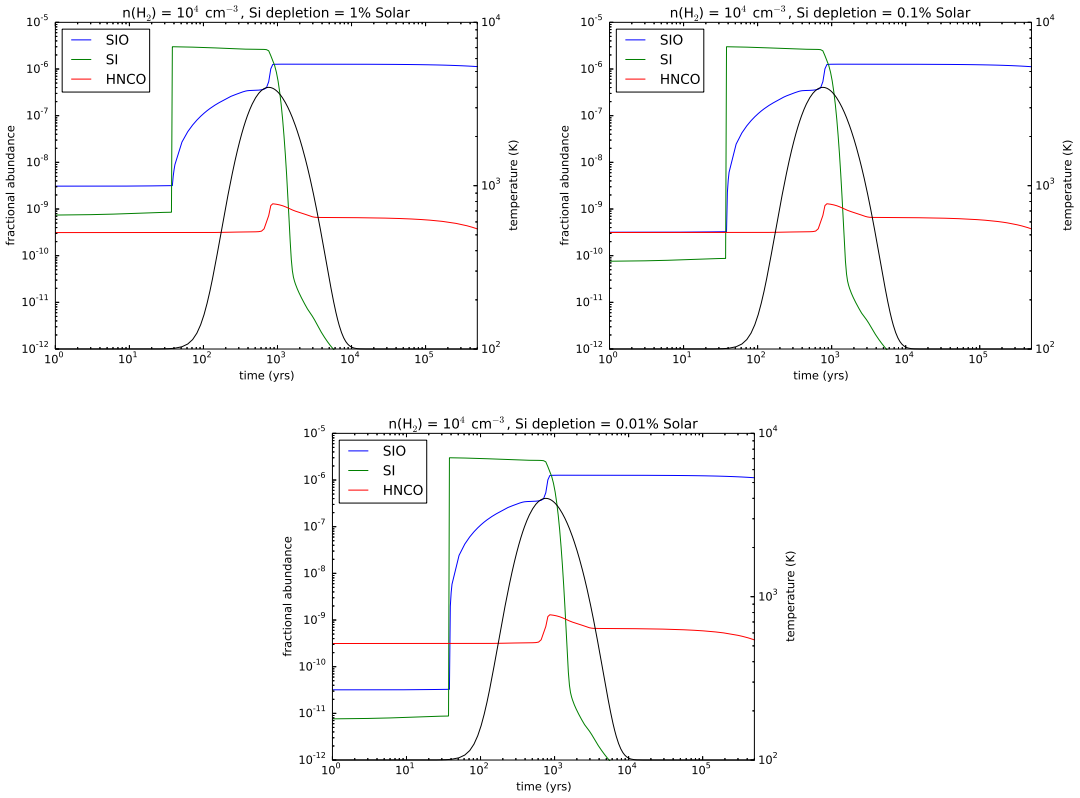

Figure 4.9: Chemical shock modelling showing Si, SiO and HNCO. These are fast (60 km/s) shock models 4-6. The black line shows temperature variation.

the non shock models are still run at a temperature (typical of regions where stars have formed) that leads to mantle sublimation. Most silicon is locked up in grain nuclei and silicon is therefore significantly depleted from solar values. As much as 99.96% of silicon may be depleted into dust grain cores (Jiménez-Serra et al. 2008; Snow and Witt 1996; Anders and Grevesse 1989). This value has some uncertainly so we adopt three values for our initial abundance of Si of X(Si) = 1%, 0.1% and 0.01% of the solar value. We hold the value of the UV radiation field at the standard interstellar value. The high extinction in the dense gas we model, even pre-shock, would shield the gas so that an increase in UV would have little effect (Viti et al. 2014).

Krips et al. (2011) as well as Viti et al. (2014) find that the gas in the regions we are observing has a density, $n(\mathrm{H_2}) \geq 10^4$ cm^{-3} (also confirmed by our RADEX analysis) and that the average gas temperature between 60 and $\sim$ 200 K. We choose to run our shock models with a pre-shock density of 10^3-10^5 cm^{-3} (leading to a post-shock density of $\geq$ 10^4 cm^{-3}). At 10^3 cm^{-3} the gas and the dust is not coupled. Therefore the temperature of the dust will be lower than the gas temperature, and at this density the dust grain

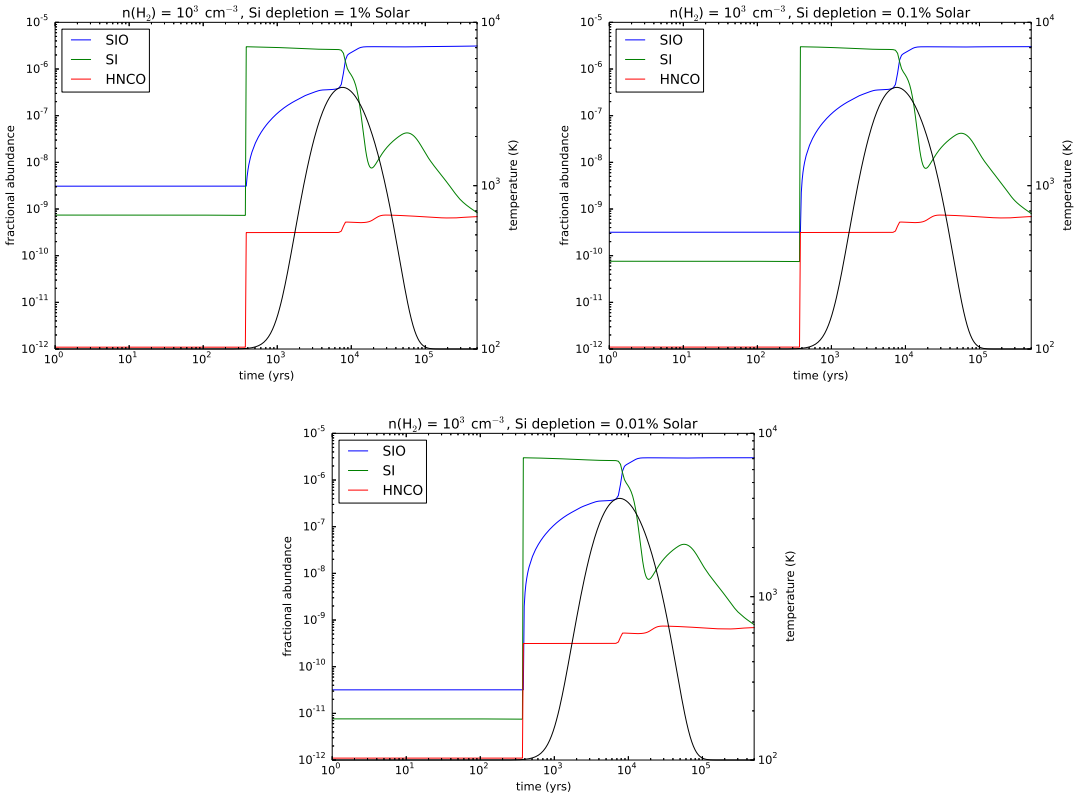

Figure 4.10: Chemical shock modelling showing Si, SiO and HNCO. These are fast (60 km/s) shock models 7-9. The black line shows temperature variation.

mantles are not sublimated until the shock occurs and temperature and density increase. At higher densities, we assume coupling between gas and dust and hence the mantles are already sublimated before the shock occurs. Our non shock models are completed using density 10^4-10^5 cm^{-3}.

In Figures 4.8 to 4.10, we show the fractional abundance (with respect to the total number of hydrogen nuclei) of Si, SiO and HNCO for our fast shock models. The main difference between the models with a very low pre-shock density and the higher density ones are that for the former there is no mantle sublimation until the shock arrives, while in the latter the mantle thermally sublimates; this leads to a slightly different behaviour for HNCO which always undergoes an enhancement during the shock passage: however for higher pre-shock densities it also seems to decrease again once the shock has passed. In all the fast shock models Si is significantly enhanced as the shock sputters the grain core. The Si, now in the gas phase, reacts quickly with O_2 and OH during the shock event. In addition, at the peak of the shock, Si reacts with CO to form SiO, the very high temperatures overcoming its large activation barrier. These reactions cause a rapid rise

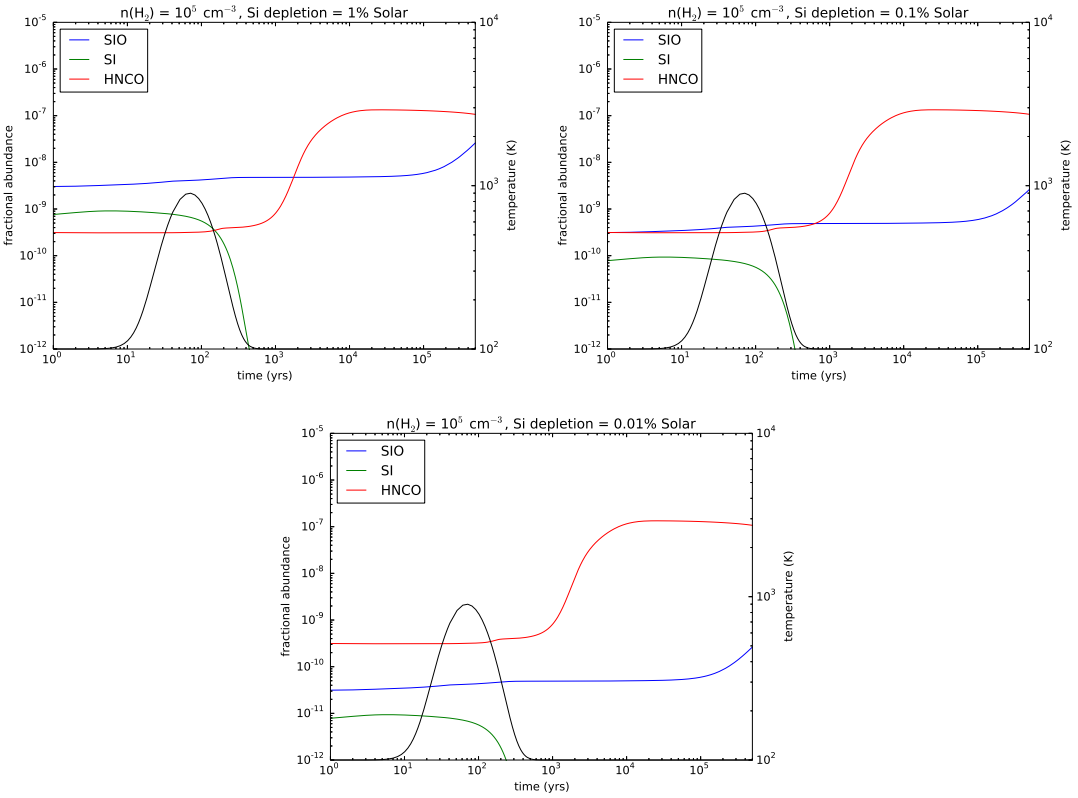

Figure 4.11: Chemical shock modelling showing Si, SiO and HNCO. These are slow (20 km/s) shock models 10-12. The black line shows temperature variation.

in SiO. SiO abundance levels off after the shock but Si falls, reacting in particular with C_2H_2 to form SiC_2. The amount of Si initially depleted into olivine grain cores does not have a large impact on the final abundance of SiO. This is because much of the Si depleted returns to the gas due to sputtering during the shock.

In Figures 4.11 to 4.13, we show our weak shock chemical models. For the weak shock models the main difference, due to the different densities used, is in whether the gas and dust are coupled: in the latter case sublimation of the icy mantles occurs before the shock arrives, as in the case of the fast shock models, while for the low density models the icy mantles are released back to the gas phase only when they get sputtered by the passage of the shock. However, because the density is very low (10^3 cm^{-3}) hardly any freeze out takes place in Phase 1. Sputtering of the grain cores does not occur. In both low and high density models we find that following the shock the HNCO abundance increases by up to 3 orders of magnitude. The increase is not so pronounced for the SiO abundance. In this case the amount of Si depleted to the dust is important in determining the final SiO abundance, as the weaker shock does not sputter the grain core.

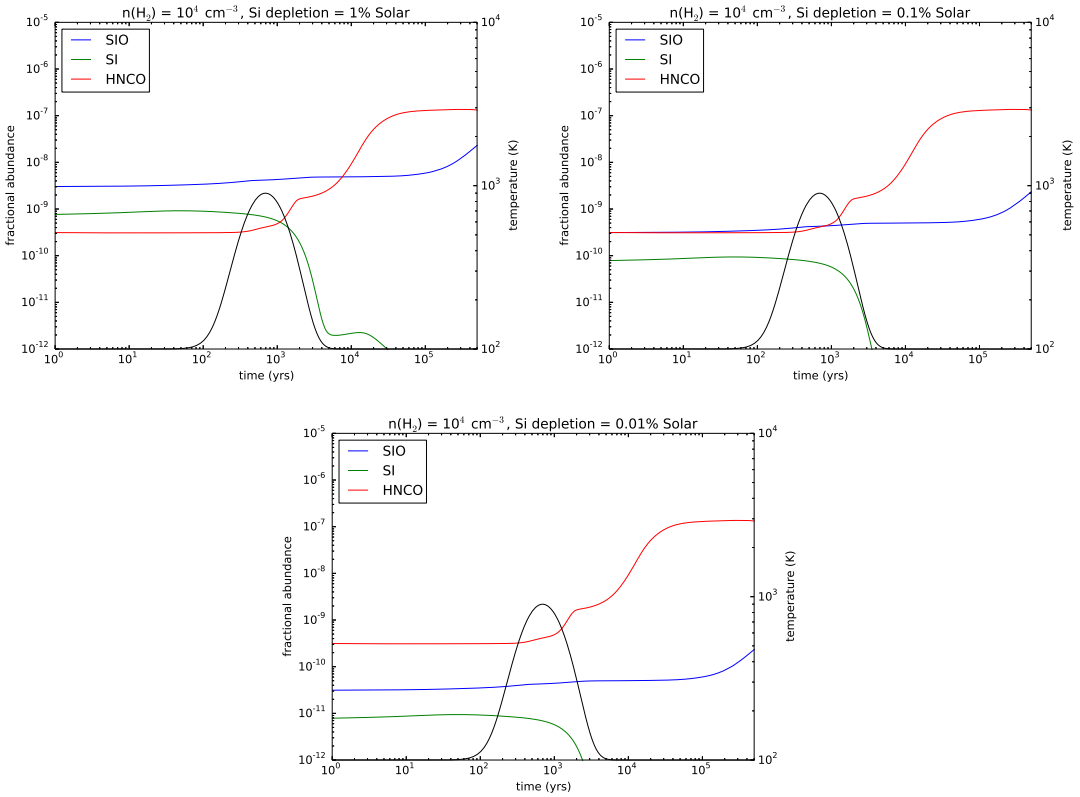

Figure 4.12: Chemical shock modelling showing Si, SiO and HNCO. These are slow (20 km/s) shock models 13-15. The black line shows temperature variation.

In Figures 4.14 to 4.15, we show our chemical models without any shocks. We see here a very small rise in SiO over time. HNCO increases significantly at late times. These models were ran at a density always equal or higher than 10^4 cm^{-3}; hence the gas and dust are assumed to be coupled and mantle sublimation therefore always occurs. The initial elemental Si depletion is important in determining the final SiO abundance, as nothing returns to the gas phase from the dust grain cores. In order to compare the observed fractional abundances with our chemical models, we can calculate a fractional abundance from the column densities we calculated from our RADEX modelling. This is subject to two important limitations. Firstly, we must assume a CO/H_2 fraction. We take the canonical value of 10^{-4}, which also matches well with what we find in our models. In addition, the chemical modelling only gives fractional abundances at single points in time and space. Our observations encompass a very large region, which will include a large gradient of abundances. So while the chemical modelling is very useful for seeing trends in production or destruction of different molecules, it is difficult to quantitively and directly compare to observations. Nevertheless, we calculate the fractional abundance X(SiO) $\approx$

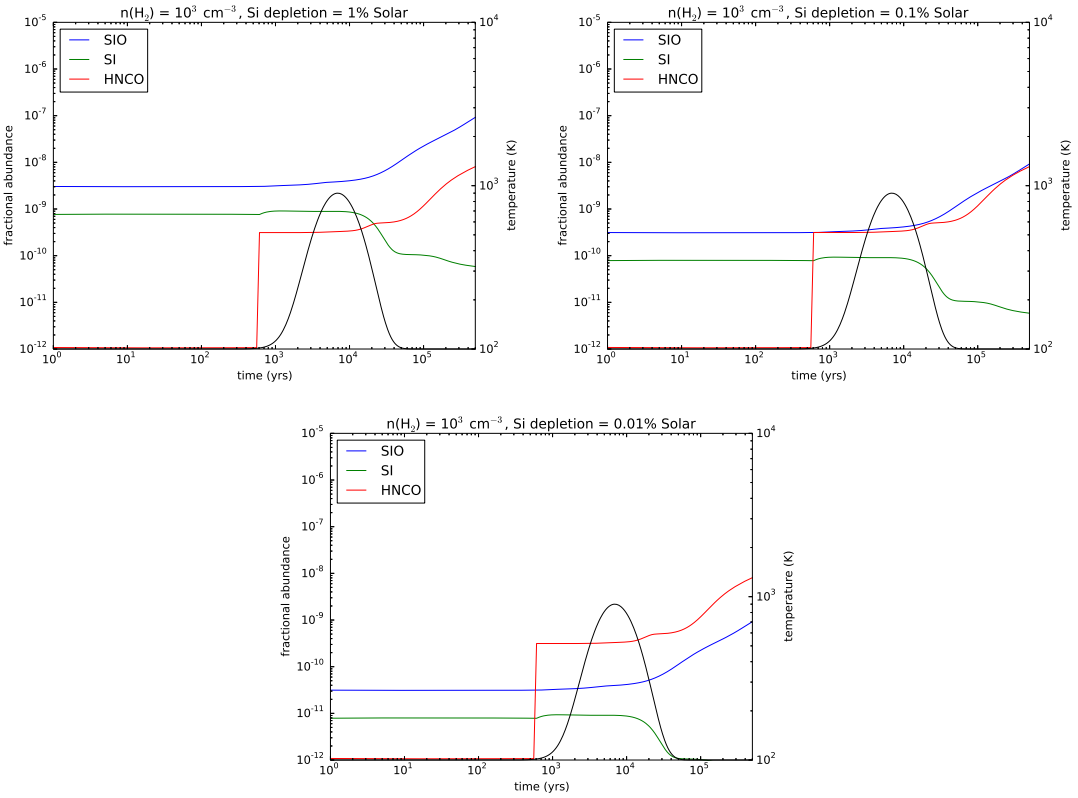

Figure 4.13: Chemical shock modelling showing Si, SiO and HNCO. These are slow (20 km/s) shock models 16-18. The black line shows temperature variation.

10^{-8} and X(HNCO) $\approx 10^{-9}$ in the East Knot locations. The column density estimates in the West Knot are very broad but give X(SiO), X(HNCO) $\approx 10^{-11}$ to 10^{-8}. The values found in the models can best be described as an upper limit given that our observations cover an area greater than a single shocked region. In the fast shocked models, X(SiO) peaks at $\sim 10^{-6}$, comfortably more than observations. X(HNCO) peaks are $\sim 10^{-9}$, roughly the same as observed. As this is an upper limit, it seems unlikely that the HNCO we observe is being produced significantly in fast shocks. In the weak shock and no shock models, we see the opposite. X(HNCO) peaks at $\sim 10^{-7}$ but X(SiO) only reaches $\sim 10^{-8}$. This indicates that fast shocks are likely to be producing SiO, whereas weak shocks, or warm, dense gas is likely responsible for the HNCO we observe.

To further this analysis, we quantify the difference that the passage of a shock makes by comparing a *fast* shock model with a non shock model ran at the same density (e.g. Model 7 and 22): we find that HNCO is in fact much more enhanced in the non shock models implying that although a fraction does come from the mantles (which evaporate in both cases, at least for the high density models) the bulk of its increase happens in

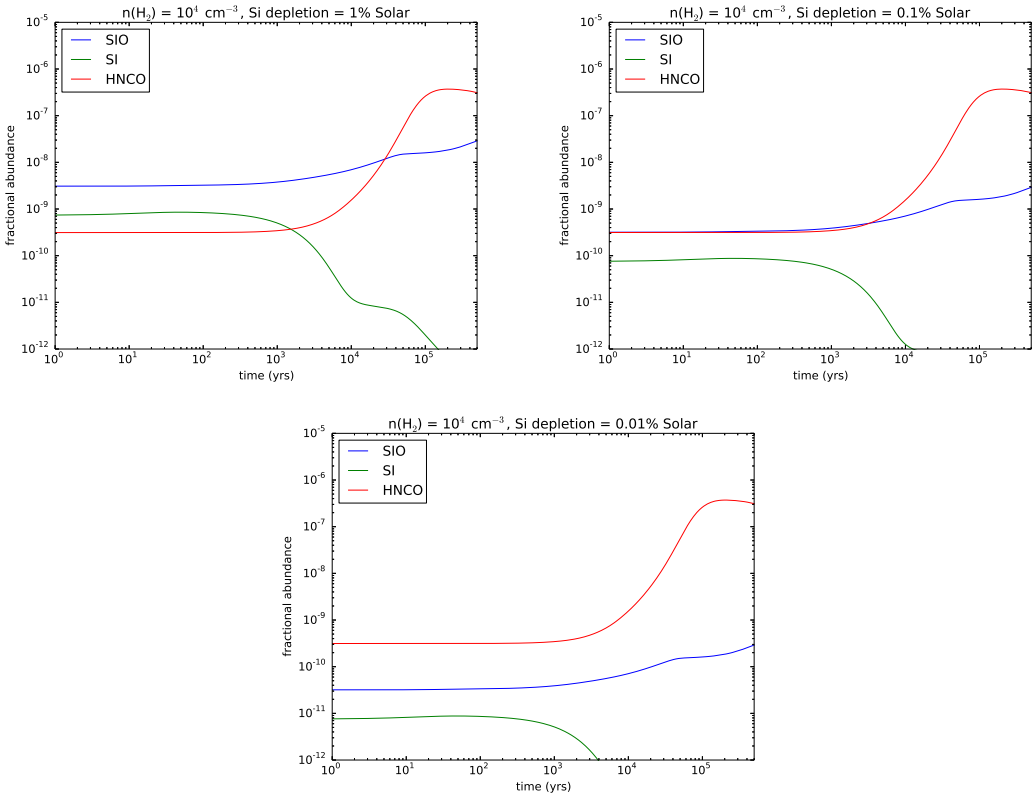

Figure 4.14: Chemical modelling with no shocks showing Si, SiO and HNCO. Models 19-21.

the warm gas phase after the ices sublimate. However, surprisingly, this increase does not occur in the shock models where the temperature is even higher. The main route to formation in the gas phase for HNCO is Reaction 4.3.

$$CH_2 + NO \longrightarrow HNCO + H \tag{4.3}$$

During the fast shock, NO is very rapidly destroyed through reaction with atomic hydrogen (Reaction 4.4), which is enhanced.

$$H + NO \longrightarrow OH + N \tag{4.4}$$

This can be seen clearly in Figure 4.16. Reaction 4.4 only proceeds at very high temperatures and does not occur at all during the slow shock or without a shock. This is confirmed by the fact that in a slow shock model HNCO does in fact increase at late times

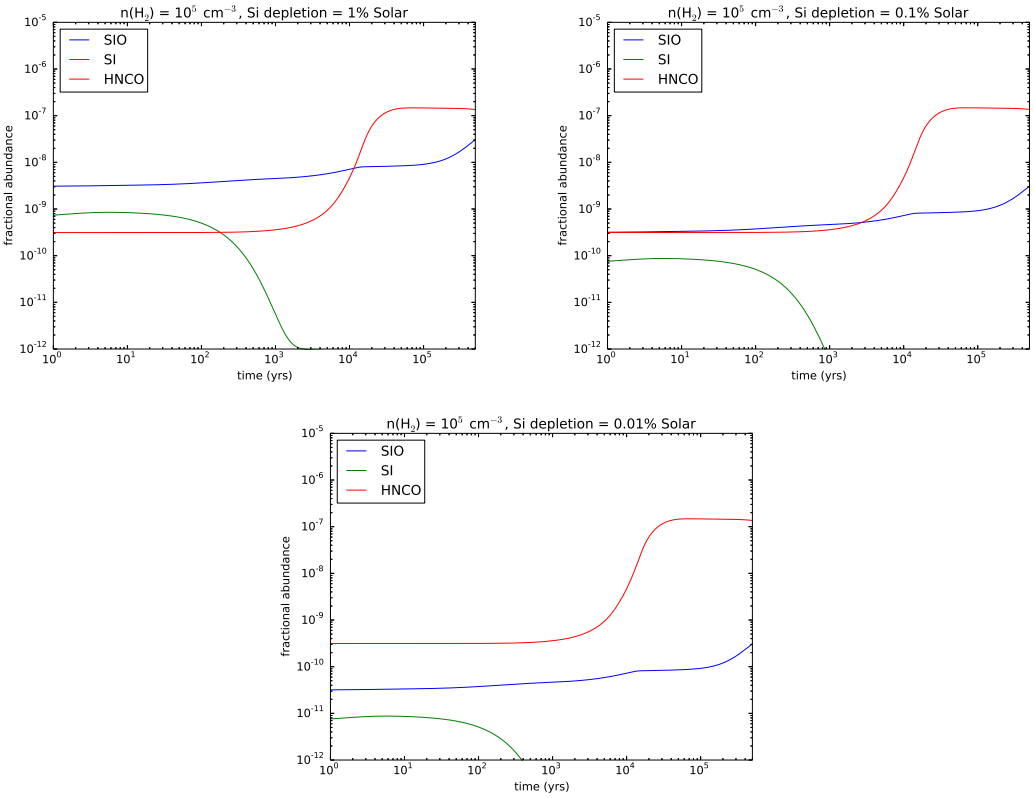

Figure 4.15: Chemical modelling with no shocks showing Si, SiO and HNCO. Models: 22-24.

as much as in a non shocked model. SiO on the other hand clearly needs a fast shock to be enhanced and the level of enhancement will depend on the initial elemental depletion. Clearly there are too many parameters that play a role for us to be able to quantitatively fit the HNCO and SiO observed in the four different locations; nevertheless we do have an explanation for the anti-correlation of these two species: a high SiO and a low HNCO seem to indicate the presence of a fast shock while a low SiO and a high HNCO imply either a very slow shock or a warm dense non shocked gas.

4.5 Conclusions

We have used the Plateau de Bure Interferometer to map two shock tracers, SiO and HNCO. SiO$(3-2)$ is detected strongly to the East of the AGN and to some extent to the West. HNCO$(6-5)$ is detected more strongly to the West, but is also detected in the East. The emission of the two lines is slightly offset from one another. We extracted spectra to analyse from the four peak emission locations of both lines. This allowed us to

Table 4.5: Chemical shock model input parameters

Model number	n(H_2) (cm^{-3})	V_s (km s^{-1})	T_{max} (K)	t_{sat} (yr)	Si Depletion
1	10^3	60	4000	380	1% Solar
2	10^3	60	4000	380	0.1% Solar
3	10^3	60	4000	380	0.01% Solar
4	10^4	60	4000	38	1% Solar
5	10^4	60	4000	38	0.1% Solar
6	10^4	60	4000	38	0.01% Solar
7	10^5	60	4000	3.8	1% Solar
8	10^5	60	4000	3.8	0.1% Solar
9	10^5	60	4000	3.8	0.01% Solar
10	10^3	20	900	570	1% Solar
11	10^3	20	900	570	0.1% Solar
12	10^3	20	900	570	0.01% Solar
13	10^4	20	900	57	1% Solar
14	10^4	20	900	57	0.1% Solar
15	10^4	20	900	57	0.01% Solar
16	10^5	20	900	5.7	1% Solar
17	10^5	20	900	5.7	0.1% Solar
18	10^5	20	900	5.7	0.01% Solar

Table 4.6: Chemical non-shock model input parameters

Model number	n(H_2) (cm^{-3})	Si Depletion
19	10^4	1% Solar
20	10^4	0.1% Solar
21	10^4	0.01% Solar
22	10^5	1% Solar
23	10^5	0.1% Solar
24	10^5	0.01% Solar

complete a RADEX radiative transfer modelling using our observations and SiO$(2-1)$ and HNCO$(5-4)$ from literature. We used parameters for the East and West Knot obtained by Viti et al. (2014) through a modelling of HCN, CS, CO and HCO^+. We found that in order to obtain a fit to our observations, the gas density, $n(H_2)$ must be higher than 10^4 cm^{-3}. We also found that, in general over the four locations, it was very hard to constrain a temperature. This may indicate that the gas as traced by HNCO and SiO is not at a constant temperature, consistent with a shocked region's varying temperature. Although this could also be due to the gas being of higher temperature than the upper energy levels of our transitions.

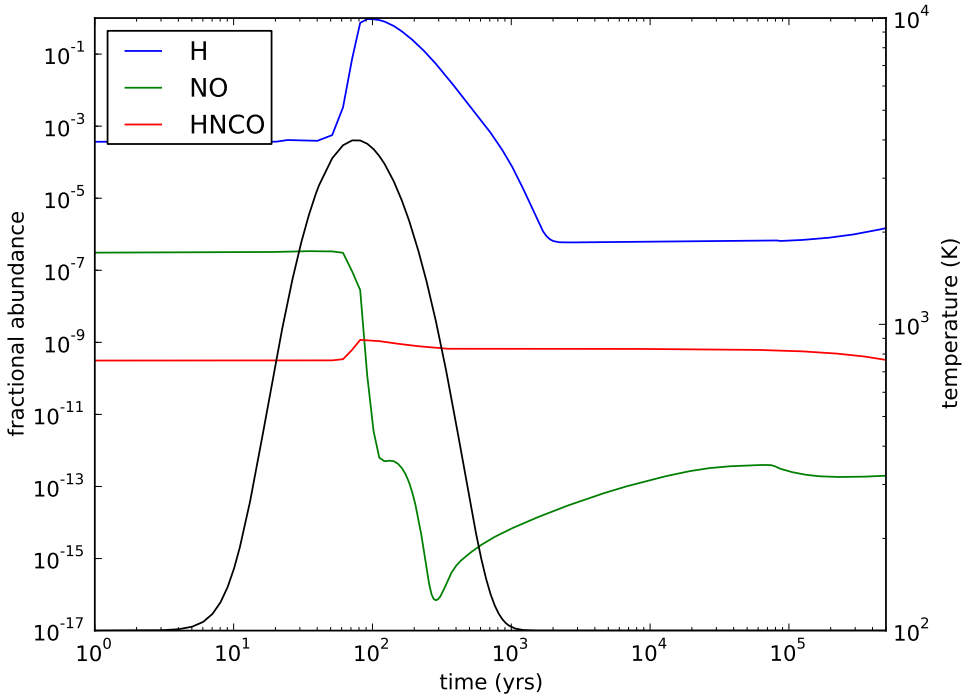

Figure 4.16: Chemical shock modelling showing H, NO, and HNCO. This is fast (60 km/s) shock model 7. The rapid decrease in NO is due to reaction with H. HNCO requires NO to form and therefore does not increase in abundance after the shock, in contrast to what is found in both slow (20 km/s) and non shocked models.

In order to further investigate the origin of the SiO and HNCO emission we completed chemical modelling. We modelled a representative fast shock (60 km s^{-1}), slow shock (20 km s^{-1}) and no shock. We found that SiO is significantly enhanced during the fast shocks, due to grain core sputtering of Si. It was slightly enhanced during the slow shock and was also produced to some extent in the no shock models. We found that HNCO actually decreased in the fast shock models due to the destruction of its precursor, NO. This occurs through reaction with atomic hydrogen and only proceeds at the very high temperatures found during the fast shock. To confirm this, during the slow shock, HNCO abundance significantly increases. HNCO also increased in abundance without need for a shock, in warm dense gas. This leads us to conclude that a high SiO but low HNCO abundance are indicative of a fast shock, whereas a low SiO and high HNCO abundance may indicate the presence of a slow shock, or of warm dense non shocked gas. Observations of the East Knot seem to therefore suggest gas in the region is heavily shocked. The offset of the HNCO peak to the SiO peak suggests that there may be regions in the East Knot away from the main shock that are undergoing a milder shock (particularly around our East

Knot 2). The weak SiO emission and stronger HNCO emission in the West Knot suggests that there are not fast shocks occurring. There may be slower shocks, or the gas may be warm, dense and non-shocked. The results of our RADEX analysis, where we struggle to constrain temperature in the West Knot, point to the milder shocks as the more likely solution.

The results in this Chapter should be of relevance to AGN feedback in NGC 1068. This galaxy is studied further in Chapter 5 and therefore this discussion has been deferred to Section 5.4.

Chapter 5

Spectral analysis of Molecular Lines in NGC 1068

The work in this chapter is based on observations first presented in García-Burillo et al. (2014) and Viti et al. (2014). Here follows a brief summary of the analysis already carried out in these two papers. The nearby Seyfert 2 galaxy, NGC 1068 has been observed with ALMA in several molecular lines. These are CO($3-2$), CS($7-6$), HCN($4-3$) and $HCO^+(4-3)$ in band 7 and CO($6-5$) in band 9. These transitions trace the moderately dense ($n(H_2) \sim 10^4$ cm^{-3}) molecular gas (CO) and the dense ($n(H_2) \sim 10^{5-6}$ cm^{-3}) molecular gas (CS, HCN and HCO^+). Continuum emission at 349 GHz and 689 GHz is also studied. The central 2 kpc has been observed with a spatial resolution 20 - 35 pc.

García-Burillo et al. (2014) show that continuum emission splits the observed region of the galaxy into three distinguishable regions: the circumnuclear disc (CND), the bar and the starburst (SB) ring. Within the CND, a torus of emission is off-centred from the AGN. There is substructure within the ring, notably, two knots to the west and east (the latter being the region of strongest emission). Within the bar, an arc of dust emission is detected 350 - 650 pc to the northeast of the AGN. The starburst (SB) ring is responsible for 72% of the integrated flux from the ALMA mosaic. It takes the form of two spiral arms, making up part of ring at a distance of 1.3 kpc from the AGN. The ring is only observed at 349 GHz in the continuum and displays a clumpy substructure, as can be seen

in Figure 5.1. Using CLUMPY torus models (Nenkova et al. 2008a,b), the gas mass of the central 20 pc torus around the AGN is found to be $M_{gas} = 2.1(\pm 1.2) \times 10^5\ M_\odot$. This is part of the total gas mass in the central 400 pc (to include the CND and the bar) of $M_{gas} = (5 \pm 3) \times 10^7\ M_\odot$.

The molecular emission in CO correlates with the continuum emission, following the pattern of the CND, the bar and the SB ring. In contrast, the majority of the CS($7-6$), HCN($4-3$) and $HCO^+(4-3)$ emission comes from the CND. However, there are some clumps of HCN($4-3$), $HCO^+(4-3)$ and CS($7-6$) in the SB ring. CS($7-6$) is detected marginally in the AGN position. In this location, the FWHM of HCN($4-3$) and $HCO^+(4-3)$ are much greater than that of CO($3-2$), indicating denser gas lying closer to the central engine. Using CO($3-2$) over the central 2.8 kpc region, a pattern of a rotating disk is found with an overall east-west orientation of its kinematic major axis - although this varies slightly over the three different regions. A molecular outflow is detected in the CND, building on previous work by Krips et al. (2011); García-Burillo et al. (2010). This is found to be flowing at a rate, $dM/dt \sim 63^{+21}_{-37}\ M_\odot \mathrm{yr}^{-1}$ from CO($3-2$). This is much higher than the star formation rate in the CND, indicating the outflow is driven by the AGN, rather than star formation. From CO($6-5$), HCN($4-3$) and $HCO^+(4-3)$, it is found that the outflow has a higher density counterpart, suggesting dM/dt may be a lower limit. This molecular outflow could hinder star formation in the central 400 pc. This is, however, likely counteracted by inflow from the outer disk identified in the velocity field.

A chemical analysis is undertaken by Viti et al. (2014) using molecular line ratios in the regions of the CND. These are also compared to a region in the SB ring that is especially strong in emission. The line ratios used include the observations with ALMA, complemented by further data from the PdBI. The regions of the CND are identified as previously - the AGN, East Knot and West Knot - with the addition of regions to the north and south of the AGN (North CND and South CND). Significant differences are found between these regions and the SB ring. The excitation of CO, HCO^+, and HCN is a factor of 2-5 greater in the CND on average. This is also the case with ratios of species with different critical densities.

CO rotation diagrams in the CND regions give rotational temperatures between 37 K (South CND) and 58 K (East Knot). These calculations are furthered with the use of the radiative transfer code RADEX (van der Tak et al. 2007). An analysis only using CO transitions finds that the coolest region is in fact the East Knot ($T < 80$ K) and the

warmest regions are the West Knot and AGN. When the analysis is completed using multi species transitions, the fit to the data is poorer, indicating multiple gas components. It is possible to fit all regions in the CND with the same set of parameters, indicating the possibility the regions are chemically similar. However, most regions allow the best fit of multiple models. The starburst ring is analysed in the lines available, finding a density of $5 \times 10^{4-5}$ and temperature $\sim$ 40 K.

A full analysis of the line profiles in each region was not undertaken and is the subject of this Chapter. An investigation of the spectra observed should unveil further the influence of the outflow and the AGN on the CND. In addition, the SB Ring as a whole has been little studied. By comparing spectra in different regions, we may be able to yield information as to the variation of its physical and chemical makeup. To supplement this work, we also complete an analysis of ratios between the lines, taken at points across the width of the line profiles. We focus in particular on ratios that have in the past been used as tracers of certain environments to test if they hold up for high resolution observations. In Section 5.1, we briefly introduce the observations. In Section 5.2, we investigate line profiles. This is split into Subsections 5.2.1 and 5.2.2, focusing on the CND and the SB Ring, respectively. Within each Subsection, we first introduce the general findings followed by our findings for each region within the CND or SB Ring. We then complete an analysis of the line ratios across the CND in Section 5.3. Finally, we sum up in Section 5.5.

5.1 Observations

Details of the observations and data reduction can be found in García-Burillo et al. (2014). We provide a very brief summary here. Maps were made using ALMA band 7 and band 9. The band 7 maps consisted of an 11 pointing mosaic, each with a FoV of 17″. Four spectral windows were observed which allowed for simultaneous observation of CO(J = 3–2) (345.796 GHz at rest) and HCO^+(J = 4–3) (356.734 GHz at rest) HCN(J = 4–3) (354.505 GHz at rest) and CS(J = 7–6) (342.883 GHz at rest). Band 7 maps encompass the CND and the SB Ring. Band 9 maps consisted only of a single pointing on the CND with a FoV of 9″ and was set up to cover CO(J = 6–5) (691.473 GHz at rest). The starburst ring is therefore not observed in CO(J = 6–5). Rest frequencies are corrected for recession velocity of $v_{sys}(HEL)$=1137 km s^{-1}. Relative velocities are now referred to v_{sys}.

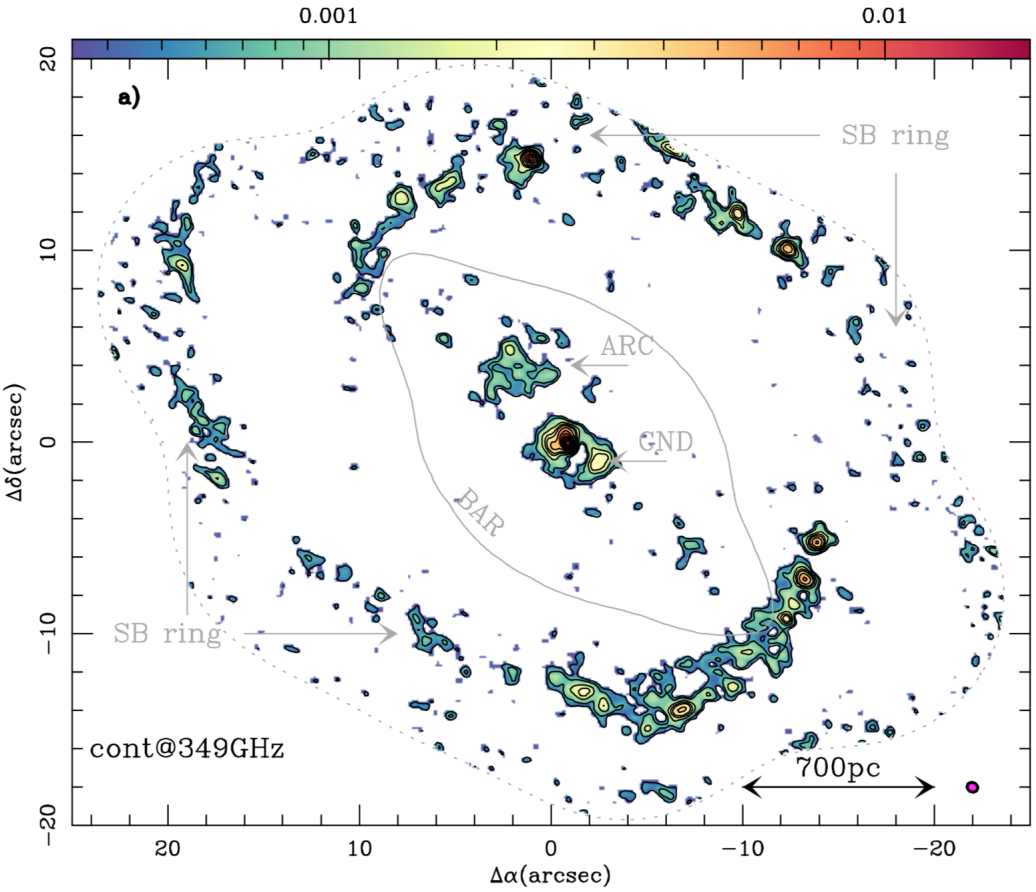

Figure 5.1: 349 GHz continuum emission map from García-Burillo et al. (2014), measured in Jy/beam and obtained with ALMA. The map shows the CND, the bar and the SB Ring. The beam size is shown in the bottom right hand corner.

5.2 Line Profiles

No analysis of the line profiles has been completed previously. This is where the focus of this Chapter is. Unless otherwise stated work completed from hereon is new. We study the line profiles in each region of the CND and then across separate clumps in the SB Ring. All lines have been converted from Jy/beam to brightness temperature (K) for consistent analysis.

5.2.1 AGN and Circumnuclear Disk

The coordinates for each region analysed here are displayed in Table 5.1, with the offset from the AGN. They are also displayed in Figure 5.2 (Viti et al. 2014; García-Burillo et al. 2014). In addition to the Figures displayed in throughout this section, we make use of line ratios in Figures 5.16 to 5.18 displayed at the end of this chapter, positioned

so as not to break up the text. These Figures display the ratios, $CO(6-5)/CO(3-2)$, $HCN(4-3)/HCO^{+}(4-3)$ and $HCN(4-3)/CS(7-6)$. A ratio is taken at 15 km s^{-1} each velocity bin where the detection level for both lines is at least 2σ. We also tabulate the velocity at which each line peaks and FWHM of each line. This has been completed using GILDAS software, CLASS (Guilloteau and Lucas 2000). Peak velocities are displayed in Table 5.2 and FWHM in Table 5.3. All spectra can also be found displayed separately for clarity in Appendix B.

Table 5.1: Co-ordinates of each region in the CND

Name	RA	Dec	ΔRA, ΔDec (″)
AGN	02:42:40.710	-00:00:47.94	0, 0
East Knot	02:42:40.771	-00:00:47.84	0.9, 0.1
West Knot	02:42:40.630	-00:00:47.84	-1.3, 0.1
North CND	02:42:40.710	-00:00:47.09	0, 0.85
South CND	02:42:40.710	-00:00:49.87	0, 2.03

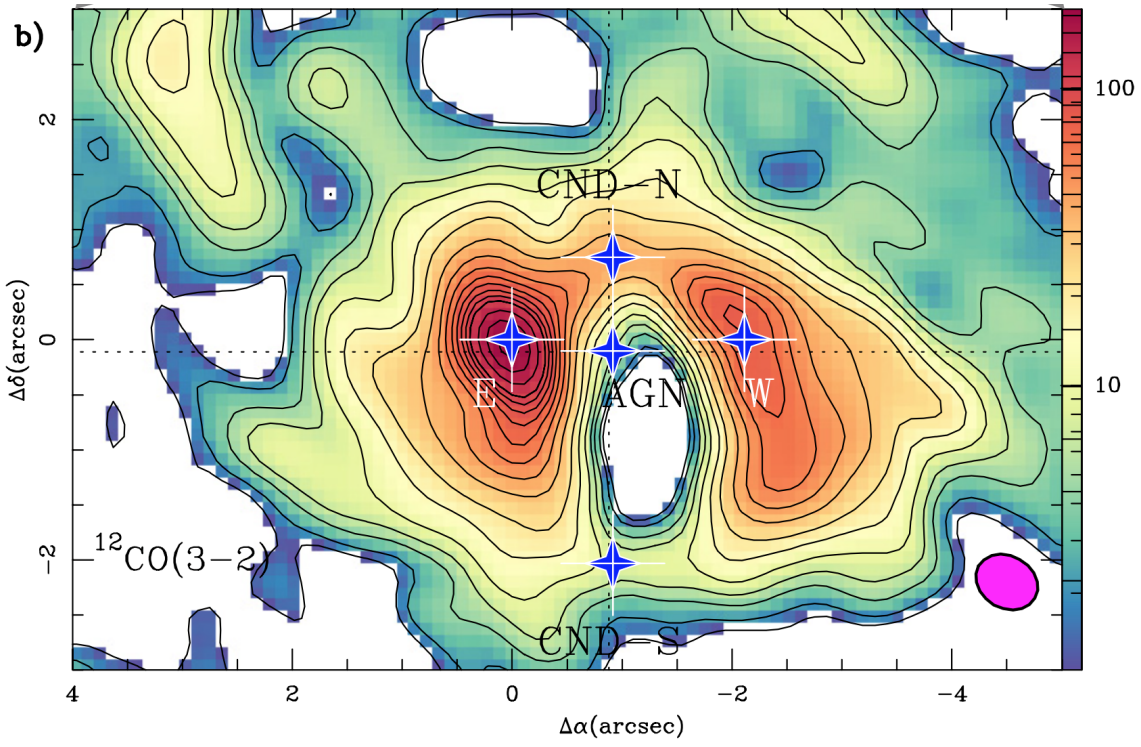

Figure 5.2: Map from Viti et al. (2014) and García-Burillo et al. (2014). $CO(3-2)$ velocity-integrated intensity map, measured in Jy/beam km s^{-1} over a 460 km s^{-1} window, obtained with ALMA. The beam size is shown in the bottom right hand corner. Locations of the regions analysed in the CND are labelled.

Table 5.2: Peak velocity for each line in each region of the CND in km s^{-1}

	$CO(3-2)$	$CO(6-5)$	$CS(7-6)$	$HCN(4-3)$	$HCO^+(4-3)$
AGN	-0.7 ± 1.1	-7.1 ± 6.1	-	-20.7 ± 4.3	-24.3 ± 3.7
East Knot	-54.7 ± 1.0	-50.6 ± 2.1	-59.4 ± 1.5	-49.3 ± 1.0	-46.6 ± 1.5
West Knot	53.1 ± 0.1	63.9 ± 0.4	55.1 ± 3.8	59.0 ± 0.8	61.7 ± 1.2
North CND	15.0 ± 1.4	19.4 ± 2.6	-	27.6 ± 1.2	25.6 ± 4.8
South CND	-117.5 ± 2.8	-171.8 ± 1.6	-	-133.2 ± 4.8	-100.7 ± 12.2

Table 5.3: FWHM for each line in each region of the CND in km s^{-1}

	$CO(3-2)$	$CO(6-5)$	$CS(7-6)$	$HCN(4-3)$	$HCO^+(4-3)$
AGN	107.1 ± 2.8	185.1 ± 15.1	-	173.5 ± 10.9	179.0 ± 9.0
East Knot	182.8 ± 2.9	178.6 ± 5.2	146.3 ± 3.7	194.1 ± 2.3	188.1 ± 3.5
West Knot	139.4 ± 0.3	120.3 ± 0.8	136.4 ± 9.4	128.8 ± 1.7	132.4 ± 3.0
North CND	169.1 ± 3.4	193.1 ± 5.9	-	175.4 ± 2.8	190.0 ± 12.0
South CND	127.6 ± 5.5	111.6 ± 22.3	-	153.2 ± 9.8	108.2 ± 38.0

A descriptive analysis of the line profiles in the CND

$CO(3-2)$ is detected in all regions. It is broadest in the East Knot, although RADEX simulations using CO ratios and multi-molecule modelling (Viti et al. 2014) indicate this region is the coolest. The region within the CND with the narrowest $CO(3-2)$ line is the AGN. The West and East Knots show almost symmetric profiles in the same lines. The peak of the East Knot spectrum is at $\sim$ -50 km s^{-1} with a prominent wing towards positive velocity. The West Knot spectrum peaks at $\sim$ 50 km s^{-1} with a wing in the opposite direction. Other detected transitions in these two regions show very similar profiles to those of $CO(3-2)$. In the north CND, the $CO(3-2)$ spectrum displays a wing towards the red. This is something that is not seen in any of the other detections in this region. The spectrum in the south CND is shifted bluewards to a point where part of the emission is unobserved. There is, however, a hint of an absorption feature. This is most prominent in $CO(3-2)$ but can be seen in $CO(6-5)$, $HCN(4-3)$ and $HCO^+(4-3)$ also. In $HCO^+(4-3)$, the profiles are largely similar to $CO(3-2)$. However, in the North and South CND, there is possibly evidence of a double peaked profile, something only displayed in $HCO^+(4-3)$ in these two regions.

In the AGN, there is a large difference in line width (80 km s^{-1}) between $CO(3-2)$ and $CO(6-5)$, as well as other transitions. The line profiles are also quite different. $CO(6-5)$ proves to be anomalous in more than one case. It is at a far extreme peak velocity in the the south CND, to an extent where nearly half the line width maybe unobserved. The

profiles in the East Knot appear to be all quite similar, as are profiles in the West Knot. Due to fairly weak detections of CS$(7-6)$, the only region it is possible to see its ratio (by velocity) with other transitions is the East Knot. There is very little difference from in CS$(7-6)$ ratios in this region. CS$(7-6)$ peaks at 100 km s^{-1} and declines by a factor of 2 away from this peak. The AGN shows a fairly constant HCO$^+(4-3)$ / HCN$(4-3)$ ratio. This is a similar pattern to all other regions. We now investigate in more detail each region of the CND.

AGN

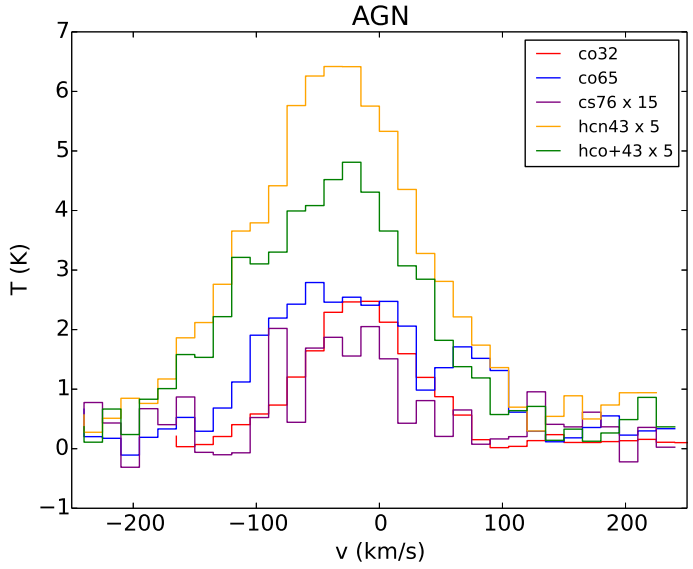

Figure 5.3: CO$(3-2)$, CO$(6-5)$, HCN$(4-3)$, HCO$^+(4-3)$ and CS$(7-6)$ spectra in the AGN. The label indicates the line observed, in some cases scaled up for ease of comparison. The scale factor is shown in the label next to the transition

The AGN spectra are displayed in Figure 5.3. Some lines have been scaled for better comparison. This is the case in many Figures in this Chapter. The amount the line is scaled by is displayed within the Figure and is absolute (i.e. a label of CS$(7-6)$ $\times$ 15 means the intensity in each velocity bin has been multiplied by 15). In order to more clearly display differentiation between different lines, we normalise the intensity of each line to its own peak intensity and then bin these intensities to 90 km s^{-1}. This is displayed for the AGN in Figure 5.4. The most notable thing about this plot is the difference between CO$(3-2)$ and CO$(6-5)$. In the wings of the line, at -100 km s^{-1}, CO$(6-5)$ is 2.5 stronger than CO$(3-2)$ and at +100 km s^{-1} it is 4 times stronger. The torus of gas rotating about the

AGN will be faster (v_{rot}) at smaller radii (r). Our results suggest therefore that the gas closer to the nucleus is more excited that at lower r. At first interpretation, there could be two possible reasons for this. Firstly, it could be due to illumination by the AGN. Or possibly it could be due to non-circular motions that we do not resolve.

It is also noticeable that at low and high velocities, $CS(7-6)$ is detected less strongly than $HCN(4-3)$ and $HCO^+(4-3)$. All three of these lines are associated with denser molecular gas. Therefore it is possible that there is some process or processes that is/are enhancing HCN and HCO^+ but not CS. HCN and HCO^+ have been observed to be enhanced in XDRs, explained by the abnormal chemistry that occurs (e.g. Krips et al. 2008). So far, there is little evidence to suggest that CS is enhanced in the same environment. In addition, Viti et al. (2014) find in their modelling of the CND, that CS is best fit by a shocked gas component. This suggests that illumination is the more likely cause of the increased excitation at small radii.

Meijerink and Spaans (2005) find in their XDR models that HCN/HCO^+ will only exceed unity in moderately dense gas where $N(H_2) < 10^{22.5}$ cm^{-2}. Due to the smaller range of ionisation rates in which HCN is enhanced under X-Rays (Lepp and Dalgarno 1996) and attenuation of the X-Ray flux at higher column densities, HCN/HCO^+ becomes <1 when $N(H_2) > 10^{22.5}$ cm^{-2}.García-Burillo et al. (2014) calculate the molecular hydrogen column density for the central r $\approx$ 20 pc to be $N(H_2) = 5 \times 10^{21}$ cm^{-2} using $CO(3-2)$. Although it is a crude approximation as CO is likely to be coming from a more extended gas component to HCN/HCO^+, we use this value as a rough comparison. We find that HCN/HCO^+ is quite constant across the whole line profile, although it is a little higher ($\approx$ 1.5) than the wings ($\approx$ 1.2) (see Figure 5.17, ratios are investigated further later in this chapter). This appears to be a somewhat confusing result. If indeed X-Ray illumination were responsible for the more excited emission at lower radii, we may expect HCN/HCO^+ to be >1 in the wings of the line (higher velocities, lower radii), and <1 in the line core (or at least lower than the value in the wings).

East Knot

The spectra and the normalised intensities, binned to 90 km s^{-1}, for the East Knot are displayed in Figure 5.5. Compared to the AGN, emission in all lines is much stronger. The East Knot is close to the major axis and the kinematics are driven by tangential/rotational motions of outflow that produce globally blueshifted profiles. This location displays the

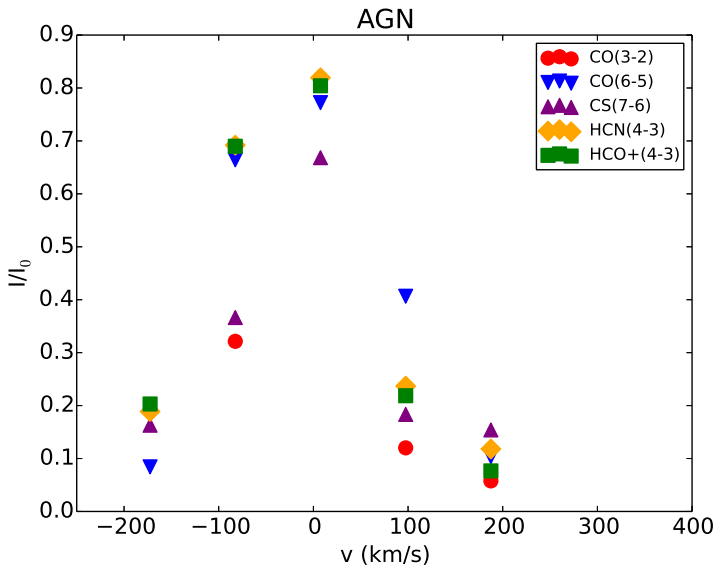

Figure 5.4: Normalised Intensity of $CO(3-2)$, $CO(6-5)$, $HCN(4-3)$, $HCO^+(4-3)$ and $CS(7-6)$ in the AGN, by 90 km s^{-1} velocity bins

strongest detections for all transitions. At its peak, CO is $\approx$ 20 times stronger in both lines, indicating a much greater quantity of molecular gas. $CS(7-6)$, is $\approx$ 10 stronger, indicating that although there is more dense gas than in the AGN, there is a lower ratio of dense gas to diffuse gas. The wings of the spectra appear to be quite uniform over all transitions. However the peaks of $HCN(4-3)$ and $HCO^+(4-3)$ are shifted by 5-15 km s^{-1} redwards of the CO peaks, and >15 km s^{-1} redwards of the $CS(7-6)$ peak. Looking at Figure 5.5, we confirm that the spectra are only significantly misaligned at low velocities. So HCN and HCO^+ are enhanced at low velocities compared to CO and CS but not at the high velocities of the outflow. It is unlikely this is due to variation in gas components of different densities, as in that case CS should be tracing the same as HCN and HCO^+. This could be due to an XDR component separate from the outflow. Figure 5.6 shows a chemical model for a warm (100 K), dense (10^4 cm $^{-3}$) gas component without a significant radiation field. We see that the differences in abundance do not correspond to what we observe. We also find that this is not well replicated with a shock model, as seen in Figure 5.7. From Chapter 4, we do see shocks in the East Knot. The chemical modelling may explain why we see such a strong CS line in the East Knot compared to other locations. A fast (60 km s^{-1}) shock significantly enhances CS but not the other observed species.

We take the ratio of $CO(6-5)/CO(3-2)$ at each velocity bin, displayed in Figure 5.16, at the end of this Chapter. We see that the $CO(6-5)/CO(3-2)$ ratio is flat across

the profile of the line. While this ratio is quite high (>1), the fact that it is not enhanced at velocities corresponding to the outflow suggests that the outflow at this location is inefficient at increasing excitation of CO lines. This indicates that the region is dominated by illumination and not by shocks in the outflow. This is particularly interesting as there are clearly shocks in the East Knot (see Chapter 4), but they may not play a significant role in the physics (and the chemistry) of the large scale molecular gas. This is consistent with the modelling of Viti et al. (2014), where only the CS emission is likely arising from the shocked gas.

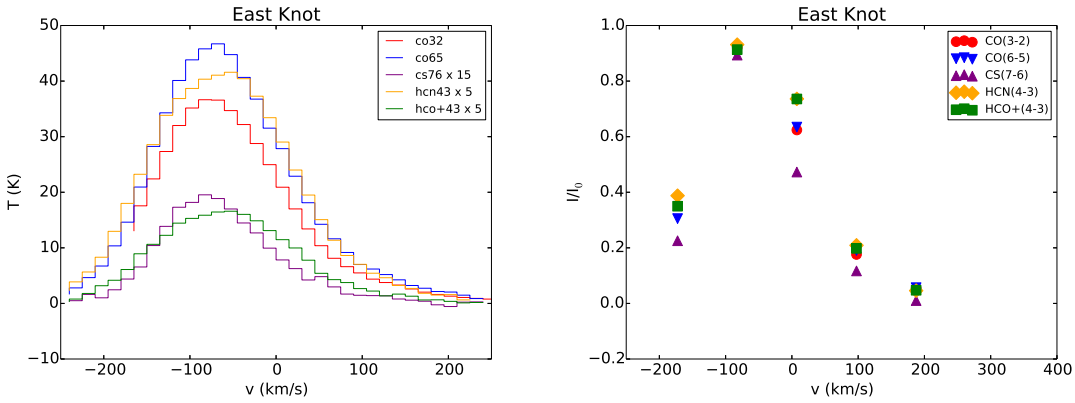

Figure 5.5: CO$(3-2)$, CO$(6-5)$, HCN$(4-3)$, HCO$^+(4-3)$ and CS$(7-6)$ spectra and normalised intensity in the East Knot

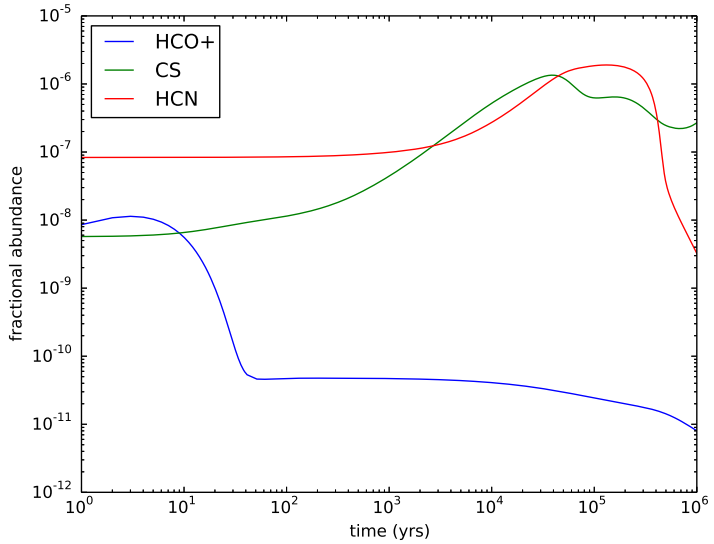

Figure 5.6: Chemical model in a warm (100 K), dense (10^4 cm $^{-3}$) gas component without a significant radiation field.

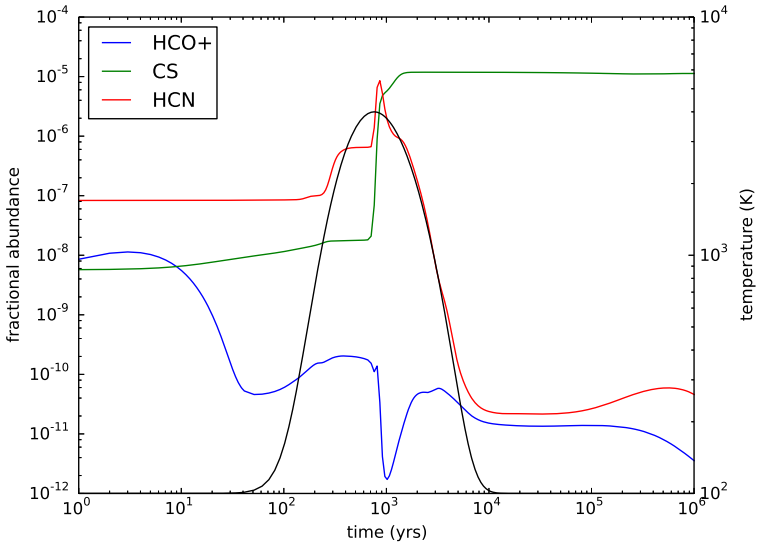

Figure 5.7: Chemical model including a shock at v = 60 km s^{-1}, with pre-shock density 10^4 cm $^{-3}$)

West Knot

The spectra and the normalised intensities, binned to 90 km s^{-1}, for the West Knot are displayed in Figure 5.8. The West Knot is close to the major axis and the kinematics are driven by tangential/rotational motions of outflow that produce globally redshifted profiles. Line profiles for all transitions are very similar. Relative to the East Knot, CO$(3-2)$ is enhanced compared to CO$(6-5)$. This however is only the case at velocities, v >50 km s^{-1}. This is best displayed in Figure 5.16. We see that while the East Knot CO$(6-5)$/CO$(3-2)$ ratio is quite flat, the West Knot is highly asymmetric. CO excitation actually decreases at the outflow velocities, v <50 km s^{-1}. This suggests that the outflow, or shocks in the outflow, are not responsible for excitation of the molecular gas in the West Knot either.

North CND

The North CND is close to the minor axis and the kinematics are driven by radial motions of outflow that produce globally slightly redshifted profiles. The spectra and the normalised intensities, binned to 90 km s^{-1}, for the North CND are displayed in Figure 5.9. The most notable outlier is CS$(7-6)$, but this is almost certainly due to a very weak marginal detection. It appears that CO$(3-2)$ is not as strong at the outflow velocity around 100 km s^{-1}. A better view of this is in Figure 5.16. We see that the

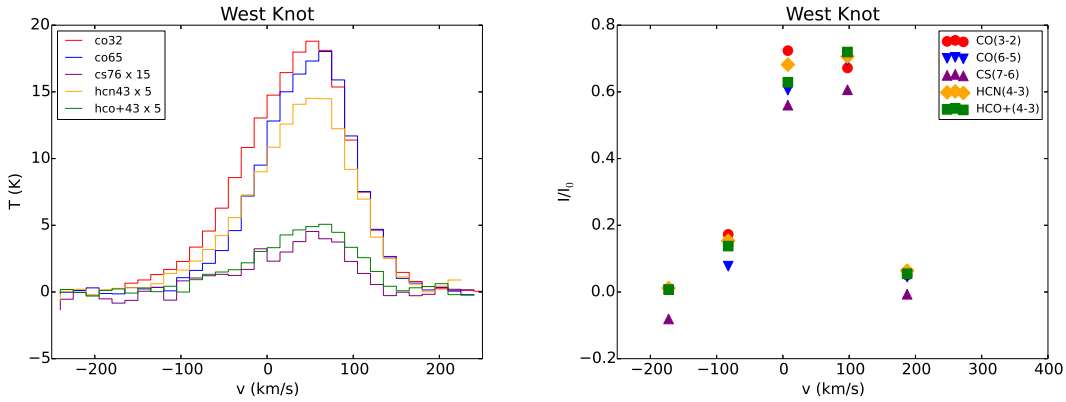

Figure 5.8: CO(3 – 2), CO(6 – 5), HCN(4 – 3), HCO^+(4 – 3) and CS(7 – 6) spectra and normalised intensity in the West Knot

CO(6 – 5)/CO(3 – 2) ratio does steadily increase from 0 to 100 km s^{-1}. However, at v >100 km s^{-1}, it then decreases. We may expect the initial increase to be due to shocks in the outflow, but there is no evidence for shocks occurring in the North CND (see Chapter 4). In addition, the drop off at extreme velocities suggests that something else is likely exciting the molecular gas.

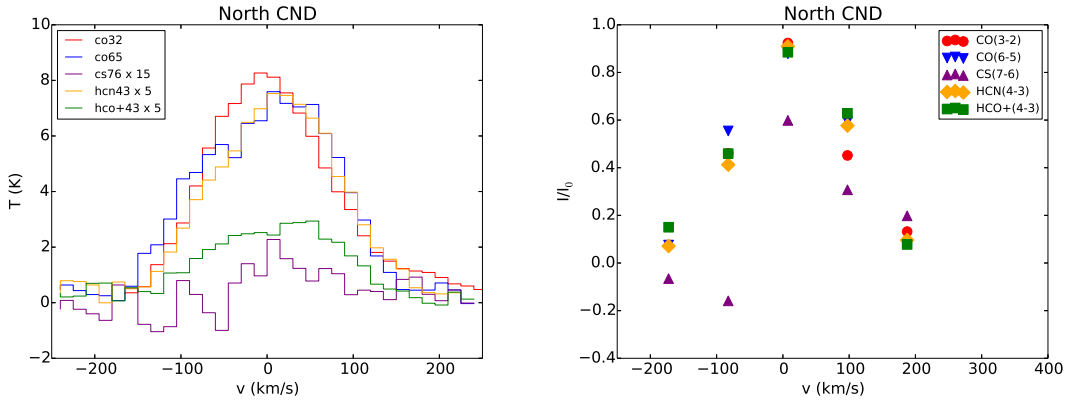

Figure 5.9: CO(3 – 2), CO(6 – 5), HCN(4 – 3), HCO^+(4 – 3) and CS(7 – 6) spectra and normalised intensity in the North CND

South CND

The South CND is close to the minor axis and the kinematics are driven by radial motions of the outflow that produce globally blueshifted profiles. The spectra and the normalised intensities, binned to 90 km s^{-1}, for the South CND are displayed in Figure 5.10. Each line appears to have two peaks, one at ≈ -100 km s^{-1} and a second at ≈ -200 km s^{-1}. Although we do not see this in CO(3 – 2) as coverage does not extend out far enough, there is the

slightest indication in the form of an increase in the furthest blue velocity bin that there would be one if our spectral range extended far enough. There is a slight sign of absorption at low velocities. There is almost no detection of CO(6 – 5) at ≈ -100 km s^{-1} but strong CO(3 – 2), indicating that CO is not excited until the extreme velocities of the outflow (<-150 km s^{-1}). At velocities faster than -100 km s^{-1} HCN(4−3) is significantly enhanced against HCO$^+$(4 – 3), something not seen in other CND locations. Martins et al. (2010) find evidence of a young stellar population in the South CND. Meijerink et al. (2007) find that the HCN/HCO$^+$ ratio is enhanced in PDRs (and sometimes in XDRs). It is possible that this enhancement is therefore due to to FUV/X-Ray illumination of the gas in the outflow.

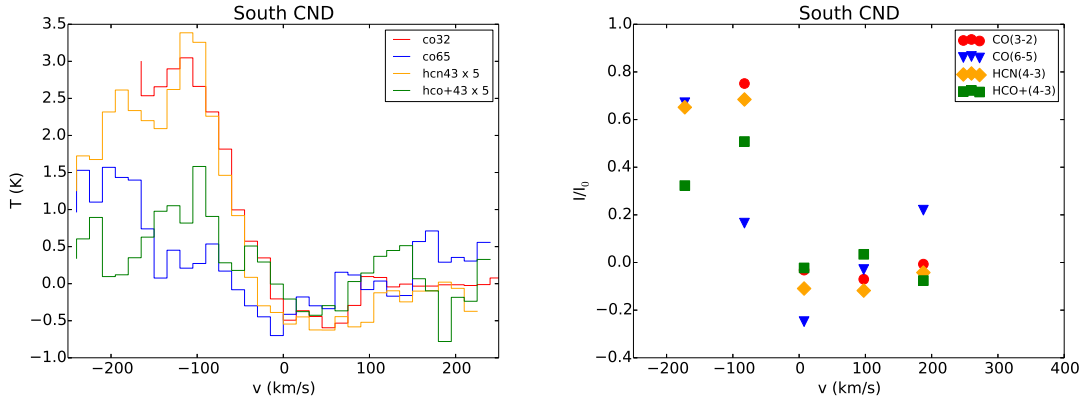

Figure 5.10: CO(3 – 2), CO(6 – 5), HCN(4 – 3) and HCO$^+$(4 – 3) spectra and normalised intensity in the South CND. CS(7 – 6) is undetected

5.2.2 SB Ring

Analysis of ALMA observations of SB Ring has so far been restricted to one star-forming clump in the southern part of the ring Viti et al. (2014). Here we complete an analysis of the line profiles across two star-forming clumps in the northern ring and six clumps (including the one previously analysed) in the southern ring. We base our decision on where to analyse on the strength of the CO(3 – 2) emission, as well as HST Paα emission and ALMA 349 GHz dust continuum emission (García-Burillo et al. 2014). CO(6 – 5) coverage does not extend to the SB Ring. The coordinates of each knot we observe are displayed in Table 5.4 and in Figure 5.11. We also tabulate the velocity at which each line peaks and FWHM of each line. This has been completed using GILDAS software, CLASS (Guilloteau and Lucas 2000). Peak velocities are displayed in Table 5.5 and FWHM in

Table 5.6.

Table 5.4: Coordinates of locations in the SB Ring

Location name	RA	Dec
North 1	02:42:40.133	-00:00:36.06
North 2	02:42:40.845	-00:00:33.02
South 1	02:42:39.845	-00:00:53.04
South 2	02:42:39.884	-00:00:54.95
South 3	02:42:40.070	-00:00:57.31
South 4	02:42:40.119	-00:00:58.70
SB Ring Original	02:42:40.317	-00:01:01.84
South 5	02:42:40.651	-00:01:00.90

Table 5.5: Peak velocity for each line in each region of the SB Ring in km s^{-1}

	Peak velocity			
Location name	$CO(3-2)$	$CS(7-6)$	$HCN(4-3)$	$HCO^+(4-3)$
North 1	40.4 ± 0.2	-12.5 ± 12.7	34.5 ± 4.7	41.7 ± 2.9
North 2	-45.4 ± 0.2	-	-37.7 ± 1.8	-42.6 ± 0.8
South 1	152.2 ± 0.2	152.6 ± 2.3	153.5 ± 0.5	153.4 ± 0.4
South 2	139.2 ± 0.2	145.8 ± 2.0	147.0 ± 0.8	145.6 ± 0.5
South 3	96.3 ± 0.1	-	96.6 ± 8.9	91.0 ± 5.2
South 4	104.2 ± 0.1	-	101.4 ± 3.8	100.3 ± 2.4
SB Ring original	49.6 ± 0.1	-	56.8 ± 1.1	58.4 ± 1.2
South 5	-17.8 ± 0.1	-	-13.0 ± 2.6	-9.0 ± 2.6

A descriptive analysis of the line profiles in the SB Ring

Peak line velocity goes from positive to negative in an anticlockwise direction. This is due to the rotation of the ring. Position South 3 and South 4 do not follow this pattern, and therefore must have some motion contrary to the large scale movement of the SB Ring. In terms of line width and peak velocity, the SB ring appears to follow the same pattern in $HCN(4-3)$ and $HCO^+(4-3)$ as it does in $CO(3-2)$. However, there are some notable differences. To the southwest, $HCN(4-3)$ and $HCO^+(4-3)$ are significantly narrower, but are broader in the north and southwest. Based on the peak velocities, they are largely moving in the same direction, at the same pace. Again points South 3 and South 4 differ, and the trend of decreasing velocity eastwards is reversed. These regions are close by (separation of $\sim$ 100 pc) indicating that in these regions there may be a secondary rotation component, about which these clumps are moving. We now investigate each region of the SB Ring more closely.

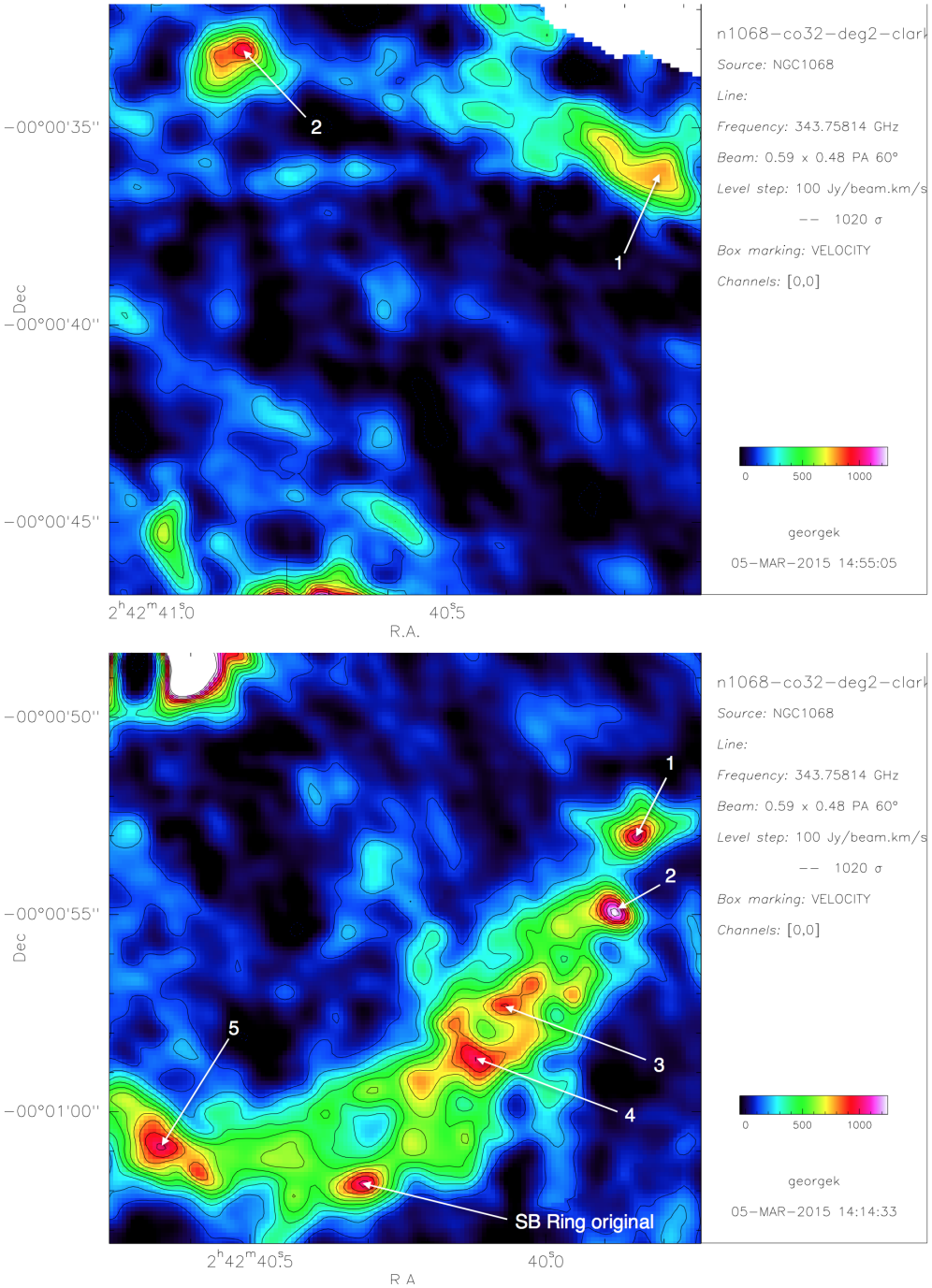

Figure 5.11: North SB ring (top) and south SB ring (bottom) in CO(3 – 2) with regions of interest annotated

Table 5.6: FWHM for each line in each region of the CND in km s^{-1}

	FWHM			
Location name	$CO(3-2)$	$CS(7-6)$	$HCN(4-3)$	$HCO^+(4-3)$
North 1	45.8 ± 0.4	126.5 ± 32.3	48.5 ± 11.0	45.9 ± 6.6
North 2	43.5 ± 0.4	-	61.4 ± 3.7	53.8 ± 1.7
South 1	39.8 ± 0.6	36.9 ± 5.8	41.8 ± 1.3	39.3 ± 1.0
South 2	53.7 ± 0.4	49.4 ± 5.4	49.8 ± 2.0	48.7 ± 1.2
South 3	57.4 ± 0.3	-	59.1 ± 12.0	52.4 ± 10.9
South 4	49.2 ± 0.3	-	57.6 ± 7.4	35.3 ± 4.8
SB Ring original	58.0 ± 0.2	-	43.8 ± 2.6	51.3 ± 3.0
South 5	57.1 ± 0.2	-	37.9 ± 5.5	45.9 ± 8.1

North SB Ring

Spectra and normalised intensity plots for the two locations in the North of the SB Ring are displayed in Figure 5.12. In North 1, $CS(7-6)$ is considerably offset in velocity from the other lines. It is over 50 km s^{-1} blueshifted relative to other transitions, which are located at approximately the the same velocities as one another. The $CS(7-6)$ is not strong but it is at a $\sim 3\sigma$ confidence level in terms of its peak intensity. However, there does not seem to be an overlap with $CO(3-2)$. Since CO should be tracing all molecular components of the gas, it may be that we are not actually detecting CS at all. The spectral feature that may be $CS(7-6)$ is ≈ 200 MHz offset from where the peak would be expected based on $CO(3-2)$. There is one molecule that has been observed in external galaxies that has a transition at this frequency. The methanol transition, $CH_3OH(5(-2,4)-4(1,3))$ is at 343.006 GHz (compared to $CS(7-6)$ at 342.883 GHz). This transition has an upper energy level, $E_u = 61$ K. However, it is highly unlikely to be responsible for the emission due to its very low dipole moment and the fact that we do not identify it in any other location. Therefore the most likely conclusion is that the apparent detection is just noise, despite the 3σ confidence level.

Notable in both locations is that $HCN(4-3)/HCO^+(4-3) < 1$. This contrasts all the CND locations. We discuss this further for the South SB Ring.

South SB ring

Spectra and normalised intensity plots for the six locations in the South of the SB Ring are displayed in Figure 5.13 and Figure 5.14, respectively. $CO(3-2)$ emission in each location has a relatively constant peak intensity of 15-20 K. However, $HCO^+(4-3)$ varies

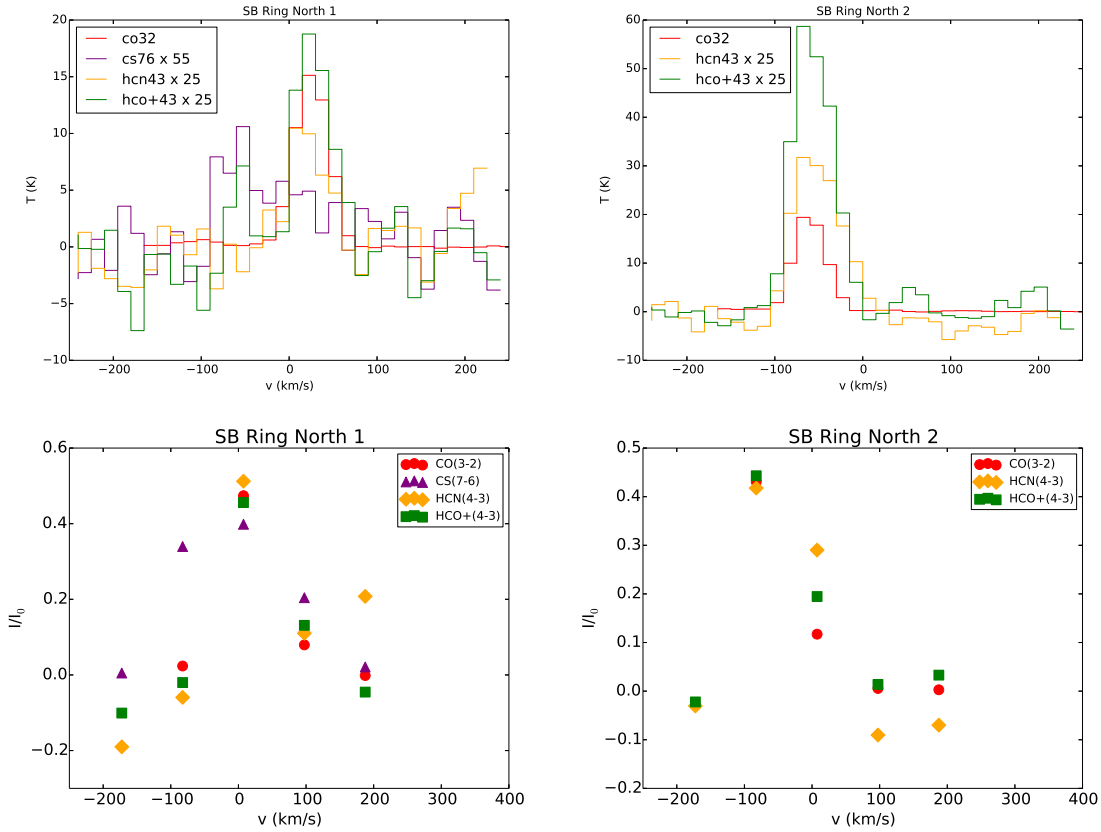

Figure 5.12: Top: Spectra for the two locations in the North SB Ring. In North 1 CO(3 − 2), HCN(4 − 3), $HCO^+(4-3)$ and CS(7 − 6) are detected. CS(7 − 6) is not detected in North 2. Bottom: Normalised intensity plots for the two locations in the North SB Ring

from 0.2 K (South 3) to 2.5 K (South 1). In addition, the ratio of $HCO^+(4-3)$/HCN(4−3) varies from ≈ 3 in South 1 down to 1 in South 3, 4 and 5. It is highly unlikely that the SB Ring is affected directly by the AGN outflow, given the distance between them (the SB Ring is at a radius of r ∼ 1-1.5 kpc (García-Burillo et al. 2014)). The most likely cause therefore is star formation. A simple chemical analysis may give us a better clue as to what environment(s) the observed emission is coming from. A possible cause for the varying emission is the presence of PDRs. Giant PDRs should be found in regions of galaxies with clusters of young massive stars, such as the clumps we observe here. Bayet et al. (2009b) completed a modelling with the aim of using different molecules to identify PDRs in external galaxies. They find that, in general, HCN is little affected by the FUV field produced by massive stars. HCO^+ is enhanced compared to non-PDR models. However, CS is dramatically reduced in abundance. Viti (2016) finds through chemical modelling that it is very difficult to achieve an $HCO^+(4-3)$/HCN(4 − 3) >1, without some form of

ionising radiation, whether UV or cosmic ray.

Prior to this work, Lintott et al. (2005) and Bayet et al. (2008b) completed a chemical modelling of hot core environments, particularly aimed at the non-Milky Way conditions likely found in external galaxies. A hot core is the dense, warm and relatively small gas surrounding a newly formed star. In contrast to a PDR, hot cores are associated with extremely high UV extinction, meaning that the FUV field does not have a significant effect on their chemistry. Bayet et al. (2008b) find that CS is significantly enhanced in hot cores. They also find that HCO^+ is detectable in hot cores only where the metallicity is low (0.1-1% solar). We do not know the metallicity of the environments we are observing. The metallicity of the CND as a whole has been found to be near solar (Aladro et al. 2013; Kamenetzky et al. 2011), but how much influence this may have on the SB Ring is unclear.

While it is important to stress the degeneracy that exists when trying to identify regions solely based on a chemistry, it is possible to draw some tentative conclusions from these findings. There are two regions in the South SB Ring where CS is either undetected (South 4), or only very marginally detected (South 3). In both these regions there is an HCN detection, indicating this is unlikely to be due to excitation effects as they both have similar critical densities and upper energy levels (when comparing $HCN(4-3)$ with $CS(7-6)$). These regions are nearby (~ 100 pc) and from the peak velocity of the detected emission, they could well be interacting. From the lack of CS and the detections of HCN and HCO^+, the most likely conclusion is that the major component in these regions is one or more PDRs. Possibly the entire region could be one giant PDR, given the apparent interactions, although this would have to be investigated further if we wish to draw a clearer conclusion.

The regions South 1 and South 2 both have clear detections of CS, HCN and HCO^+. HCO^+ is by far the strongest detection. These regions may therefore consist of a combination of hot core and PDR environments. It is unlikely that hot cores alone could produce this level of HCO^+ emission. The SB Ring position originally identified in García-Burillo et al. (2014); Viti et al. (2014), and position South 5, both have weak detections of CS and weak detections of HCN and HCO^+, compared to South 1 and South 2. This suggests that there must be a warm, shielded component to produce CS, and a PDR to produce HCO^+. However, both are likely to be on the scale of what is observed in South 1 and South 2.

Viti (2016) complete a large grid of chemical and RADEX models, showing the integrated intensities for both $HCO^+(4-3)$ and $HCN(4-3)$. Despite a large coverage of temperature, density and radiation field (both UV (χ) and cosmic ray (ζ)), there does not seem to be a model that fits the behaviour of HCO^+ and HCN in any of the SB Ring locations. HCN is almost always more intense than HCO^+ in the models. Where it isn't (primarily where either χ or ζ is very high), the integrated intensities of both lines are much lower than observed. This may mean that the two molecules are primarily being emitted from different gas components, which would make it very difficult to fit to a single model.

5.3 Line ratios

Here we analyse selected line ratios at observed locations in the CND. We do this both for a total velocity integrated ratio, and for how the ratio changes across the line profiles. Both are displayed in Figures 5.16 - 5.18 at the end of this Chapter. Below these ratios are discussed in more detail.

$HCN(4-3)/HCO^+(4-3)$

The HCN/HCO^+ ratio has in many papers (e.g. (Kohno et al. 2001; Krips et al. 2008; Davies et al. 2012) been suggested as a method for determining activity in the centre of a galaxy as either starburst (SB) or AGN. If the method can be proved reliable, it could be a very useful technique for detecting so-called "buried" AGN. These environments are opaque in UV and soft X-Rays, due to very high dust concentration. Therefore they can only be detected in the re-emitted IR, which is indistinguishable from emission from star formation, or in hard X-Rays (Fabian et al. 2002), which are difficult to observe. These give rise to X-Ray Dominated Regions (XDRs) surrounding AGN, in which HCN is apparently enhanced. The theory is therefore: a higher HCN/HCO^+ indicates an AGN, while a lower value indicates a SB.

Izumi et al. (2013) list HCN/HCO^+ values for five galaxies to show that this ratio in SB galaxies tends to be <1, and in AGN >1. Values in-between often lead to galaxies being classified as mixed AGN/SB (Imanishi et al. 2007). Izumi et al. (2013) give a value for NGC 1068 taken from Pérez-Beaupuits et al. (2009) of 3.7 ± 0.6. This is calculated from the same transitions as we observe, but is done so using single-dish data. Looking

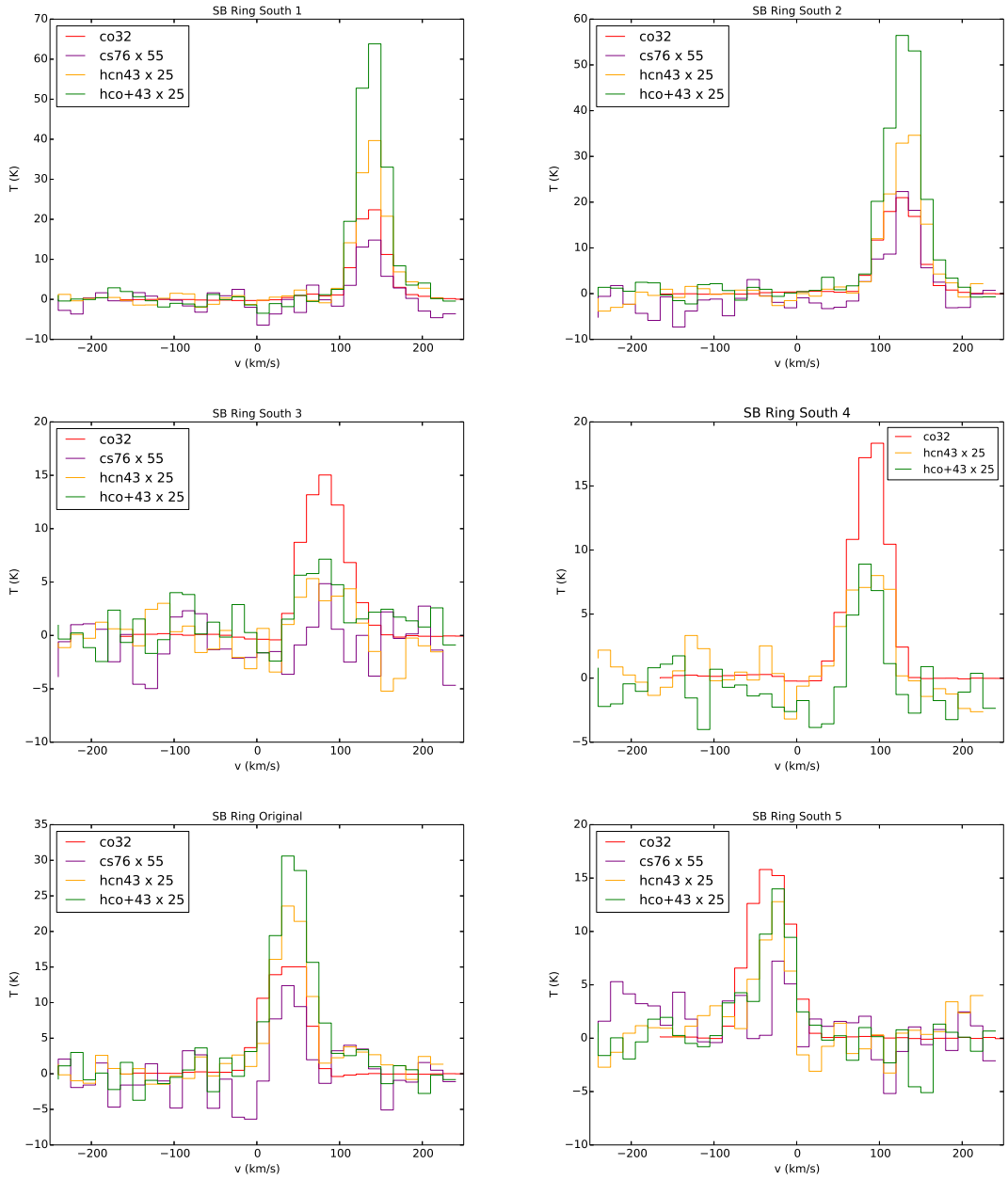

Figure 5.13: Spectra for the six locations in the South SB Ring. CO$(3-2)$, HCN$(4-3)$, HCO$^+(4-3)$ are detected in all locations. CS$(7-6)$ is not detected in some locations; if not detected it is not displayed.

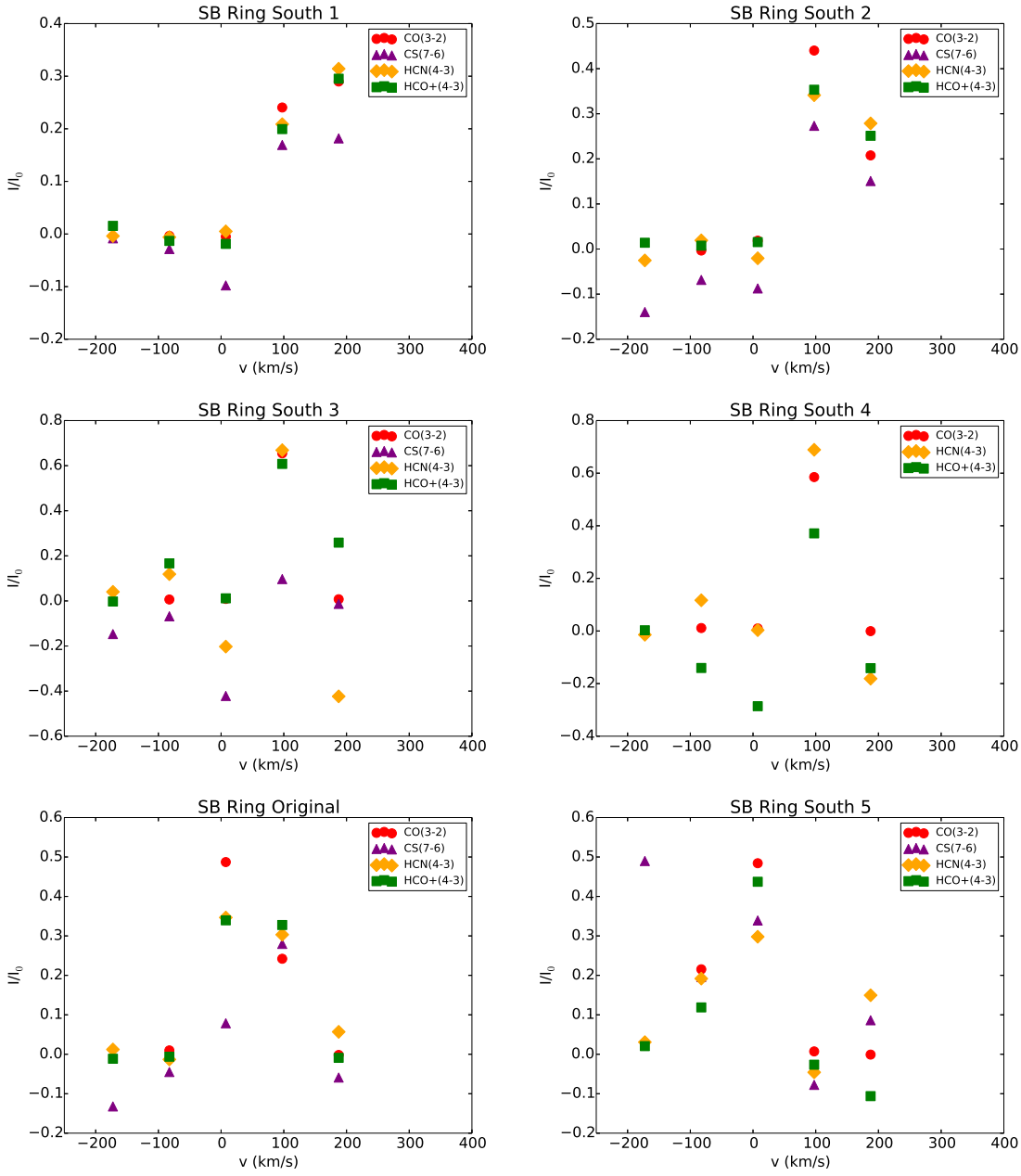

Figure 5.14: Normalised intensity plots for the six locations in the South SB Ring. Where CS($7-6$) is not detected it is not displayed.

at Figure 5.17, we calculate this ratio at 1.3 ± 0.1 for the AGN. The difference almost certainly arises as the beam size for the single dish observations covers a much larger region that we observe. We find that the HCN/HCO^+ value for the regions in the CND is always ∼2.5. The SB ring location is 1.2 ± 0.9. At best this only semi-correlates with the hypothesis that HCN/HCO^+ is a tracer of AGN or SB activity. The value for the AGN is similar to that of NGC 253, a typical SB galaxy (1.1 ± 0.3, Izumi et al. 2013). Using ALMA observations, Izumi et al. (2015) find a value of 1.1 ± 0.06 in the nucleus of the Seyfert I galaxy, NGC 7469. This galaxy also displays a clear CND surrounding its AGN. At several locations in the CND of NGC 7496, the HCN$(4-3)$/$HCO^+(4-3)$ ratio is ∼ 0.5. Unlike NGC 1068, NGC 7496 does not have a significant outflow. It is possible that the outflow, or interaction between the outflow and molecular clouds in the CND, is causing increased emission in HCN (or decreased emission in HCO^+). This could be through increased abundance via chemical means, and/or enhanced excitation due to the gas conditions. Chemically, Meijerink et al. (2007) show that the same HCN/HCO^+ abundance ratio can be achieved in a high density ($n(H_2) > 10^5$ cm^{-3}), lower energy region as is possible in a lower density XDR. In addition, abundance ratio may not be the same as the observed value. HCN has roughly an order of magnitude higher critical density than HCO^+ for the same transition J+1→J. In high density environments, such as is observed in the CND of NGC 1068 (Viti et al. 2014), we would expect HCN emission to be enhanced compared to HCO^+. These complexities make the HCN/HCO^+ ratio an unreliable method for distinguishing AGN from SB. It could be an initial indicator of a *possible* AGN, but should not be used alone as a diagnostic tool. Very tentatively, the ratio could be used as an indicator of outflow interaction around *known* AGN, if indeed this is what is responsible for the increased value. This is a hypothesis that needs to be further investigated in other galaxies before drawing any serious conclusions. Viti (2016) finds that this ratio in particular is subject to significant degeneracies during modelling. Most likely, the same complexities that lead to its lack of reliability as a SB/AGN diagnostic would cause similar issues here.

Observing the trend as it changes with velocity, it is generally flat for all CND locations. Although there is some marginal trend toward lower ratios at velocities of outflow in East Knot and West Knot. It is unclear what would cause this however, and in terms of the global ratio, it would have little effect. The value is also quite constant in the AGN, with a slight dip at central velocities and at very extreme velocities. Most of this is accounted

for by the error bars.

HCN$(4-3)$**/CS**$(7-6)$

Izumi et al. (2013) suggest that the HCN/CS ratio could also be used as a tracer of AGN or SB activity. They also use the HCN$(4-3)$/CS$(7-6)$ ratio. At face value, this could resolve one of the issues of using HCN$(4-3)$/HCO$^+(4-3)$. HCN$(4-3)$ and CS$(7-6)$ have very similar critical densities. At 100 K, $n_{crit}(HCN43) \approx 7 \times 10^6$ cm^{-3} and $n_{crit}(CS76)$ $\approx 8 \times 10^6$ cm^{-3}. However, what we observe (shown in Figure 5.18) does not improve very much upon using HCN/HCO$^+$. Values in the AGN and in the surrounding CND do not appear to vary by very much. Izumi et al. (2013) produce a plot (their Figure 11) of HCN$(4-3)$/CS$(7-6)$ against HCN$(4-3)$/HCO$^+(4-3)$. They plot five galaxies: two Seyferts (including NGC 1068 from single dish data), two SBs, and NGC 4418, which is described as containing many unusual features and a buried AGN (Spoon et al. 2001). The plot shows that the two AGN are enhanced in both ratios by a factor of up to 8 compared to the two SB galaxies. NGC 4418 is not enhanced in either ratio. We produce the same plot here (Figure 5.15) to show how the ratios vary between regions/environments. We see no correlation. The reason for this could well be chemical. We study the ratios by velocity to get a better picture of what is going on.

The trend of ratio by velocity is similar in all CND locations and the SB Ring, but at the East Knot the trend is towards lower ratios at high red velocities of outflow. CS$(7-6)$ and HCN$(4-3)$ have similar critical densities, so something else must be causing the difference. That could be either non-collisional excitation or chemical abundance-driven. Could it be possible that less CS is produced in the outflow than we thought? We find in Chapter 4 that powerful shocks are almost certainly occurring in the East Knot. In Chapter 3 (and in Kelly et al. 2015), we find that it is possible for CS to be enhanced during shock events, primarily due to the raised temperature of the gas. So it seems unlikely that CS would be significantly depleted and therefore more likely that HCN is enhanced, or there is radiative excitation occurring that favours HCN$(4-3)$ over CS$(7-6)$. It should also be noted that the error bars at the high velocities are quite large.

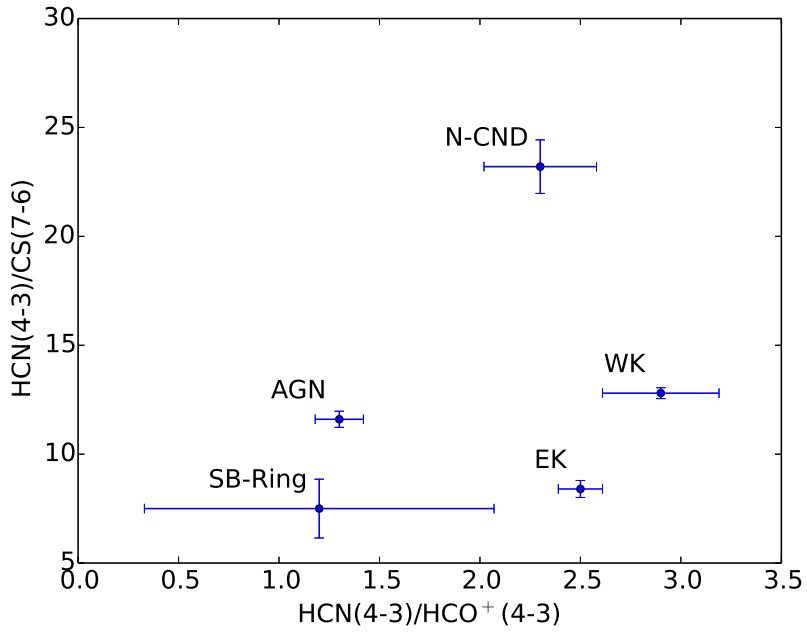

Figure 5.15: HCN (J = 4-3) to HCO^+ (J = 4-3) and HCN (J = 4-3) to CS (J = 7-6) integrated intensity ratios of each region we observe in brightness temperature scale. While previous papers have suggestion a high ratio of either of these line could be due to an AGN, the apparent non-correlation shown here does not support that theory.

5.4 AGN Feedback in NGC 1068

The role of the outflow in NGC 1068 is important as it can serve to regulate activity in the central region of the galaxy. The outflow has a rate of dM/dt $\sim 63^{+21}_{-37}$ $M_\odot \mathrm{yr}^{-1}$ (García-Burillo et al. 2014), which could serve to quench star formation in the CND. The interaction between the ISM and the photons in the outflow is identified in the $\mathrm{CO}(6-5)/\mathrm{CO}(3-2)$ ratio, which is significantly higher in the AGN location than in the other CND locations (García-Burillo et al. 2014). In addition to the AGN location, we found in Chapter 4 that it is clear the outflow in NGC 1068 is shocking the ISM in the East Knot and likely in the West Knot. In addition, X-Ray illumination is affecting all our observed CND locations, and is likely dominating in the North and South CND. Understanding this interaction is central to the understanding of how the outflow mediates the co-evolution of the super massive black hole (SMBH) and the rest of the galaxy. The SMBH at the centre of NGC 1068 is approximately 10^7 $M_\odot$ and is accreting close to its Eddington limit (Kishimoto 1999). In terms of galaxy evolution, NGC 1068 sits in the so-called "green valley" of the colour-magnitude diagram. This is the space between the two major galaxy populations: the red sequence containing mostly elliptical galaxies; and the blue cloud where spirals

are generally found. The green valley has been described as the transition between the star forming blue galaxies and the quenched red ellipticals (Faber et al. 2007). There is a large clustering of AGN in this region, where star formation across the galaxy as a whole has been recently quenched (Salim et al. 2007). Recent research suggests that this period of transition is very different for galaxies that contain an AGN. They pass through this period much more quickly as the balance between outflow and inflow of gas is disrupted and star formation uses up the remaining gas reservoir (Schawinski et al. 2014).

NGC 1068 has an intense starburst at its centre, which contributes most of its star formation rate of $\sim 5\ M_{\odot}\mathrm{yr}^{-1}$ (Smith and Wilson 2003). The shock interactions between outflow and ISM we detect in Chapter 4 occurs out to a distance from the AGN of up to $\sim$ 160 pc. They also do not occur at all regions surrounding the AGN, despite the radial effects of the outflow and the clear detection of ISM molecular gas at the North and South CND (where no shocks are detected either in SiO, HNCO or CS). This indicates that different processes of AGN feedback are dominating different regions of the CND. Winds/shocks are dominant in the East and West Knots, and X-Ray radiation dominates in the South and North CND.

The radial molecular outflow has its semi-major axis running approximately east-west, with the semi-minor axis running north-south. This is traced by CO$(3-2)$, which correlates strongly with Paα emission and radio continuum emission at 22 GHz (García-Burillo et al. 2014). These trace the AGN ionised nebulosity and radio jet plasma respectively. We see a strong correlation between the peak of the CO$(3-2)$ emission and the peak of the other molecular lines discussed in this Chapter. There is also some correlation between SiO$(3-2)$ and CO$(3-2)$ as seen in Figure 4.4, particularly in the East Knot. This suggests that AGN Feedback is affecting both the moderately dense gas and the densest components traced by CS, HCN and HCO^{+}. This correlates with the interstellar molecular gas in the CND is being efficiently pushed outwards via the nuclear wind, and not through other means. If this outflow of molecular gas is not balanced sufficiently by an inflow, circumnuclear star formation in NGC 1068 could be swiftly quenched. Further study of any potential gas inflow would be required to determine more exactly how AGN feedback is affecting NGC 1068.

From Müller-Sánchez et al. (2011), the outflow appears to accelerate out to a distance of $\sim$80 pc, where it reaches a turnover point and subsequently decelerates. This is also seen in other Seyferts with an outflow (NGC 3783 and NGC 7469), but not in all. This

distance is where we see the peak emission in most tracers, including shock tracers from Chapter 4, which helps back up this result since wind/shock interactions with the ISM should serve to decelerate the outflow. It has been suggested that the outflow extends to up to 1 kpc from the AGN (Evans et al. 2010). In Section 5.2.2, we state that detections of CS in regions of the SB Ring are likely due to star formation/hot cores. It could be argued that since we identify CS as tracer of shocks in the CND, its detection in the SB Ring may be due to an interaction between outflow and ISM. This is, however, quite unlikely since in the observations in Chapter 4 of SiO and HNCO detected neither in any region of the SB Ring. This does not completely rule out interaction at this distance, but suggests that it does not dominate.

5.5 Conclusions

We have used observations of several molecular lines to investigate chemical and physical differentiation between regions of NGC 1068. We do this by observing line profile variation within specific regions and line variation between these regions. In the CND, we find that in the AGN, more highly excited CO closer to the AGN, and a lack of CS emission, suggests that the gas is most likely in an XDR environment, illuminated by the AGN. In the East Knot, we find that despite heavy shocks, the region is mostly dominated by the XDR powered by the AGN. We find the same in the West Knot, where shocks have also been identified. Shocks tracers are not observed in the North or South CND. The chemistry in these regions is almost certainly driven predominantly by the XDR. Between the regions, we find that CS is not observed in the South or North CND. It is observed however in the East and West Knot. In the East Knot in particular, is offset from HCO^+ and HCN, confirming the modelling of Viti et al. (2014), who find that CS is emitted from the shocked region while HCO^+ and HCN arise from unshocked regions with high ionisation rates. In all regions of the CND HCN is more intense that HCO^+. In the SB Ring we see some regions where HCO^+ is more intense that HCN. The AGN is not likely to have a large effect on the SB Ring, due to its distance. We attribute the enhanced HCO^+ to the the likely presence of PDRs. This is compounded by the fact that we do not detect CS in many of these regions. CS has been shown to be dramatically reduced in the presence of a high FUV field. Where we do observe CS in the SB Ring, we determine there must be some shielded gas components, possibly hot cores, where CS emission arises from.

We speculate that two nearby clumps in the southern SB Ring may be part of one giant PDR, due to lack of CS emission, enhanced HCO^+ emission, and an apparent interaction between the two.

We also investigate line ratios in the CND regions and at a representative point in the SB Ring. A high HCN/HCO^+ ratio has been used to identify AGN in several papers. We find that this ratio is, however, unreliable as it varies seemingly at random across the CND and is in fact lowest in the AGN (other than the SB Ring). We also investigate the HCN/CS ratio used in conjunction with HCN/HCO^+ to distinguish AGN from SB. Again, we find that this ratio does not seem to follow a pattern and of the CND locations, it is lowest in the AGN. We conclude that line ratios alone are not reliable diagnostics and it may be better to examine line profiles individually.

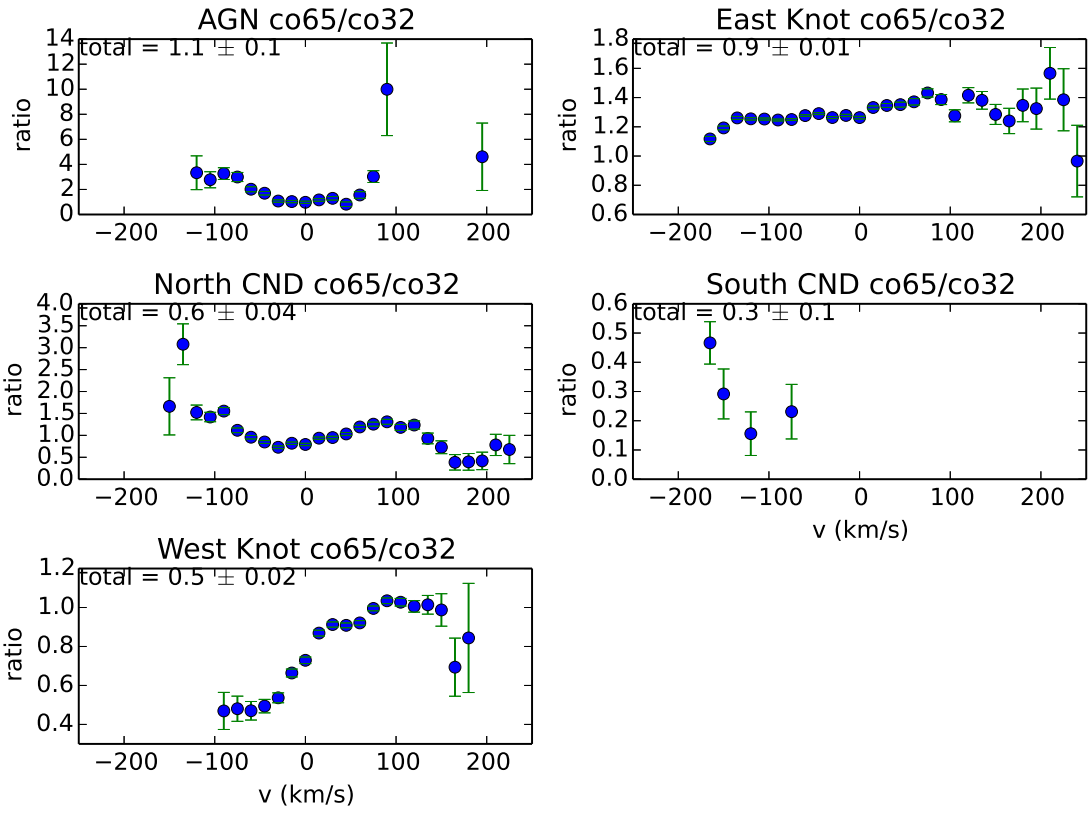

Figure 5.16: $CO(6-5)/CO(3-2)$ ratio by 15 km s^{-1} velocity bin

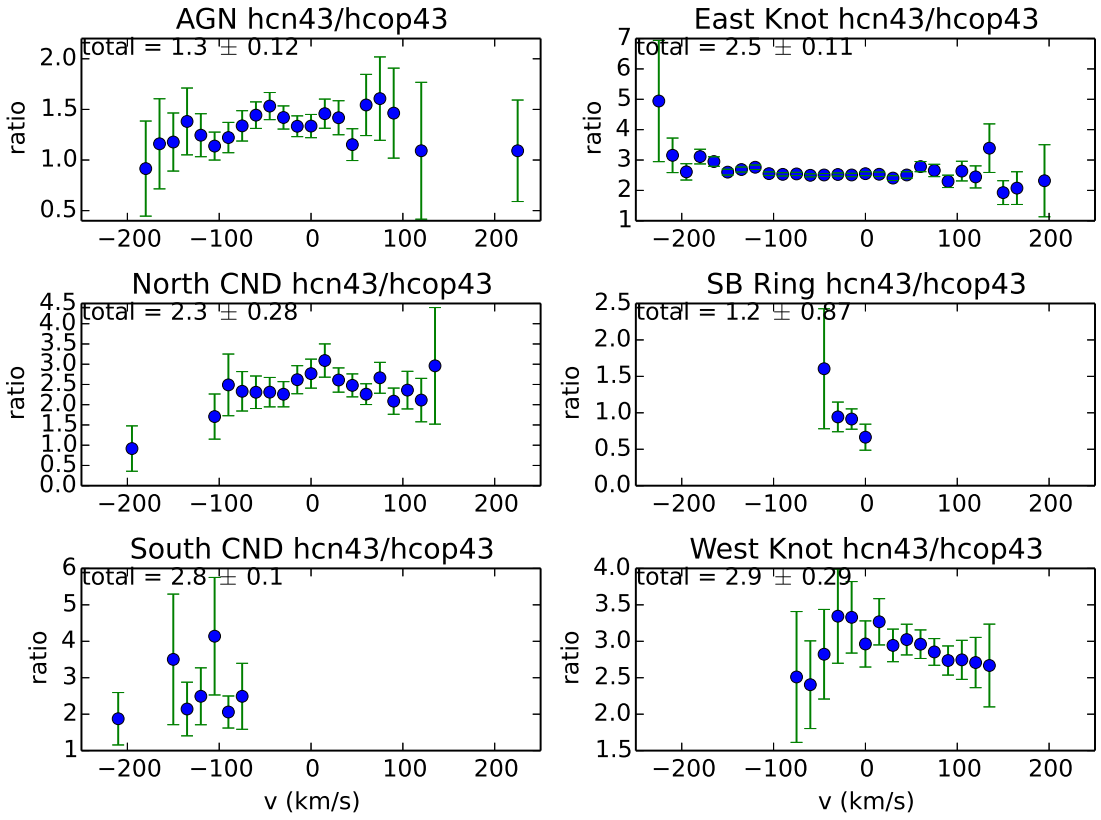

Figure 5.17: HCN$(4-3)$/HCO$^+(4-3)$ ratio by 15 km s^{-1} velocity bin

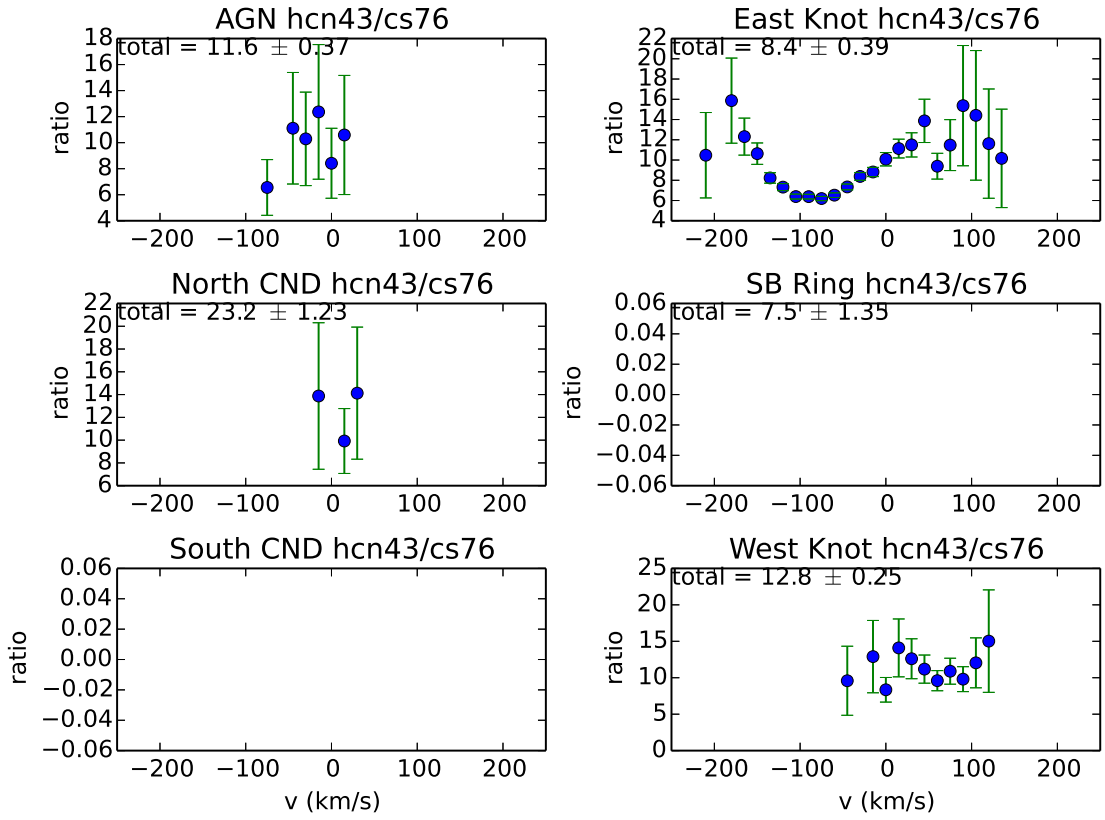

Figure 5.18: HCN$(4-3)$/CS$(7-6)$ ratio by 15 km s^{-1} velocity bin

This page was intentionally left blank

Chapter 6

Concluding Remarks and Future Work

In this thesis, we have used observations of molecular rotational lines to uncover the properties of some of the most extreme regions of nearby galaxies. We have done this by both direct analysis of the observations, and by utilising chemical and radiative transfer models. By using complementary observations of different molecules, we traced different components of the molecular gas. We studied the star forming dense cores of starburst galaxies traced by CS, the shocks produced from an AGN powered outflow as traced by SiO and HNCO, and the variation between regions of an AGN-starburst galaxy using several molecular tracers.

In Chapter 2, we presented observations of the dense gas tracer CS in two nearby starburst galaxies. The central regions of NGC 6946 and NGC 3079 were mapped in CS($J = 2 - 1$) and CS($J = 3 - 2$). We identified a double-horn line profile in the central pointing of both galaxies and conclude that this could be due to the rotation of gas, or possible self-absorption. LTE calculations were made using the observational data we tabulate. Using complementary observations of methanol, we determined the lower limit to the kinetic temperature in NGC 6946 to be 14 K. Using this value as a guide, we derived LTE column densities for each pointing using our CS observations and found values between N(CS) = 3×10^{12} cm^{-2} and N(CS) = 2×10^{14} cm^{-2} in NGC 6946 and values between N(CS) = 5×10^{12} cm^{-2} and N(CS) = 1×10^{14} cm^{-2} in NGC 3079.

The work in Chapter 2 was developed further in Chapter 3. We linked a time and depth dependent chemical model with a molecular line radiative transfer model and used the observations in Chapter 2 to guide our inputs. We reproduced the observations, showing how the conditions in the dense, potentially star forming gas are likely to vary away from the galactic centres. We also estimated the quantity of this gas. We find that, for both target galaxies, emission of CS from warm (T = 100 - 400 K), dense ($n(H_2) = 10^{5-6}$ cm^{-3}) cores, possibly with a high cosmic ray ionisation rate ($\zeta = 10\,\zeta_0$) best describes conditions for our central pointing. In NGC 6946, conditions are generally cooler and/or less dense further from the centre, whereas in NGC 3079, conditions are more uniform. The inclusion of shocks allowed for more efficient CS formation, which means that an order of magnitude less dense gas is required to replicate observations in some cases. We estimated that the dense gas as traced by CS, makes up a total of 2.5%-25% of the molecular gas reservoir by mass.

The limitations of the work in Chapter 2 and Chapter 3 were mostly dependent of the lack of spatial resolution achieved with a single dish telescope. In addition, we lacked the high-J transitions of CS that trace the densest components of the gas. The use of interferometric observations over a wide range of frequencies would make it possible truly quantify the star forming gas and determine its distribution across the nucleus of the galaxy. However, NGC 6946 and NGC 3079 are not positioned to be easily observable with the most advanced submillimeter interferometer, ALMA. Given this limitation, a proposal has been submitted to observe the similar galaxy NGC 4303, a Seyfert II spiral barred starburst galaxy. If successful, these observations, which will encompass the nucleus, the bar and part of the spiral arms, will allow us to study the distribution of the dense gas as traced by CS at scales down to $\sim$ 35 pc spatial resolution (the scale of GMCs). We will also be able to determine the gradient of densities and temperature across the bar and partially along the spiral arms and determine whether and where the dense gas has been shocked.

In Chapter 4, we compared the distribution of two shock tracers, SiO and HNCO, in the CND of NGC 1068. We performed LTE and RADEX analyses to determine the column densities and physical characteristics of the gas emitting these two species. We then used a chemical model to determine the origin of the emission.We found there was strong SiO peak to the East of the AGN, with weak detections to the West. This distribution contrasted that of HNCO, which was detected more strongly to the West. We saw that

SiO emission peak in the East is similar to the peak of the molecular gas mass traced by CO, whereas HNCO emission is offset from this peak by as much as ∼80 pc (∼1″). We compared velocity integrated line ratios in the East and West. We confirmed that SiO emission strongly dominates in the East, while the reverse is true in the West. We used RADEX to analyse the possible gas conditions that could produce such emission. We found that, in both East and West, we could not constrain a single temperature for the gas. We ran a grid of chemical models of potential shock processes in the CND and found that SiO is significantly enhanced during a fast (60 km s^{-1}) shock but not during a slow (20 km s^{-1}) shock, nor in a gas not subjected to shocks at all. We found the inverse for HNCO, whose abundance increases during slow shocks and in warm non-shocked gas. High SiO and low HNCO indicated a fast shock, while high HNCO and low SiO indicated either a slow shock or warm, dense, non-shocked gas. The East Knot is therefore likely to contain gas that is heavily shocked. From chemical modelling, we found that gas in the West Knot may be non-shocked, or may be undergoing a much milder shock event. When we took into account RADEX results, we saw that the milder shock event is the more likely of the two scenarios.

In Chapter 5, we used ALMA data of NGC 1068 to analyse spectra of five transitions, CO(3 − 2), CO(6 − 5), CS(7 − 6), HCN(4 − 3) and HCO^+(4 − 3). This was completed for different regions of the galaxy: the AGN, four locations in the CND where emission is particularly strong, and eight locations in a SB ring at a radius of ∼ 1.3 kpc from the AGN. We saw that CO is more highly excited closer to the AGN, suggesting that the AGN is illuminating the molecular gas surrounding it. We did not detect CS in the AGN. Since CS does not form efficiently in the presence of X-Rays, we found the most likely solution to be that the region is a large X-Ray Dominated Region (XDR), illuminated by the AGN. In the East Knot, we found the shocks identified in Chapter 4 are not responsible for the bulk of the chemistry in the region, and in fact illumination from the AGN is probably dominant. We strongly detected CS, suggesting it is probably tracing another gas component into the region, most likely the shocked gas. Similar conclusions are reached for the gas to the West Knot. To the North and South CND, where no shocks are detected, XDR chemistry dominates and no CS is detected, providing further evidence and building on the findings of Chapter 3 that CS is enhanced in shocked regions. In the SB Ring we saw some regions where HCO^+ is more intense that HCN. This is unusual and does not fit well to models. We find that HCO^+ is enhanced due to PDRs and that HCN

is probably not emitting strongly in them. It is likely from another gas component. As is the CS, which we find likely to be tracing hot cores, the region surrounding newly formed stars. In addition, found that using solely the molecular ratios, $HCN(4-3)/HCO^{+}(4-3)$ and $HCN(4-3)/CS(7-6)$, is not always an accurate way to identify AGN activity, as has been suggested in many previous papers.

We find that signatures of AGN feedback correlate well with the tracers of the molecular outflow in NGC 1068. While the outflow in the East and West Knots are likely wind driven, the North and South CND regions are dominated by radiation. The question of whether the outflow is affecting the SB Ring is still open, but the lack of detection of even weak shock tracers suggest that maybe it is not interacting strongly. In addition, the chemistry as a whole in regions of the SB Ring is different to that of any of the CND regions. $HCO^{+}(4-3)$ is stronger in the SB Ring compared to all other species. We note that this alone cannot rule out potential large scale effects of AGN feedback on the SB Ring.

Future work on NGC 1068 focuses on obtaining ALMA mapping of several CS transitions. We confirmed that CS is tracing the shock components of the CND, where other molecules were not. To further characterise the shock components many transitions of CS are required. Using the models and techniques similar to those used in Chapter 3, it will be possible to produce a full CS transition J-ladder which can then be compared to observations. This should be complemented by observations of several SiO transitions, for which a similar modelling can be completed.

Appendix A

Appendix A

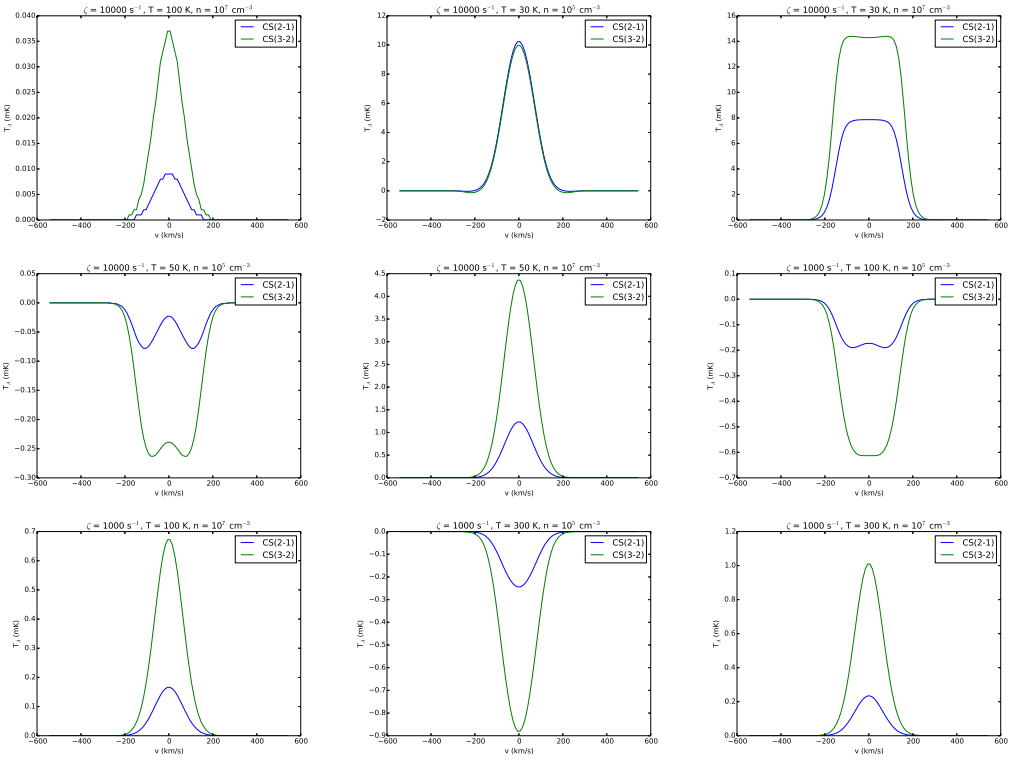

Figure A.1: Additional outputs from SMMOL radiative transfer modelling

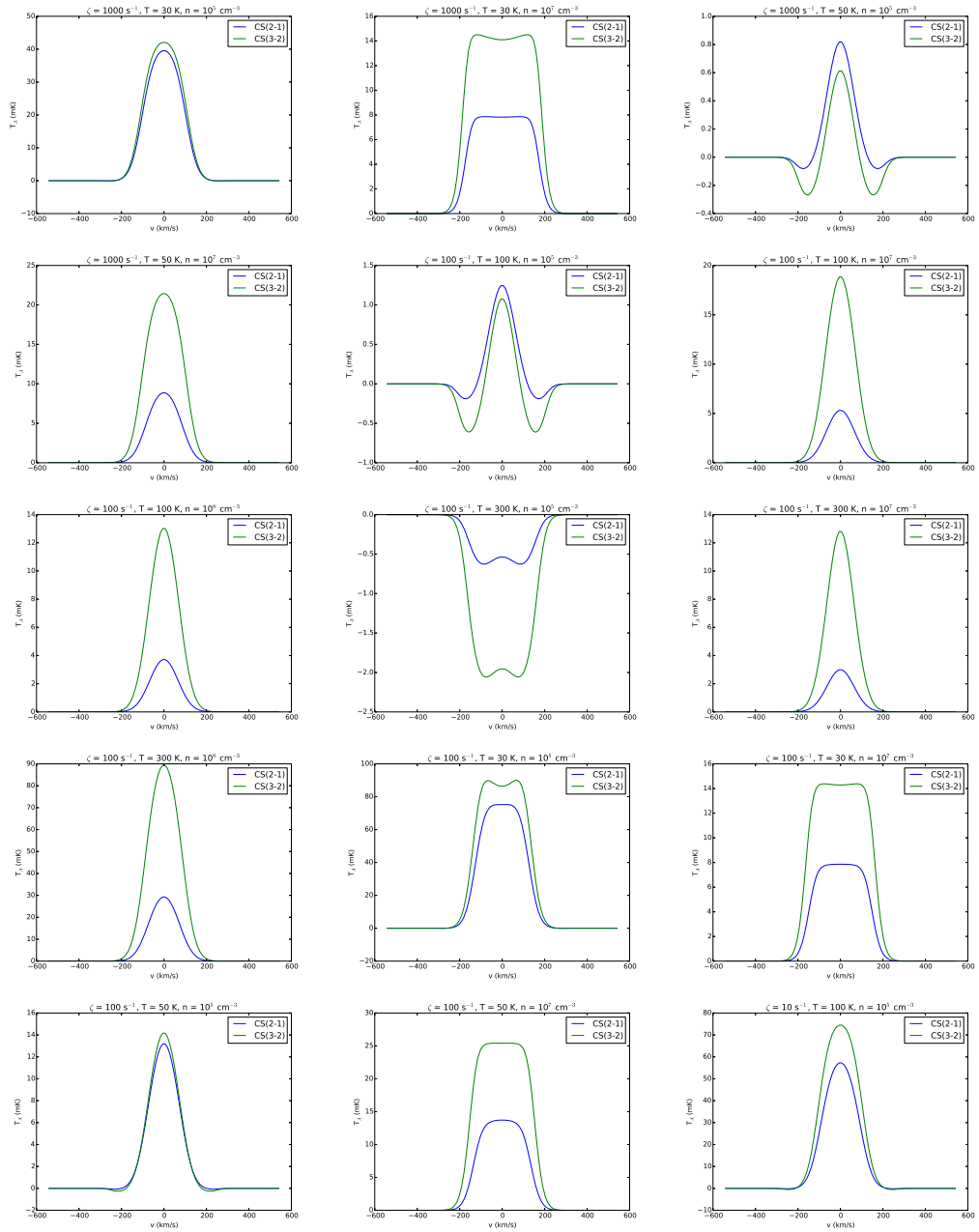

Figure A.2: Additional outputs from SMMOL radiative transfer modelling

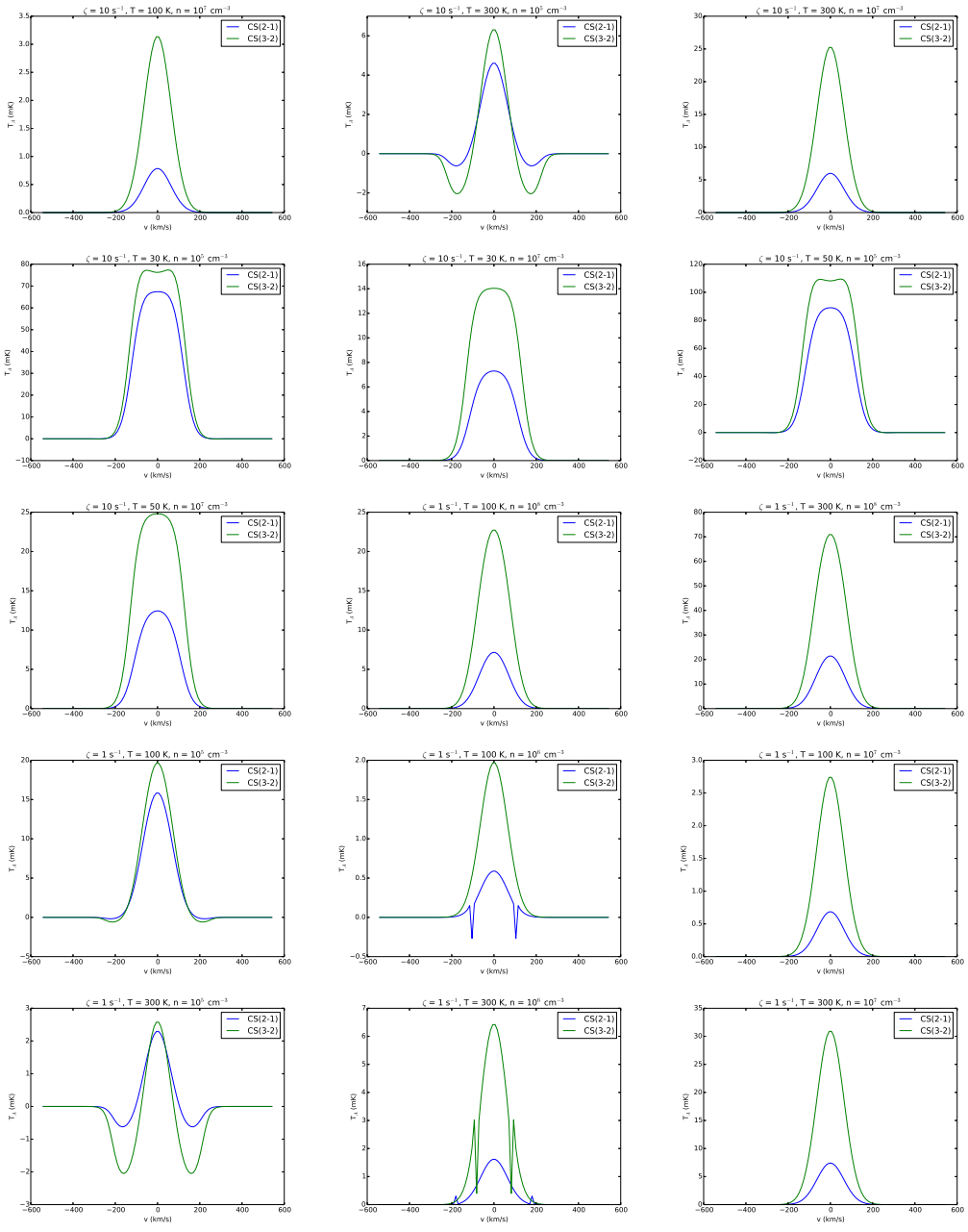

Figure A.3: Additional outputs from SMMOL radiative transfer modelling

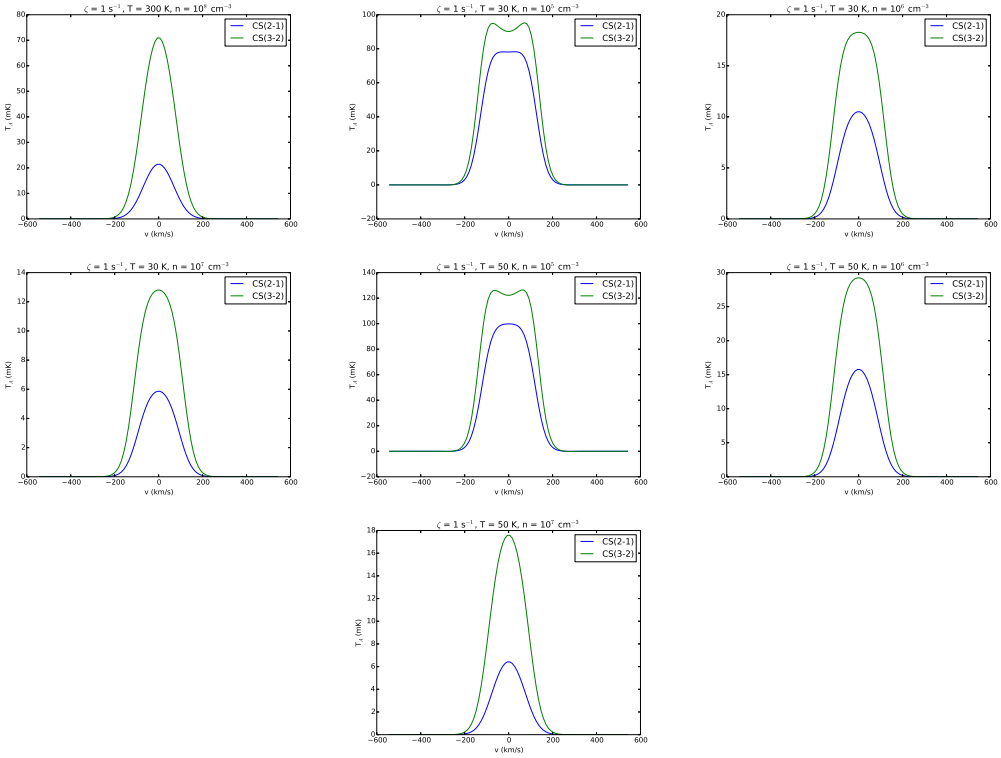

Figure A.4: Additional outputs from SMMOL radiative transfer modelling

Appendix B

Appendix B

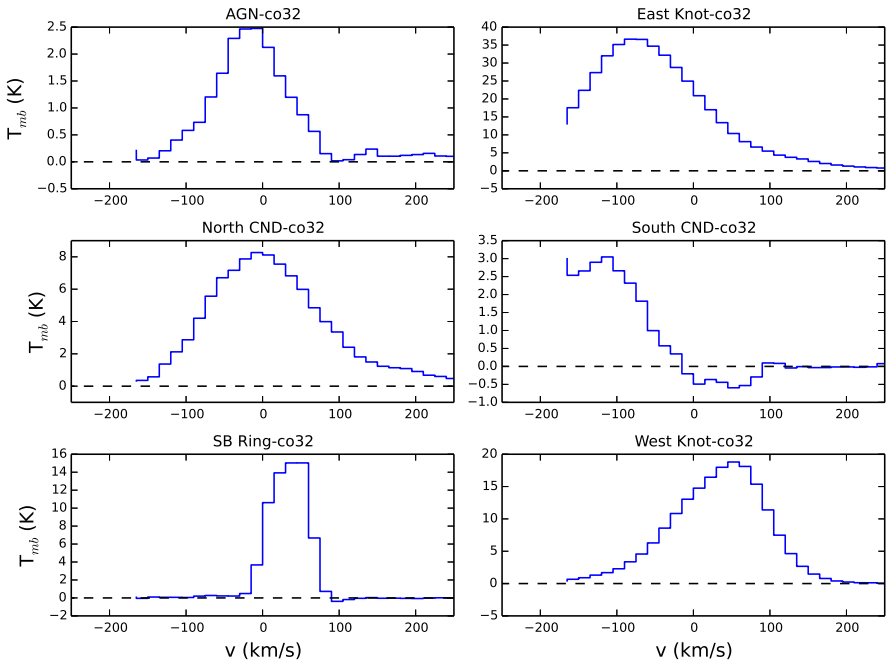

Figure B.1: CO(3 − 2) emission in the five CND subregions and in a single SB ring location

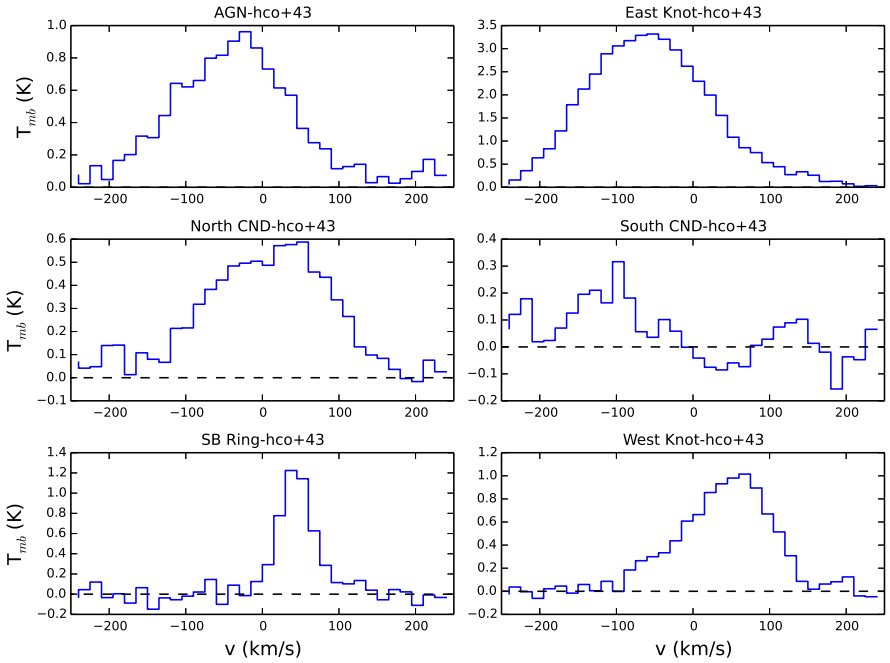

Figure B.2: $HCO^+(3-2)$ emission in the five CND subregions and in a single SB ring location

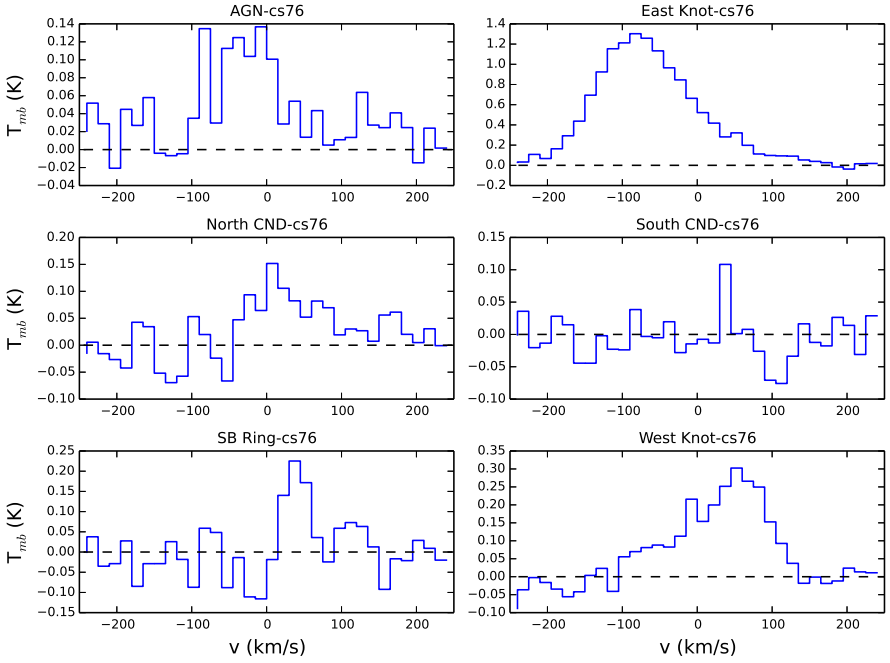

Figure B.3: $CS(7-6)$ emission in the five CND subregions and in a single SB ring location

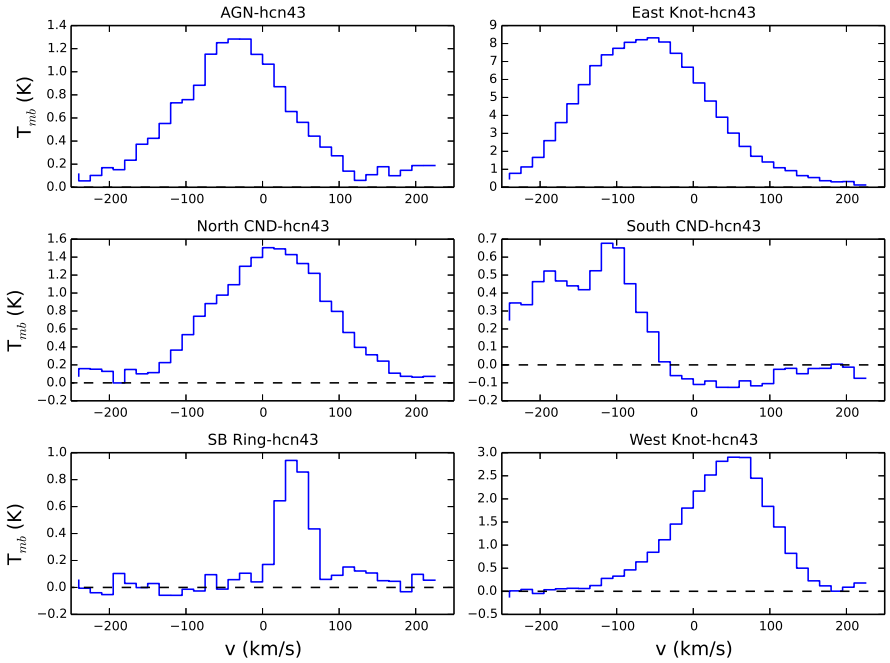

Figure B.4: HCN(4 – 3) emission in the five CND subregions and in a single SB ring location

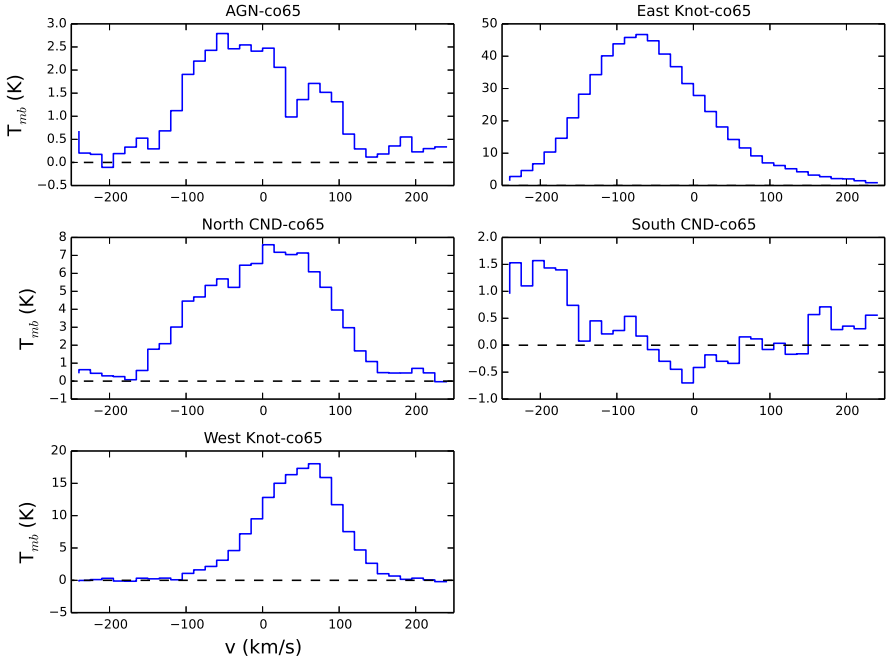

Figure B.5: CO(6 – 5) emission in the five CND subregions

This page was intentionally left blank

Bibliography

R. Aladro, S. Martín, J. Martín-Pintado, R. Mauersberger, C. Henkel, B. Ocaña Flaquer, and M. A. Amo-Baladrón. A $\lambda = 1.3$ mm and 2 mm molecular line survey towards M 82. *A&A*, 535:A84, Nov. 2011a. doi: 10.1051/0004-6361/201117397.

R. Aladro, J. Martín-Pintado, S. Martín, R. Mauersberger, and E. Bayet. CS, HC_3N, and CH_3CCH multi-line analyses toward starburst galaxies. The evolution of cloud structures in the central regions of galaxies. *A&A*, 525:A89, Jan. 2011b. doi: 10.1051/0004-6361/201014090.

R. Aladro, S. Viti, E. Bayet, D. Riquelme, S. Martín, R. Mauersberger, J. Martín-Pintado, M. A. Requena-Torres, C. Kramer, and A. Weiß. A $\lambda = 3$ mm molecular line survey of NGC 1068. Chemical signatures of an AGN environment. *A&A*, 549:A39, Jan. 2013. doi: 10.1051/0004-6361/201220131.

E. Anders and N. Grevesse. Abundances of the elements - Meteoritic and solar. *Geochimica et Cosmochimica Acta*, 53:197–214, Jan. 1989. doi: 10.1016/0016-7037(89)90286-X.

R. Antonucci. Unified models for active galactic nuclei and quasars. *Ann. Rev. Astr. Astrophys.*, 31:473–521, 1993. doi: 10.1146/annurev.aa.31.090193.002353.

L. Armus, V. Charmandaris, J. Bernard-Salas, H. W. W. Spoon, J. A. Marshall, S. J. U. Higdon, V. Desai, H. I. Teplitz, L. Hao, D. Devost, B. R. Brandl, Y. Wu, G. C. Sloan, B. T. Soifer, J. R. Houck, and T. L. Herter. Observations of Ultraluminous Infrared Galaxies with the Infrared Spectrograph on the Spitzer Space Telescope. II. The IRAS Bright Galaxy Sample. *ApJ*, 656:148–167, Feb. 2007. doi: 10.1086/510107.

S. Aronowitz and S. Chang. Adsorption and recombination of hydrogen atoms on a model graphite surface. *ApJ*, 293:243–250, June 1985. doi: 10.1086/163230.

W. A. Baan and J. A. Irwin. The Nuclear Structure of NGC 3079. *ApJ*, 446:602, June 1995. doi: 10.1086/175820.

R. Ball, A. I. Sargent, N. Z. Scoville, K. Y. Lo, and S. L. Scott. The molecular bar and star formation in the nucleus of NGC 6946. *ApJ L*, 298:L21–L25, Nov. 1985. doi: 10.1086/184559.

A. J. Battisti and M. H. Heyer. The Dense Gas Mass Fraction of Molecular Clouds in the Milky Way. *ApJ*, 780:173, Jan. 2014. doi: 10.1088/0004-637X/780/2/173.

E. Bayet, C. Lintott, S. Viti, J. Martín-Pintado, S. Martín, D. A. Williams, and J. M. C. Rawlings. Tracing High-Density Gas in M82 and NGC 4038. *ApJ L*, 685:L35–L38, Sept. 2008a. doi: 10.1086/592399.

E. Bayet, S. Viti, D. A. Williams, and J. M. C. Rawlings. Molecular Tracers of High-Mass Star Formation in External Galaxies. *ApJ*, 676:978–990, Apr. 2008b. doi: 10.1086/528678.

E. Bayet, R. Aladro, S. Martín, S. Viti, and J. Martín-Pintado. Extragalactic CS Survey. *ApJ*, 707:126–136, Dec. 2009a. doi: 10.1088/0004-637X/707/1/126.

E. Bayet, S. Viti, D. A. Williams, J. M. C. Rawlings, and T. Bell. Molecular Tracers of Pdr-Dominated Galaxies. *ApJ*, 696:1466–1477, May 2009b. doi: 10.1088/0004-637X/696/2/1466.

E. Bayet, J. Yates, and S. Viti. CS Line Profiles in Hot Cores. *ApJ*, 728:114, Feb. 2011. doi: 10.1088/0004-637X/728/2/114.

V. Beckmann and C. R. Shrader. *Active Galactic Nuclei*. Aug. 2012.

K. Bekki. Formation of blue compact dwarf galaxies from merging and interacting gas-rich dwarfs. *MNRAS*, 388:L10–L14, July 2008. doi: 10.1111/j.1745-3933.2008.00489.x.

M. Benedettini, J. A. Yates, S. Viti, and C. Codella. A detailed modelling of the chemically rich clumps along the CB3 outflow. *MNRAS*, 370:229–238, July 2006. doi: 10.1111/j.1365-2966.2006.10473.x.

E. A. Bergin and W. D. Langer. Chemical Evolution in Preprotostellar and Protostellar Cores. *ApJ*, 486:316, Sept. 1997. doi: 10.1086/304510.

J. Bland-Hawthorn, J. F. Gallimore, L. J. Tacconi, E. Brinks, S. A. Baum, R. R. J. Antonucci, and G. N. Cecil. The Ringberg Standards for NGC 1068. *Ap&SS*, 248:9–19, Feb. 1997. doi: 10.1023/A:1000567831370.

A. D. Bolatto, M. Wolfire, and A. K. Leroy. The CO-to-H_2 Conversion Factor. *Ann. Rev. Astr. Astrophys.*, 51:207–268, Aug. 2013. doi: 10.1146/annurev-astro-082812-140944.

A. Boselli, J. Lequeux, and G. Gavazzi. Molecular gas in normal late-type galaxies. *A&A*, 384:33–47, Mar. 2002. doi: 10.1051/0004-6361:20011747.

L. Bronfman, L.-A. Nyman, and J. May. A CS(2-1) survey of IRAS point sources with color characteristics of ultra-compact HII regions. *A&A*, 115:81, Jan. 1996.

P. D. Brown, S. B. Charnley, and T. J. Millar. A model of the chemistry in hot molecular cores. *MNRAS*, 231:409–417, Mar. 1988. doi: 10.1093/mnras/231.2.409.

C. Carignan, P. Charbonneau, F. Boulanger, and F. Viallefond. Observational study of the spiral galaxy NGC 6946. II - H I kinematics and mass distribution. *A&A*, 234:43–52, Aug. 1990.

A. Cattaneo, S. M. Faber, J. Binney, A. Dekel, J. Kormendy, R. Mushotzky, A. Babul, P. N. Best, M. Brüggen, A. C. Fabian, C. S. Frenk, A. Khalatyan, H. Netzer, A. Mahdavi, J. Silk, M. Steinmetz, and L. Wisotzki. The role of black holes in galaxy formation and evolution. *Nature*, 460:213–219, July 2009. doi: 10.1038/nature08135.

C. J. Chen. . *Leiden University*, page xx, 2011.

M. P. Collings, M. A. Anderson, R. Chen, J. W. Dever, S. Viti, D. A. Williams, and M. R. S. McCoustra. A laboratory survey of the thermal desorption of astrophysically relevant molecules. *MNRAS*, 354:1133–1140, Nov. 2004. doi: 10.1111/j.1365-2966.2004.08272.x.

F. Costagliola, S. Aalto, M. I. Rodriguez, S. Muller, H. W. W. Spoon, S. Martín, M. A. Peréz-Torres, A. Alberdi, J. E. Lindberg, F. Batejat, E. Jütte, P. van der Werf, and F. Lahuis. Molecules as tracers of galaxy evolution: an EMIR survey. I. Presentation of the data and first results. *A&A*, 528:A30, Apr. 2011. doi: 10.1051/0004-6361/201015628.

A. C. Crook, J. P. Huchra, N. Martimbeau, K. L. Masters, T. Jarrett, and L. M. Macri.

Groups of Galaxies in the Two Micron All Sky Redshift Survey. *ApJ*, 655:790–813, Feb. 2007. doi: 10.1086/510201.

L. P. Crosthwaite and J. L. Turner. CO(1-0), CO(2-1), and Neutral Gas in NGC 6946: Molecular Gas in a Late-Type, Gas-Rich, Spiral Galaxy. *AJ*, 134:1827–1842, Nov. 2007. doi: 10.1086/521645.

E. Daddi, F. Bournaud, F. Walter, H. Dannerbauer, C. L. Carilli, M. Dickinson, D. Elbaz, G. E. Morrison, D. Riechers, M. Onodera, F. Salmi, M. Krips, and D. Stern. Very High Gas Fractions and Extended Gas Reservoirs in z = 1.5 Disk Galaxies. *ApJ*, 713:686–707, Apr. 2010. doi: 10.1088/0004-637X/713/1/686.

A. Das, K. Acharyya, S. Chakrabarti, and S. K. Chakrabarti. Formation of water and methanol in star forming molecular clouds. *A&A*, 486:209–220, July 2008. doi: 10.1051/0004-6361:20078422.

R. Davies, D. Mark, and A. Sternberg. Dense molecular gas around AGN: HCN/CO in NGC 3227. *A&A*, 537:A133, Jan. 2012. doi: 10.1051/0004-6361/201117647.

J. D. Destree, T. P. Snow, and J. H. Black. An Ultraviolet Search for Interstellar CS. *ApJ*, 693:804–811, Mar. 2009. doi: 10.1088/0004-637X/693/1/804.

R. Diehl, H. Halloin, K. Kretschmer, G. G. Lichti, V. Schönfelder, A. W. Strong, A. von Kienlin, W. Wang, P. Jean, J. Knödlseder, J.-P. Roques, G. Weidenspointner, S. Schanne, D. H. Hartmann, C. Winkler, and C. Wunderer. Radioactive ^{26}Al from massive stars in the Galaxy. *Nature*, 439:45–47, Jan. 2006. doi: 10.1038/nature04364.

S. D. Doty, F. L. Schöier, and E. F. van Dishoeck. Physical-chemical modeling of the low-mass protostar IRAS 16293-2422. *A&A*, 418:1021–1034, May 2004. doi: 10.1051/0004-6361:20034476.

B. T. Draine. Photoelectric heating of interstellar gas. *ApJSS*, 36:595–619, Apr. 1978. doi: 10.1086/190513.

B. T. Draine, W. G. Roberge, and A. Dalgarno. Magnetohydrodynamic shock waves in molecular clouds. *ApJ*, 264:485–507, Jan. 1983. doi: 10.1086/160617.

K. Drdla, G. R. Knapp, and E. F. van Dishoeck. The CS molecule in diffuse interstellar clouds. *ApJ*, 345:815–827, Oct. 1989. doi: 10.1086/167953.

P.-A. Duc, E. Brinks, J. E. Wink, and I. F. Mirabel. Gas segregation in the interacting system ARP 105. *A&A*, 326:537–553, Oct. 1997.

W. W. Duley and D. A. Williams. *Interstellar chemistry.* 1984.

C. W. Engelbracht, M. J. Rieke, G. H. Rieke, and W. B. Latter. Observations and Modeling of the Nuclear Starburst in NGC 6946. *ApJ*, 467:227, Aug. 1996. doi: 10.1086/177598.

D. A. Evans, P. M. Ogle, H. L. Marshall, M. A. Nowak, S. Bianchi, M. Guainazzi, A. L. Longinotti, D. Dewey, N. S. Schulz, M. S. Noble, J. Houck, and C. R. Canizares. Searching for AGN Outflows: Spatially Resolved Chandra HETG Spectroscopy of the NLR Ionization Cone in NGC 1068. In L. Maraschi, G. Ghisellini, R. Della Ceca, and F. Tavecchio, editors, *Accretion and Ejection in AGN: a Global View*, volume 427 of *Astronomical Society of the Pacific Conference Series*, page 97, Oct. 2010.

S. M. Faber, C. N. A. Willmer, C. Wolf, D. C. Koo, B. J. Weiner, J. A. Newman, M. Im, A. L. Coil, C. Conroy, M. C. Cooper, M. Davis, D. P. Finkbeiner, B. F. Gerke, K. Gebhardt, E. J. Groth, P. Guhathakurta, J. Harker, N. Kaiser, S. Kassin, M. Kleinheinrich, N. P. Konidaris, R. G. Kron, L. Lin, G. Luppino, D. S. Madgwick, K. Meisenheimer, K. G. Noeske, A. C. Phillips, V. L. Sarajedini, R. P. Schiavon, L. Simard, A. S. Szalay, N. P. Vogt, and R. Yan. Galaxy Luminosity Functions to z˜1 from DEEP2 and COMBO-17: Implications for Red Galaxy Formation. *ApJ*, 665:265–294, Aug. 2007. doi: 10.1086/519294.

A. C. Fabian. Observational Evidence of Active Galactic Nuclei Feedback. *Ann. Rev. Astr. Astrophys.*, 50:455–489, Sept. 2012. doi: 10.1146/annurev-astro-081811-125521.

A. C. Fabian, R. J. Wilman, and C. S. Crawford. On the detectability of distant Compton-thick obscured quasars. *MNRAS*, 329:L18–L22, Jan. 2002. doi: 10.1046/j.1365-8711.2002.05138.x.

G. Fedoseev, S. Ioppolo, D. Zhao, T. Lamberts, and H. Linnartz. Low-temperature surface formation of NH_3 and HNCO: hydrogenation of nitrogen atoms in CO-rich interstellar ice analogues. *MNRAS*, 446:439–448, Jan. 2015. doi: 10.1093/mnras/stu2028.

J. F. Gallimore, S. A. Baum, C. P. O'Dea, and A. Pedlar. The Subarcsecond Radio Structure in NGC 1068. I. Observations and Results. *ApJ*, 458:136, Feb. 1996. doi: 10.1086/176798.

Y. Gao and P. M. Solomon. The Star Formation Rate and Dense Molecular Gas in Galaxies. *ApJ*, 606:271–290, May 2004. doi: 10.1086/382999.

S. García-Burillo, J. Martín-Pintado, A. Fuente, and R. Neri. Large-scale shocks in the starburst galaxy NGC 253. Interferometer mapping of a ~ 600 pc SiO/$H^{13}CO^+$ circumnuclear disk. *A&A*, 355:499–511, Mar. 2000.

S. García-Burillo, J. Martín-Pintado, A. Fuente, A. Usero, and R. Neri. Widespread HCO Emission in the Nuclear Starburst of M82. *ApJL*, 575:L55–L58, Aug. 2002. doi: 10.1086/342743.

S. García-Burillo, A. Usero, A. Fuente, J. Martín-Pintado, F. Boone, S. Aalto, M. Krips, R. Neri, E. Schinnerer, and L. J. Tacconi. Molecular gas chemistry in AGN. II. High-resolution imaging of SiO emission in NGC 1068: shocks or XDR? *A&A*, 519:A2, Sept. 2010. doi: 10.1051/0004-6361/201014539.

S. García-Burillo, F. Combes, A. Usero, S. Aalto, M. Krips, S. Viti, A. Alonso-Herrero, L. K. Hunt, E. Schinnerer, A. J. Baker, F. Boone, V. Casasola, L. Colina, F. Costagliola, A. Eckart, A. Fuente, C. Henkel, A. Labiano, S. Martín, I. Márquez, S. Muller, P. Planesas, C. Ramos Almeida, M. Spaans, L. J. Tacconi, and P. P. van der Werf. Molecular line emission in NGC 1068 imaged with ALMA. I. An AGN-driven outflow in the dense molecular gas. *A&A*, 567:A125, July 2014. doi: 10.1051/0004-6361/201423843.

S. Garcia-Burillo, F. Combes, C. Ramos Almeida, A. Usero, M. Krips, A. Alonso-Herrero, S. Aalto, V. Casasola, L. K. Hunt, S. Martin, S. Viti, L. Colina, F. Costagliola, A. Eckart, A. Fuente, C. Henkel, I. Marquez, R. Neri, E. Schinnerer, L. J. Tacconi, and P. P. van der Werf. ALMA resolves the torus of NGC 1068: continuum and molecular line emission. *ArXiv e-prints*, Apr. 2016.

R. T. Garrod, V. Wakelam, and E. Herbst. Non-thermal desorption from interstellar dust grains via exothermic surface reactions. *A&A*, 467:1103–1115, June 2007. doi: 10.1051/0004-6361:20066704.

A. Gil de Paz, S. Boissier, B. F. Madore, M. Seibert, Y. H. Joe, A. Boselli, T. K. Wyder, D. Thilker, L. Bianchi, S.-C. Rey, R. M. Rich, T. A. Barlow, T. Conrow, K. Forster, P. G. Friedman, D. C. Martin, P. Morrissey, S. G. Neff, D. Schiminovich, T. Small, J. Donas, T. M. Heckman, Y.-W. Lee, B. Milliard, A. S. Szalay, and S. Yi. The

GALEX Ultraviolet Atlas of Nearby Galaxies. *ApJSS*, 173:185–255, Dec. 2007. doi: 10.1086/516636.

P. F. Goldsmith and W. D. Langer. Population Diagram Analysis of Molecular Line Emission. *ApJ*, 517:209–225, May 1999. doi: 10.1086/307195.

R. M. González Delgado, T. Heckman, C. Leitherer, G. Meurer, J. Krolik, A. S. Wilson, A. Kinney, and A. Koratkar. Ultraviolet-Optical Observations of the Seyfert 2 Galaxies NGC 7130, NGC 5135, and IC 3639: Implications for the Starburst-Active Galactic Nucleus Connection. *ApJ*, 505:174–198, Sept. 1998. doi: 10.1086/306154.

F. O. Goodman. Formation of hydrogen molecules on interstellar grain surfaces. *ApJ*, 226:87–94, Nov. 1978. doi: 10.1086/156588.

R. J. Gould and E. E. Salpeter. The Interstellar Abundance of the Hydrogen Molecule. I. Basic Processes. *ApJ*, 138:393, Aug. 1963. doi: 10.1086/147654.

R. Gredel, S. Lepp, A. Dalgarno, and E. Herbst. Cosmic-ray-induced photodissociation and photoionization rates of interstellar molecules. *ApJ*, 347:289–293, Dec. 1989. doi: 10.1086/168117.

S. Guilloteau and R. Lucas. Imaging at the IRAM Plateau de Bure Interferometer. In J. G. Mangum and S. J. E. Radford, editors, *Imaging at Radio through Submillimeter Wavelengths*, volume 217 of *Astronomical Society of the Pacific Conference Series*, page 299, 2000.

S. Guilloteau, J. Delannoy, D. Downes, A. Greve, M. Guelin, R. Lucas, D. Morris, S. J. E. Radford, J. Wink, J. Cernicharo, T. Forveille, S. Garcia-Burillo, R. Neri, J. Blondel, A. Perrigourad, D. Plathner, and M. Torres. The IRAM interferometer on Plateau de Bure. *A&A*, 262:624–633, Sept. 1992.

A. Gusdorf, G. Pineau Des Forêts, S. Cabrit, and D. R. Flower. SiO line emission from interstellar jets and outflows: silicon-containing mantles and non-stationary shock waves. *A&A*, 490:695–706, Nov. 2008. doi: 10.1051/0004-6361:200810443.

E. Habart, F. Boulanger, L. Verstraete, C. M. Walmsley, and G. Pineau des Forêts. Some empirical estimates of the H_2 formation rate in photon-dominated regions. *A&A*, 414: 531–544, Feb. 2004. doi: 10.1051/0004-6361:20031659.

H. J. Habing. The interstellar radiation density between 912 A and 2400 A. 19:421, Jan. 1968.

D. Hollenbach and E. E. Salpeter. Molecular Hydrogen Formation on Grains in H I Regions. In *Bulletin of the American Astronomical Society*, volume 1 of *BAAS*, page 244, June 1969.

D. Hollenbach, S.-I. Chu, and R. McCray. H2 in expanding circumstellar shells. *ApJ*, 208: 458–467, Sept. 1976. doi: 10.1086/154627.

M. Imanishi, K. Nakanishi, Y. Tamura, N. Oi, and K. Kohno. Millimeter Interferometric HCN(1-0) and HCO^+(1-0) Observations of Luminous Infrared Galaxies. *AJ*, 134:2366–2384, Dec. 2007. doi: 10.1086/523598.

N. Indriolo, T. R. Geballe, T. Oka, and B. J. McCall. H^+_3 in Diffuse Interstellar Clouds: A Tracer for the Cosmic-Ray Ionization Rate. *ApJ*, 671:1736–1747, Dec. 2007. doi: 10.1086/523036.

J. A. Irwin and E. R. Seaquist. The neutral hydrogen distribution of NGC 3079. *ApJ*, 371:111–130, Apr. 1991. doi: 10.1086/169875.

F. P. Israel and F. Baas. CI and CO in the spiral galaxies NGC 6946 and M 83. *A&A*, 371:433–444, May 2001. doi: 10.1051/0004-6361:20010354.

T. Izumi, K. Kohno, S. Martín, D. Espada, N. Harada, S. Matsushita, P.-Y. Hsieh, J. L. Turner, D. S. Meier, E. Schinnerer, M. Imanishi, Y. Tamura, M. T. Curran, A. Doi, K. Fathi, M. Krips, A. A. Lundgren, N. Nakai, T. Nakajima, M. W. Regan, K. Sheth, S. Takano, A. Taniguchi, Y. Terashima, T. Tosaki, and T. Wiklind. Submillimeter ALMA Observations of the Dense Gas in the Low-Luminosity Type-1 Active Nucleus of NGC 1097. *PASJj*, 65, Oct. 2013. doi: 10.1093/pasj/65.5.100.

T. Izumi, K. Kohno, S. Aalto, A. Doi, D. Espada, K. Fathi, N. Harada, B. Hatsukade, T. Hattori, P.-Y. Hsieh, S. Ikarashi, M. Imanishi, D. Iono, S. Ishizuki, M. Krips, S. Martín, S. Matsushita, D. S. Meier, H. Nagai, N. Nakai, T. Nakajima, K. Nakanishi, H. Nomura, M. W. Regan, E. Schinnerer, K. Sheth, S. Takano, Y. Tamura, Y. Terashima, T. Tosaki, J. L. Turner, H. Umehata, and T. Wiklind. ALMA Observations of the Submillimeter Dense Molecular Gas Tracers in the Luminous Type-1 Active Nucleus of NGC 7469. *ApJ*, 811:39, Sept. 2015. doi: 10.1088/0004-637X/811/1/39.

I. Jiménez-Serra, P. Caselli, J. Martín-Pintado, and T. W. Hartquist. Parametrization of C-shocks. Evolution of the sputtering of grains. *A&A*, 482:549–559, May 2008. doi: 10.1051/0004-6361:20078054.

J. Kamenetzky, J. Glenn, P. R. Maloney, J. E. Aguirre, J. J. Bock, C. M. Bradford, L. Earle, H. Inami, H. Matsuhara, E. J. Murphy, B. J. Naylor, H. T. Nguyen, and J. Zmuidzinas. The Dense Molecular Gas in the Circumnuclear Disk of NGC 1068. *ApJ*, 731:83, Apr. 2011. doi: 10.1088/0004-637X/731/2/83.

G. Kelly, S. Viti, E. Bayet, R. Aladro, and J. Yates. Mapping CS in starburst galaxies: Disentangling and characterising dense gas. *A&A*, 578:A70, June 2015. doi: 10.1051/0004-6361/201425502.

R. C. Kennicutt and N. J. Evans. Star Formation in the Milky Way and Nearby Galaxies. *Ann. Rev. Astr. Astrophys.*, 50:531–608, Sept. 2012. doi: 10.1146/annurev-astro-081811-125610.

R. C. Kennicutt, Jr. Star Formation in Galaxies Along the Hubble Sequence. *Ann. Rev. Astr. Astrophys.*, 36:189–232, 1998. doi: 10.1146/annurev.astro.36.1.189.

R. C. Kennicutt, Jr., F. Schweizer, J. E. Barnes, D. Friedli, L. Martinet, and D. Pfenniger, editors. *Galaxies: Interactions and Induced Star Formation*, 1998.

A. A. Kepley, A. K. Leroy, D. Frayer, A. Usero, J. Marvil, and F. Walter. The Green Bank Telescope Maps the Dense, Star-forming Gas in the Nearby Starburst Galaxy M82. *ApJL*, 780:L13, Jan. 2014. doi: 10.1088/2041-8205/780/1/L13.

E. Y. Khachikian and D. W. Weedman. A Blue Galactic Nucleus with a Featureless Spectrum. *ApJL*, 189:L99, May 1974. doi: 10.1086/181473.

M. Kishimoto. The Location of the Nucleus of NGC 1068 and the Three-dimensional Structure of Its Nuclear Region. *ApJ*, 518:676–692, June 1999. doi: 10.1086/307290.

S. Klose. Hydrogen chemisorption on a graphite surface. *A&A*, 260:321–328, July 1992.

J. Koda, Y. Sofue, K. Kohno, H. Nakanishi, S. Onodera, S. K. Okumura, and J. A. Irwin. Nobeyama Millimeter Array CO (J=1-0) Observations of the Hα/Radio Lobe Galaxy NGC 3079: Gas Dynamics in a Weak Bar Potential and Central Massive Core. *ApJ*, 573:105–121, July 2002. doi: 10.1086/340561.

K. Kohno, S. Matsushita, B. Vila-Vilaró, S. K. Okumura, T. Shibatsuka, M. Okiura, S. Ishizuki, and R. Kawabe. Dense Molecular Gas and Star Formation in Nearby Seyfert Galaxies. In J. H. Knapen, J. E. Beckman, I. Shlosman, and T. J. Mahoney, editors, *The Central Kiloparsec of Starbursts and AGN: The La Palma Connection*, volume 249 of *Astronomical Society of the Pacific Conference Series*, page 672, 2001.

J. Kormendy, N. Drory, M. E. Cornell, and R. Bender. No Supermassive Black Holes in Giant Galaxy Disks: M101 and NGC 6946. In *American Astronomical Society Meeting Abstracts*, volume 39 of *Bulletin of the American Astronomical Society*, page 860, Dec. 2007.

M. Krips, R. Neri, S. García-Burillo, S. Martín, F. Combes, J. Graciá-Carpio, and A. Eckart. A Multi-transition HCN and HCO^+ Study of 12 Nearby Active Galaxies: Active Galactic Nucleus versus Starburst Environments. *ApJ*, 677:262–275, Apr. 2008. doi: 10.1086/527367.

M. Krips, S. Martín, A. Eckart, R. Neri, S. García-Burillo, S. Matsushita, A. Peck, I. Stoklasová, G. Petitpas, A. Usero, F. Combes, E. Schinnerer, E. Humphreys, and A. J. Baker. Submillimeter Array/Plateau de Bure Interferometer Multiple Line Observations of the Nearby Seyfert 2 Galaxy NGC 1068: Shock-related Gas Kinematics and Heating in the Central 100 pc? *ApJ*, 736:37, July 2011. doi: 10.1088/0004-637X/736/1/37.

E. Krügel, editor. *The Physics of Interstellar Dust*, volume 10 of *Wiley Praxis Series in Astronomy and Astrophysics*, Dec. 2002. doi: 10.1201/9781420033335.

C. Leitherer, D. Schaerer, J. D. Goldader, R. M. G. Delgado, C. Robert, D. F. Kune, D. F. de Mello, D. Devost, and T. M. Heckman. Starburst99: Synthesis Models for Galaxies with Active Star Formation. *ApJSS*, 123:3–40, July 1999. doi: 10.1086/313233.

S. Lepp and A. Dalgarno. X-ray-induced chemistry of interstellar clouds. *A&A*, 306: L21–L24, Feb. 1996.

J. Lequeux. *The Interstellar Medium*. 2005. doi: 10.1007/b137959.

A. K. Leroy, F. Walter, E. Brinks, F. Bigiel, W. J. G. de Blok, B. Madore, and M. D. Thornley. The Star Formation Efficiency in Nearby Galaxies: Measuring Where Gas Forms Stars Effectively. *ApJ*, 136:2782–2845, Dec. 2008. doi: 10.1088/0004-6256/136/6/2782.

A. K. Leroy, F. Walter, A. Schruba, F. Bigiel, K. Foyle, and HERACLES Team. HERACLES: The HERA CO-Line Extragalactic Survey. In *American Astronomical Society Meeting Abstracts 217*, volume 43 of *Bulletin of the American Astronomical Society*, page 246.14, Jan. 2011.

E. S. Levine, T. T. Helfer, R. Meijerink, and L. Blitz. The Dense Gas in the Central Kiloparsec of NGC 6946. *ApJ*, 673:183–192, Jan. 2008. doi: 10.1086/524027.

C. J. Lintott, S. Viti, D. A. Williams, J. M. C. Rawlings, and I. Ferreras. Hot cores: probes of high-redshift galaxies? *MNRAS*, 360:1527–1531, July 2005. doi: 10.1111/j.1365-2966.2005.09151.x.

A. López-Sepulcre, A. A. Jaber, E. Mendoza, B. Lefloch, C. Ceccarelli, C. Vastel, R. Bachiller, J. Cernicharo, C. Codella, C. Kahane, M. Kama, and M. Tafalla. Shedding light on the formation of the pre-biotic molecule formamide with ASAI. *MNRAS*, 449:2438–2458, May 2015. doi: 10.1093/mnras/stv377.

N. Lu, Y. Zhao, C. K. Xu, Y. Gao, T. Díaz-Santos, V. Charmandaris, H. Inami, J. Howell, L. Liu, L. Armus, J. M. Mazzarella, G. C. Privon, S. D. Lord, D. B. Sanders, B. Schulz, and P. P. van der Werf. Measuring Star Formation Rate and Far-infrared Color in High-redshift Galaxies Using the CO(7-6) and [N II] 205 μm Lines. *ApJL*, 802:L11, Mar. 2015. doi: 10.1088/2041-8205/802/1/L11.

R. Lucas and H. S. Liszt. Comparative chemistry of diffuse clouds. III. Sulfur-bearing molecules. *A&A*, 384:1054–1061, Mar. 2002. doi: 10.1051/0004-6361:20020043.

J. G. Mangum, J. Darling, C. Henkel, K. M. Menten, M. MacGregor, B. E. Svoboda, and E. Schinnerer. Ammonia Thermometry of Star-Forming Galaxies. *ApJ*, 779:33, Dec. 2013. doi: 10.1088/0004-637X/779/1/33.

S. Martín, J. Martín-Pintado, R. Mauersberger, C. Henkel, and S. García-Burillo. Sulfur Chemistry and Isotopic Ratios in the Starburst Galaxy NGC 253. *ApJ*, 620:210–216, Feb. 2005. doi: 10.1086/426888.

S. Martín, R. Mauersberger, J. Martín-Pintado, C. Henkel, and S. García-Burillo. A 2 Millimeter Spectral Line Survey of the Starburst Galaxy NGC 253. *ApJ*, 164:450–476, June 2006. doi: 10.1086/503297.

S. Martín, J. Martín-Pintado, and R. Mauersberger. HNCO Abundances in Galaxies: Tracing the Evolutionary State of Starbursts. *ApJ*, 694:610–617, Mar. 2009a. doi: 10.1088/0004-637X/694/1/610.

S. Martín, J. Martín-Pintado, and S. Viti. Photodissociation Chemistry Footprints in the Starburst Galaxy NGC 253. *ApJ*, 706:1323–1330, Dec. 2009b. doi: 10.1088/0004-637X/706/2/1323.

J. Martín-Pintado, P. de Vicente, A. Fuente, and P. Planesas. SiO Emission from the Galactic Center Molecular Clouds. *ApJL*, 482:L45–L48, June 1997. doi: 10.1086/310691.

L. P. Martins, R. Riffel, A. Rodríguez-Ardila, R. Gruenwald, and R. de Souza. Nuclear and extended spectra of NGC 1068 - II. Near-infrared stellar population synthesis. *MNRAS*, 406:2185–2192, Aug. 2010. doi: 10.1111/j.1365-2966.2010.16817.x.

J. S. Mathis, W. Rumpl, and K. H. Nordsieck. The size distribution of interstellar grains. *ApJ*, 217:425–433, Oct. 1977. doi: 10.1086/155591.

T. A. Matthews and A. R. Sandage. Optical Identification of 3c 48, 3c 196, and 3c 286 with Stellar Objects. *ApJ*, 138:30, July 1963. doi: 10.1086/147615.

R. Mauersberger and C. Henkel. Dense gas in nearby galaxies. I - Distribution, kinematics and multilevel studies of CS. *A&A*, 223:79–88, Oct. 1989.

R. Mauersberger, C. Henkel, T. L. Wilson, and J. Harju. Dense gas in nearby galaxies. II - CS emission from spiral galaxies. *A&A*, 226:L5–L8, Dec. 1989.

D. McElroy, C. Walsh, A. J. Markwick, M. A. Cordiner, K. Smith, and T. J. Millar. The UMIST database for astrochemistry 2012. *A&A*, 550:A36, Feb. 2013. doi: 10.1051/0004-6361/201220465.

C. F. McKee and J. P. Ostriker. A theory of the interstellar medium - Three components regulated by supernova explosions in an inhomogeneous substrate. *ApJ*, 218:148–169, Nov. 1977. doi: 10.1086/155667.

D. S. Meier and J. L. Turner. Spatially Resolved Chemistry in Nearby Galaxies. I. The Center of IC 342. *ApJ*, 618:259–280, Jan. 2005. doi: 10.1086/426499.

D. S. Meier and J. L. Turner. Spatially Resolved Chemistry in nearby Galaxies. II. The Nuclear Bar in Maffei 2. *ApJ*, 755:104, Aug. 2012. doi: 10.1088/0004-637X/755/2/104.

D. S. Meier, F. Walter, A. D. Bolatto, A. K. Leroy, J. Ott, E. Rosolowsky, S. Veilleux, S. R. Warren, A. Weiß, M. A. Zwaan, and L. K. Zschaechner. ALMA Multi-line Imaging of the Nearby Starburst NGC 253. *ApJ*, 801:63, Mar. 2015. doi: 10.1088/0004-637X/801/1/63.

R. Meijerink and M. Spaans. Diagnostics of irradiated gas in galaxy nuclei. I. A far-ultraviolet and X-ray dominated region code. *A&A*, 436:397–409, June 2005. doi: 10.1051/0004-6361:20042398.

R. Meijerink, M. Spaans, and F. P. Israel. Diagnostics of irradiated dense gas in galaxy nuclei. II. A grid of XDR and PDR models. *A&A*, 461:793–811, Jan. 2007. doi: 10.1051/0004-6361:20066130.

R. Meijerink, M. Spaans, I. Kamp, G. Aresu, W.-F. Thi, and P. Woitke. Tracing the Physical Conditions in Active Galactic Nuclei with Time-Dependent Chemistry. *Journal of Physical Chemistry A*, 117:9593–9604, Oct. 2013. doi: 10.1021/jp312289f.

S. Mineo, M. Gilfanov, B. D. Lehmer, G. E. Morrison, and R. Sunyaev. X-ray emission from star-forming galaxies - III. Calibration of the L_X-SFR relation up to redshift z 1.3. *MNRAS*, 437:1698–1707, Jan. 2014. doi: 10.1093/mnras/stt1999.

D. J. Mortlock, S. J. Warren, B. P. Venemans, M. Patel, P. C. Hewett, R. G. McMahon, C. Simpson, T. Theuns, E. A. Gonzáles-Solares, A. Adamson, S. Dye, N. C. Hambly, P. Hirst, M. J. Irwin, E. Kuiper, A. Lawrence, and H. J. A. Röttgering. A luminous quasar at a redshift of z = 7.085. *Nature*, 474:616–619, June 2011. doi: 10.1038/nature10159.

F. Müller-Sánchez, M. A. Prieto, E. K. S. Hicks, H. Vives-Arias, R. I. Davies, M. Malkan, L. J. Tacconi, and R. Genzel. Outflows from Active Galactic Nuclei: Kinematics of the Narrow-line and Coronal-line Regions in Seyfert Galaxies. *ApJ*, 739:69, Oct. 2011. doi: 10.1088/0004-637X/739/2/69.

T. Nakajima, S. Takano, K. Kohno, N. Harada, E. Herbst, Y. Tamura, T. Izumi, A. Taniguchi, and T. Tosaki. High-Resolution Imaging in 3-mm and 0.8-mm Bands and Abundances of Shock/Dust Related Molecules Toward the Seyfert Galaxy NGC 1068 Observed with ALMA. In D. Iono, K. Tatematsu, A. Wootten, and L. Testi, editors, *Revolution in Astronomy with ALMA: The Third Year*, volume 499 of *Astronomical Society of the Pacific Conference Series*, page 109, Dec. 2015.

L. A. M. Nejad, D. A. Williams, and S. B. Charnley. Dynamical Models of Molecular Clouds - Nitrogen Chemistry. *MNRAS*, 246:183, Sept. 1990.

M. Nenkova, M. M. Sirocky, Ž. Ivezić, and M. Elitzur. AGN Dusty Tori. I. Handling of Clumpy Media. *ApJ*, 685:147-159, Sept. 2008a. doi: 10.1086/590482.

M. Nenkova, M. M. Sirocky, R. Nikutta, Ž. Ivezić, and M. Elitzur. AGN Dusty Tori. II. Observational Implications of Clumpiness. *ApJ*, 685:160-180, Sept. 2008b. doi: 10.1086/590483.

R. Neri, R. Genzel, R. J. Ivison, F. Bertoldi, A. W. Blain, S. C. Chapman, P. Cox, T. R. Greve, A. Omont, and D. T. Frayer. Interferometric Observations of Powerful CO Emission from Three Submillimeter Galaxies at z=2.39, 2.51, and 3.35. *ApJL*, 597: L113–L116, Nov. 2003. doi: 10.1086/379968.

B. P. Nicholas, G. Rowell, M. G. Burton, A. J. Walsh, Y. Fukui, A. Kawamura, and N. I. Maxted. A 7 mm line survey of the shocked and disrupted molecular gas towards the W28 field TeV gamma-ray sources. *MNRAS*, 419:251–266, Jan. 2012. doi: 10.1111/j.1365-2966.2011.19688.x.

A. Nilsson, Å. Hjalmarson, P. Bergman, and T. J. Millar. SO and CS observations of molecular clouds. II. Analysis and modelling of the abundance ratios - probing O_2/CO with SO/CS? *A&A*, 358:257–275, June 2000.

J. A. Noble, P. Theule, F. Mispelaer, F. Duvernay, G. Danger, E. Congiu, F. Dulieu, and T. Chiavassa. The desorption of H_2CO from interstellar grains analogues. *A&A*, 543: A5, July 2012. doi: 10.1051/0004-6361/201219437.

T. Onishi, A. Mizuno, A. Kawamura, H. Ogawa, and Y. Fukui. A $C^{18}O$ Survey of Dense Cloud Cores in Taurus: Star Formation. *ApJ*, 502:296–314, July 1998. doi: 10.1086/305867.

D. E. Osterbrock. *Astrophysics of gaseous nebulae*. 1974.

H.-A. Pan, N. Kuno, J. Koda, A. Hirota, K. Sorai, and H. Kaneko. Molecular Gas and Star-formation Properties in the Central and Bar Regions of NGC 6946. *ApJ*, 815:59, Dec. 2015. doi: 10.1088/0004-637X/815/1/59.

J. P. Pérez-Beaupuits, M. Spaans, F. F. S. van der Tak, S. Aalto, S. García-Burillo, A. Fuente, and A. Usero. Probing X-ray irradiation in the nucleus of NGC 1068 with observations of high-J lines of dense gas tracers. *A&A*, 503:459–466, Aug. 2009. doi: 10.1051/0004-6361/200912350.

V. Pirronello, J. Krelowski, and G. Manicò, editors. *Solid state astrochemistry*, volume 120, 2003.

S. A. Pustilnik, A. Y. Kniazev, V. A. Lipovetsky, and A. V. Ugryumov. Environment status of blue compact galaxies and trigger of star formation. *A&A*, 373:24–37, July 2001. doi: 10.1051/0004-6361:20010555.

J. M. C. Rawlings and J. A. Yates. Modelling line profiles in infalling cores. *MNRAS*, 326:1423–1430, Oct. 2001. doi: 10.1111/j.1365-8711.2001.04674.x.

J. M. C. Rawlings, T. W. Hartquist, K. M. Menten, and D. A. Williams. Direct diagnosis of infall in collapsing protostars. I - The theoretical identification of molecular species with broad velocity distributions. *MNRAS*, 255:471–485, Apr. 1992.

L. J. Rickard, P. Palmer, M. Morris, B. Zuckerman, and B. E. Turner. Detection of extragalactic carbon monoxide at millimeter wavelengths. *ApJL*, 199:L75–L78, July 1975. doi: 10.1086/181852.

J. F. Roberts, J. M. C. Rawlings, S. Viti, and D. A. Williams. Desorption from interstellar ices. *MNRAS*, 382:733–742, Dec. 2007. doi: 10.1111/j.1365-2966.2007.12402.x.

T. P. Robitaille and B. A. Whitney. The Present-Day Star Formation Rate of the Milky Way Determined from Spitzer-Detected Young Stellar Objects. *ApJL*, 710:L11–L15, Feb. 2010. doi: 10.1088/2041-8205/710/1/L11.

N. J. Rodríguez-Fernández, M. Tafalla, F. Gueth, and R. Bachiller. HNCO enhancement by shocks in the L1157 molecular outflow. *A&A*, 516:A98, June 2010. doi: 10.1051/0004-6361/201013997.

D. S. N. Rupke and S. Veilleux. Integral Field Spectroscopy of Massive, Kiloparsec-scale Outflows in the Infrared-luminous QSO Mrk 231. *ApJL*, 729:L27, Mar. 2011. doi: 10.1088/2041-8205/729/2/L27.

S. Salim, R. M. Rich, S. Charlot, J. Brinchmann, B. D. Johnson, D. Schiminovich, M. Seibert, R. Mallery, T. M. Heckman, K. Forster, P. G. Friedman, D. C. Martin, P. Morrissey, S. G. Neff, T. Small, T. K. Wyder, L. Bianchi, J. Donas, Y.-W. Lee, B. F. Madore, B. Milliard, A. S. Szalay, B. Y. Welsh, and S. K. Yi. UV Star Formation Rates in the Local Universe. *ApJSS*, 173:267–292, Dec. 2007. doi: 10.1086/519218.

W. C. Saslaw and D. Zipoy. Molecular Hydrogen in Pre-galactic Gas Clouds. *Nature*, 216: 976–978, Dec. 1967. doi: 10.1038/216976a0.

B. D. Savage and J. S. Mathis. Observed properties of interstellar dust. *Ann. Rev. Astr. Astrophys.*, 17:73–111, 1979. doi: 10.1146/annurev.aa.17.090179.000445.

C. Savage and L. M. Ziurys. Ion Chemistry in Photon-dominated Regions: Examining the $[HCO^+]/[HOC^+]/[CO^+]$ Chemical Network. *ApJ*, 616:966–975, Dec. 2004. doi: 10.1086/424964.

G. B. Scharmer and M. Carlsson. A new approach to multi-level non-LTE radiative transfer problems. *Journal of Computational Physics*, 59:56–80, May 1985. doi: 10.1016/0021-9991(85)90107-X.

K. Schawinski, C. M. Urry, B. D. Simmons, L. Fortson, S. Kaviraj, W. C. Keel, C. J. Lintott, K. L. Masters, R. C. Nichol, M. Sarzi, R. Skibba, E. Treister, K. W. Willett, O. I. Wong, and S. K. Yi. The green valley is a red herring: Galaxy Zoo reveals two evolutionary pathways towards quenching of star formation in early- and late-type galaxies. *MNRAS*, 440:889–907, May 2014. doi: 10.1093/mnras/stu327.

P. Schilke, C. M. Walmsley, G. Pineau des Forets, and D. R. Flower. SiO production in interstellar shocks. *A&A*, 321:293–304, May 1997.

E. Schinnerer, A. Eckart, L. J. Tacconi, R. Genzel, and D. Downes. Bars and Warps Traced by the Molecular Gas in the Seyfert 2 Galaxy NGC 1068. *ApJ*, 533:850–868, Apr. 2000. doi: 10.1086/308702.

E. Schinnerer, T. Böker, E. Emsellem, and U. Lisenfeld. Molecular Gas Dynamics in NGC 6946: A Bar-driven Nuclear Starburst "Caught in the Act". *ApJ*, 649:181–200, Sept. 2006. doi: 10.1086/506265.

E. Schinnerer, T. Böker, E. Emsellem, and D. Downes. Bar-driven mass build-up within the central 50 pc of NGC 6946. *A&A*, 462:L27–L30, Feb. 2007. doi: 10.1051/0004-6361:20066711.

M. Schmidt. Lifetimes of Extragalactic Radio Sources. *ApJ*, 146:7, Oct. 1966. doi: 10.1086/148854.

F. L. Schöier, F. F. S. van der Tak, E. F. van Dishoeck, and J. H. Black. An atomic and molecular database for analysis of submillimetre line observations. *A&A*, 432:369–379, Mar. 2005. doi: 10.1051/0004-6361:20041729.

Y. Shimajiri, Y. Kitamura, F. Nakamura, M. Momose, M. Saito, T. Tsukagoshi, M. Hiramatsu, T. Shimoikura, K. Dobashi, C. Hara, and R. Kawabe. Catalog of Dense Cores in the Orion A Giant Molecular Cloud. *ApJSS*, 217:7, Mar. 2015. doi: 10.1088/0067-0049/217/1/7.

J. Silk and M. J. Rees. Quasars and galaxy formation. *A&A*, 331:L1–L4, Mar. 1998.

M. F. Skrutskie, R. M. Cutri, R. Stiening, M. D. Weinberg, S. Schneider, J. M. Carpenter, C. Beichman, R. Capps, T. Chester, J. Elias, J. Huchra, J. Liebert, C. Lonsdale, D. G. Monet, S. Price, P. Seitzer, T. Jarrett, J. D. Kirkpatrick, J. E. Gizis, E. Howard, T. Evans, J. Fowler, L. Fullmer, R. Hurt, R. Light, E. L. Kopan, K. A. Marsh, H. L. McCallon, R. Tam, S. Van Dyk, and S. Wheelock. The Two Micron All Sky Survey (2MASS). *ApJ*, 131:1163–1183, Feb. 2006. doi: 10.1086/498708.

K. Sliwa, C. D. Wilson, D. Iono, A. Peck, and S. Matsushita. Around the Ring We Go: The Cold, Dense Ring of Molecular Gas in NGC 1614. *ApJL*, 796:L15, Nov. 2014. doi: 10.1088/2041-8205/796/1/L15.

D. A. Smith and A. S. Wilson. A Chandra X-Ray Study of NGC 1068. II. The Luminous X-Ray Source Population. *ApJ*, 591:138–153, July 2003. doi: 10.1086/375291.

I. L. Smith and M. Wardle. An analysis of HCN observations of the Circumnuclear Disc at the Galactic Centre. *MNRAS*, 437:3159–3171, Feb. 2014. doi: 10.1093/mnras/stt2092.

T. P. Snow and A. N. Witt. Interstellar Depletions Updated: Where All the Atoms Went. *ApJL*, 468:L65, Sept. 1996. doi: 10.1086/310225.

V. V. Sobolev. *Moving envelopes of stars*. 1960.

P. M. Solomon, D. Downes, and S. J. E. Radford. Dense molecular gas and starbursts in ultraluminous galaxies. *ApJL*, 387:L55–L59, Mar. 1992. doi: 10.1086/186304.

L. Spitzer, Jr. Review of Publications: Physical Processes in the Interstellar Medium. *JRASC*, 72:349, Dec. 1978.

H. W. W. Spoon, J. V. Keane, A. G. G. M. Tielens, D. Lutz, and A. F. M. Moorwood. The obscured mid-infrared continuum of NGC 4418: A dust- and ice-enshrouded AGN. *A&A*, 365:L353–L356, Jan. 2001. doi: 10.1051/0004-6361:20000557.

A. Sternberg and A. Dalgarno. Chemistry in Dense Photon-dominated Regions. *ApJSS*, 99:565, Aug. 1995. doi: 10.1086/192198.

A. Sternberg, A. Dalgarno, and S. Lepp. Cosmic-ray-induced photodestruction of interstellar molecules in dense clouds. *ApJ*, 320:676–682, Sept. 1987. doi: 10.1086/165585.

D. K. Strickland, T. M. Heckman, K. A. Weaver, C. G. Hoopes, and M. Dahlem. Chandra Observations of NGC 253. II. On the Origin of Diffuse X-Ray Emission in the Halos of Starburst Galaxies. *ApJ*, 568:689–716, Apr. 2002. doi: 10.1086/338889.

S. Takano, T. Nakajima, K. Kohno, N. Harada, E. Herbst, Y. Tamura, T. Izumi, A. Taniguchi, and T. Tosaki. Distributions of molecules in the circumnuclear disk and surrounding starburst ring in the Seyfert galaxy NGC 1068 observed with ALMA. *PASJ*, 66:75, July 2014. doi: 10.1093/pasj/psu052.

J. C. Tan, S. Kong, M. J. Butler, P. Caselli, and F. Fontani. The Dynamics of Massive Starless Cores with ALMA. *ApJ*, 779:96, Dec. 2013. doi: 10.1088/0004-637X/779/2/96.

C.-W. Tsai, J. L. Turner, S. C. Beck, D. S. Meier, and S. A. Wright. The Circumnuclear Star Formation Environment of NGC 6946: Br γ and H_2 Results from Keck Integral Field Spectroscopy. *ApJ*, 776:70, Oct. 2013. doi: 10.1088/0004-637X/776/2/70.

R. Tunnard and T. R. Greve. How Dense is Your Gas? On the Recoverability of LVG Model Parameters. *ApJ*, 819:161, Mar. 2016. doi: 10.3847/0004-637X/819/2/161.

J. L. Turner and P. T. P. Ho. VLA observations of massive star formation in spiral nuclei. *ApjL*, 268:L79–L83, May 1983. doi: 10.1086/184033.

T. Umebayashi and T. Nakano. Recombination of Ions and Electrons on Grains and the Ionization Degree in Dense Interstellar Clouds. , 32:405, 1980.

A. Usero, S. García-Burillo, J. Martín-Pintado, A. Fuente, and R. Neri. Large-scale molecular shocks in galaxies: the SiO interferometer map of ¡ASTROBJ¿IC 342¡/ASTROBJ¿. *A&A*, 448:457–470, Mar. 2006. doi: 10.1051/0004-6361:20054033.

F. F. S. van der Tak, J. H. Black, F. L. Schöier, D. J. Jansen, and E. F. van Dishoeck. A computer program for fast non-LTE analysis of interstellar line spectra. With diagnostic plots to interpret observed line intensity ratios. *A&A*, 468:627–635, June 2007. doi: 10.1051/0004-6361:20066820.

E. F. van Dishoeck. Astrochemistry of dust, ice and gas: introduction and overview. *Faraday Discussions*, 168:9, 2014. doi: 10.1039/C4FD00140K.

S. Veilleux, G. Cecil, J. Bland-Hawthorn, R. B. Tully, A. V. Filippenko, and W. L. W. Sargent. The nuclear superbubble of NGC 3079. *ApJ*, 433:48–64, Sept. 1994. doi: 10.1086/174624.

G. Vidali. H2 Formation on Interstellar Grains. *Chemical Reviews*, 113:8752–8782, Dec. 2013. doi: 10.1021/cr400156b.

S. Viti. Astrochemistry in external galaxies: how to use molecules as probes of their physical conditions. *ArXiv e-prints*, Mar. 2016.

S. Viti and D. A. Williams. Time-dependent evaporation of icy mantles in hot cores. *MNRAS*, 305:755–762, May 1999. doi: 10.1046/j.1365-8711.1999.02447.x.

S. Viti, P. Caselli, T. W. Hartquist, and D. A. Williams. Chemical signatures of shocks in hot cores. *A&A*, 370:1017–1025, May 2001. doi: 10.1051/0004-6361:20010300.

S. Viti, C. Codella, M. Benedettini, and R. Bachiller. The origin and structure of clumps along molecular outflows: the test case of CB3. *MNRAS*, 350:1029–1037, May 2004a. doi: 10.1111/j.1365-2966.2004.07722.x.

S. Viti, M. P. Collings, J. W. Dever, M. R. S. McCoustra, and D. A. Williams. Evaporation of ices near massive stars: models based on laboratory temperature programmed desorption data. *MNRAS*, 354:1141–1145, Nov. 2004b. doi: 10.1111/j.1365-2966.2004.08273.x.

S. Viti, I. Jimenez-Serra, J. A. Yates, C. Codella, M. Vasta, P. Caselli, B. Lefloch, and C. Ceccarelli. L1157-B1: Water and Ammonia as Diagnostics of Shock Temperature. *ApJL*, 740:L3, Oct. 2011. doi: 10.1088/2041-8205/740/1/L3.

S. Viti, S. García-Burillo, A. Fuente, L. K. Hunt, A. Usero, C. Henkel, A. Eckart, S. Martin, M. Spaans, S. Muller, F. Combes, M. Krips, E. Schinnerer, V. Casasola, F. Costagliola, I. Marquez, P. Planesas, P. P. van der Werf, S. Aalto, A. J. Baker, F. Boone, and L. J. Tacconi. Molecular line emission in NGC1068 imaged with ALMA: II. The chemistry of the dense molecular gas. *ArXiv e-prints*, July 2014.

W. Walsh, R. Beck, G. Thuma, A. Weiss, R. Wielebinski, and M. Dumke. Molecular gas in NGC 6946. *A&A*, 388:7–28, June 2002. doi: 10.1051/0004-6361:20020467.

F. Walter, C. Carilli, F. Bertoldi, K. Menten, P. Cox, K. Y. Lo, X. Fan, and M. A. Strauss. Resolved Molecular Gas in a Quasar Host Galaxy at Redshift z=6.42. *ApJL*, 615:L17–L20, Nov. 2004. doi: 10.1086/426017.

J. C. Weingartner and B. T. Draine. Dust Grain-Size Distributions and Extinction in the Milky Way, Large Magellanic Cloud, and Small Magellanic Cloud. *ApJ*, 548:296–309, Feb. 2001. doi: 10.1086/318651.

L. Weliachew. Detection of Interstellar OH in Two External Galaxies. *ApJL*, 167:L47, July 1971. doi: 10.1086/180757.

D. R. Wik, B. D. Lehmer, A. E. Hornschemeier, M. Yukita, A. Ptak, A. Zezas, V. Antoniou, M. K. Argo, K. Bechtol, S. Boggs, F. Christensen, W. Craig, C. Hailey, F. Harrison, R. Krivonos, T. J. Maccarone, D. Stern, T. Venters, and W. W. Zhang. Spatially Resolving a Starburst Galaxy at Hard X-Ray Energies: NuSTAR, Chandra, and VLBA Observations of NGC 253. *ApJ*, 797:79, Dec. 2014. doi: 10.1088/0004-637X/797/2/79.

J. Woodall, M. Agúndez, A. J. Markwick-Kemper, and T. J. Millar. The UMIST database for astrochemistry 2006. *A&A*, 466:1197–1204, May 2007. doi: 10.1051/0004-6361:20064981.

D. E. Woon. Modeling Gas-Grain Chemistry with Quantum Chemical Cluster Calculations. I. Heterogeneous Hydrogenation of CO and H_2CO on Icy Grain Mantles. *ApJ*, 569:541–548, Apr. 2002. doi: 10.1086/339279.

A. Wootten and A. R. Thompson. The Atacama Large Millimeter/Submillimeter Array. *IEEE Proceedings*, 97:1463–1471, Aug. 2009. doi: 10.1109/JPROC.2009.2020572.

M. Yamagishi, H. Kaneda, D. Ishihara, S. Komugi, T. Suzuki, and T. Onaka. AKARI Infrared Observations of the Edge-On Spiral Galaxy NGC 3079. *PASJ*, 62:1085–, Aug. 2010. doi: 10.1093/pasj/62.4.1085.

Z.-Y. Zhang, Y. Gao, C. Henkel, Y. Zhao, J. Wang, K. M. Menten, and R. Güsten. Dense Gas Tracers and Star Formation Laws in Active Galaxies: APEX Survey of HCN J = 4 - 3, HCO^+ J = 4 - 3, and CS J = 7 - 6. *ApJL*, 784:L31, Apr. 2014. doi: 10.1088/2041-8205/784/2/L31.

H. Zinnecker and H. W. Yorke. Toward Understanding Massive Star Formation. *A&AR*, 45:481–563, Sept. 2007. doi: 10.1146/annurev.astro.44.051905.092549.